TRABAJO FINAL DE MÁSTER

Máster en
Ingeniería del Terreno
e Ingeniería Sísmica

TÍTULO

CAT SCANNER AS A TOOL FOR GEOTECHNICAL SAMPLE INSPECTION

AUTOR

NÚRIA SAU VALENZUELA

TUTOR

MARCOS ARROYO ALVAREZ DE TOLEDO

ESPECIALIDAD

INGENIERÍA DEL TERRENO

FECHA

28 de Julio del 2013

Dep. de Ingeniería del Terreno, Cartográfica y Geofísica
E.T.S. Ingenieros de Caminos, Canales y Puertos
UPC

UNIVERSIDAD POLITÉCNICA DE CATALUÑA

ACKNOWLEDGEMENTS

A mi director Marcos Arroyo, por confiar en mí y ayudarme cuando lo he necesitado.

A todos los habituales del laboratorio, por su ayuda, sus conocimientos y evidentemente, su compañía.

Y a toda la gente que ha estado a mi lado durante este proceso.

Muchas gracias a todos.

ABSTRACT

X-ray computed tomography (CT) provides nondestructive three-dimensional visualization and characterization, creating images that map the variation of X-ray attenuation within objects, which relates closely to bulk density.

In this work it was considered interesting to use this technique as a tool for geotechnical inspection sample. CT scans of soil samples of Castelló d'Empúries (close to Figueres, Spain) were quantitatively evaluated to determine wet bulk density.

The CT scans performed over Castello soil samples were obtained as part of a larger experimental program related to the Soft Soil Project (Arroyo et al., 2012). This project had as a main objective the evaluation of sample disturbance produced by various sampling methods.

A state-of-art of X-ray computed tomography applied to geosciences was perfomed. It was found that X-ray attenuation depends on the bulk density of the sample, its porosity, water content and chemical composition in a complex way. Therefore, experimental calibration was necessary to unambiguosly determine the wet bulk density of the Castello soil from the CAT values. A complementary experimental campaign using several reconstituted soils was performed for that purpose.

Once the calibration was established it was applied to the CT scans of the Castello soil samples to obtain detailed profiles of wet bulk density for the tube samples and specific values for the lab test specimens. For the late wet bulk density values had been previously obtained from lab procedures. It was the possible to check the quality of the results obtained from CT scan analysis. Very good agreement was attained between both measurements. This means that the calibration and the post-process of the CT scan data were successful.

Specimen quality classification results of the Soft Soil Project were reviewed, since the initial results were unreliable. The reviewing process included the sample disturbance criterion applied (Lunne et al. 1997) and all the laboratory tests results. The newly obtained CAT density was useful to identify some mistakes in the original test interpretation. After correcting then, the results were re-analyzed. A new quality classification for the specimens was obtained and it was checked for consistency against the results of the laboratory tests. This study confirms the applicability of the Lunne criteria of sample quality well away from the geotechnical setting for which they were originally proposed.

The CT scan images and the sample quality assessment results indicate that, for the Castello soil, there is no advantage in using Osterberg piston-type samplers instead of simpler pushed Shelby tubes.

INDEX

LIST OF TABLES

LIST OF FIGURES

Chapter I. INTRODUCTION

1.1 BACKGROUND

A research project on geotechnical sample quality was developed at UPC during 2010-2012 with support from the Spanish ministry of science and Igeotest, a geotechnical investigation contractor. The project (Arroyo et al., 2012) had as a main objective the evaluation of sample disturbance produced by various sampling methods. The sampling campaign took place on Castelló d'Empúries (close to Figueres, Spain). Samples were obtained using: unconventional Sherbrooke sampler, Shelby sampler (with interior diameters of 83 and 76mm) and hydraulic piston sampler also call Österberg sampler (with interior diameters of 95 and 76mm). For the assessment of the sample behaviour many tests were conducted. These include CAUC triaxial and CRS oedometer tests, measurements of initial suction and measurements of shear wave velocity with bender elements. The author of this thesis participated actively in that testing campaign.

Classification of sample quality during the project was based on established criteria, but the results were anomalous, indicating an almost uniform quality for all samples despite the very different sampling means employed. One of the parameters entering the sample quality assessment was initial void ratio. There were reasonable doubts about the values that had been established for this parameter in the laboratory.

X-ray computed tomography scans had been performed on the project samples, but these tests were only employed qualitatively. The CT scans have been used to observe the sedimentary structure and also to detect major heterogeneities (fissures, inclusions, etc), to select the more suitable zones for laboratory test specimens.

However it was known that X-ray computed tomography (CT) images had been previously exploited quantitatively in soils. Particularly the variation of X-ray attenuation might be closely related to bulk density. A quantitative analysis of the CT images obtained for the project would then result in an independent estimate of initial void ratio for all the samples. That, in turn, would allow the reassessment of sample quality –which was the essential objective of the whole project- from a more secure basis.

1.2 OBJECTIVES

Accordingly the present thesis started with two separate objectives:

- The main objective was to exploit in a quantitative way the CT scan images obtained from the different samplers to obtain density measurements. To achieve this objective it was necessary:

  o To understand the fundamental aspects of computed tomography.
  o To review the state of art of the computed tomography as applied to geosciences.
  o To identify artifacts and errors in the previously obtained images that would impede quantitative interpretation
  o To eliminate those errors by adequate post processing
  o To set up a dedicated calibration testing program

- o To apply the calibration results to the previously obtained images
- The second objective was to review the sample quality assessment performed for the previous project. To achieve this objective it was necessary:
    - o To understand the sample disturbance criterion used in the Soft Soil Project.
    - o To review the laboratory test results of the Soft Soil Project to identify possible mistakes (including but not only these affecting specimen density).
    - o To reclassify the test specimens taking into account all the information from the lab and the CT scans.
    - o To establish if the classification newly attained for all the specimens was consistent with the laboratory tests results.

1.3 MASTER THESIS LAYOUT

This memory is structured as follows:

Chapter 2 covers the state-of-art, equipment and methodology of the X-ray computed tomography, including the specifications of the CT scan, the scanning method, the CT scan output, the artifacts on the results and some examples of their application on geoscience.

In the Chapter 3, the CT scanning parameters are studied, and its influence on the results quality. This chapter also includes a brief introduction about the post-process imaging software.

Chapters 4 and 5 cover the sampling campaign and part of the experimental program related to the Soft Soil Project. The characterization of the Castello Soil is also included.

In the Chapter 6, the calibration process of the CT scan, the analysis of the results, the artifacts treatment of the reference CT scans (of the Soft Soil Project samplers), the results and analysis of the reference CT scans are summarized.

Chapter 7 covers the reviewing of the sample quality classification of the Soft Soil Project and the analysis of the coherence using the results of the laboratory tests.

On chapter 8, conclusions and main results of the study are summarized.

Chapter II. X-RAY COMPUTERIZED TOMOGRAPHY

2.1 INTRODUCTION

X-ray computerized tomography (CT) is a nondestructive technique that allows three-dimensional visualization of internal structures of samples, determined mainly by variations in their density and atomic composition. CT (example of apparatus on Figure 1) was originally developed as a medical imaging technique in the early 1970s (Hounsfield, 1972, 1973), and the application of the technique to geoscience studies began in the early 1980s. Several publications show the possibility for use of this technique in geology and engineering studies, such as in soil science (Petrovic et al., 1982; Hainsworth & Aylmore, 1983), meteorites (Arnold et al., 1982), petroleum geology (Vinegar, 1986; Vinegar & Wellington, 1986), paleontology (Haubitz et al., 1988), geotechnics (Raynaud et al., 1989), and sedimentology (Kenter, 1989). These studies have clearly demonstrated the power of in geological research. However, one disadvantage of classical medical CT is that resolution is too low (lowest order of magnitude: 60 μm x 60 μm x 1 mm) for detailed geological research, such as reservoir appraisal. Since the 1990s, microfocus CT (μCT) (Auzerais et al., 1996) has been used to characterize porous media such as clastic, carbonate, volcanic and metamorphic rocks (Carlson & Denison, 1992; Ketcham & Carlson, 2001; Van Geet et al., 2001; Ketcham & Iturrino, 2005; Goldstein et al., 2007; Remeysen & Swennen, 2008), to investigate the void ratio evolution inside a shear band (Desrues et al., 1996) and others applications in geosciences field. The μCT utilizes a microfocal source that makes it possible to scan small objects with a spatial resolution down to 10 μm (Flannery et al., 1987; Van Geet et al., 2000; Cnudde et al., 2006).

Figure 1. Photograph of a CT scanner (Siemens Somatom Spirit ®). Extract from medical siemens website.

2.2   ESSENTIALS OF COMPUTED TOMOGRAPHY

The imaging process can be summarized as follows. The object is placed on a table (see Figure 1) whose movement can be accurately controlled. An X-ray source generates a continuous beam of X-rays, the beam passes through the object until the detector. The rotation of the source and detectors (gantry, see Figure 1) determines a virtual section through the sample whose thickness is roughly equal to the diameter of the radiation beam. As result of the reconstruction algorithm, this section is decomposed into voxels (an acronym for volume element), having a prismatic shape (see Figure 3b). The height of the voxel is equal to the attenuation width of the x-ray beam and is characterized by an average value of the linear attenuation coefficient (expressed in HU or CTN). Further, to each voxel (usually there are 512x512 voxels) a pixel of image can be attributed (see Figure 2) whose shades of gray are proportional to the corresponding numerical value of the attenuation coefficient. Finally, there results a two-dimension map representing the distribution of the linear attenuation coefficient over the entire section, whose spatial resolution is equal to the voxel size. This picture, which represents the reconstruction of the distribution function of the μ coefficient by means of its projection, is the final CAT image. Output format of CAT image is called DICOM (Digital Imaging and Communication in Medicine).
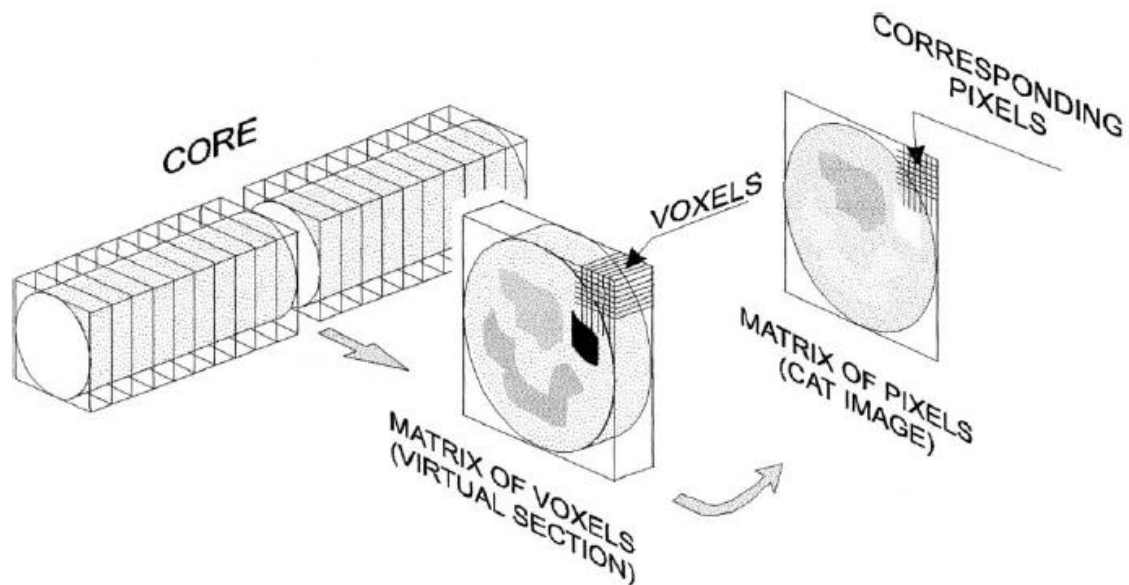
Figure 2. Schematic representation of the relation between the investigated object and its CAT image. (after Wellington & Vinegar, 1987, modified by Duliu,1999).

(a) X-Ray virtual section   (b) Voxel
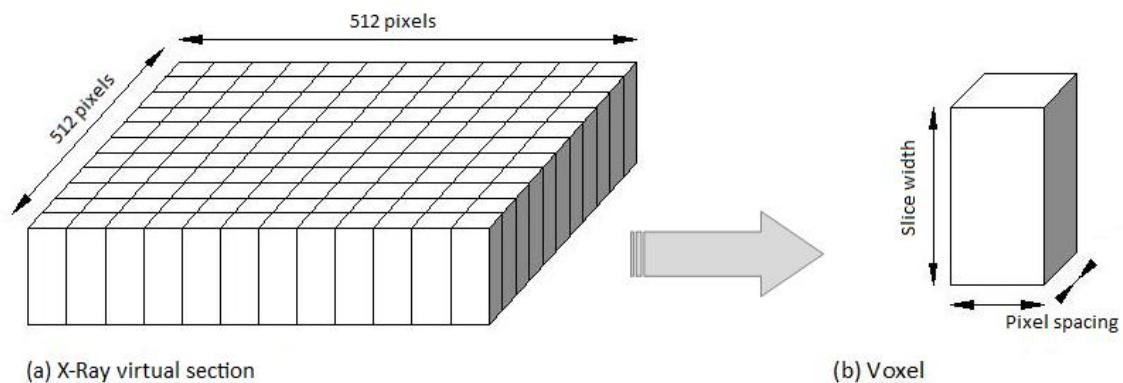
Figure 3. Concept of X-Ray CT virtual section and voxel.

By assembling together a great number of consecutive and parallel CAT digital images, it results in a complete three-dimensions matrix of data containing the distribution of the attenuation coefficient over the entire object. In order to reveal as many as possible details, these data can be subsequently used to obtain new CAT images following any desired section.

2.2.1 THE DEVELOPMENT OF CT SCANNERS

The majority of the CT scanners in use are classified to five generations, which mainly differ in mechanical configuration of the equipment, the relative motion of the scanned object, the x-ray source, the detectors, and the amount of the x-ray energy (Figure 4). The type of the scanner will influence the CT image quality, and scanning times, therefore, a tradeoff between the scanning time and quality (resolution) of the images must take place. For example in the medical field the patient is required to remain motionless until the scanning process is finished, therefore, time is a very important factor in medical CT. Moreover, the amount of energy to be used must be low to be tolerated by the human body. On the other hand, in industrial CT time is a less important factor and better quality images could be obtained utilizing the availability of a greater scanning time. Higher energies could be used without affecting the scanned object. (Kropas-Hughes et al. 2000).

First generation CT scanners use a single x-ray source and a single detector, this geometry is called: Parallel Beam Geometry. Multiple measurements of the x-ray transmission are obtained using a single highly collimated x-ray pencil beam and detector (Yoshikawa, 2004). The x-ray source and detector are translated along the scanned object to obtain a single view, and then they are rotated to obtain another view. Then all the views are collected to build a slice. This is called a "Translation-Rotation" motion which yields good quality images but it needs a very long time to perform.

Second generation CT scanners use the same "Translation-Rotation" motion but instead of having a single x-ray beams, a fan beam of radiation and a linear array of detectors are used. This enables the scanner to obtain multiple views of the object within a single translation, resulting in reducing the scanning time by about 10 times for each slice (Kropas-Hughes et al. 2000).

In third generation CT scanner, a curved detector array containing a large number of detectors is used with the x-ray source to obtain a complete view of the object without translation. Multiple views are obtained by the rotation of the source and the detector arrays around the object. This is called a "Rotate only" motion, and it reduces the scanning time to a small fraction of the time needed by the first two generations. In this type of scanners, the quality (resolution) of the obtained images, depend mainly on the number and size of the sensors in the detector. Therefore, a very large number of sensors has to be used in order to get an acceptable quality for the images.

Fourth generation CT scanners also use the "Rotate only" motion, but it is different from the third generation since it uses a stationary circular array of detectors. The source rotates around the body shooting a wide fan beam of x-ray. A view is made by obtaining successive absorption measurements of a single detector at successive positions of the x-ray source. These scanners are faster and have a better artifacts resistance than the other CT scanners, but they are more susceptible to scattered radiation (Yoshikawa, 2004).

Fifth generation CT scanners are different than all the other scanners since no motion is involved. In this scanner, a circular array of x-ray sources, which are electronically turned on and off is used. The detectors in this scanner are substituted by a large florescent screen so that when an x-ray source is switched on, a large volume of the object is imaged simultaneously. This scanner acquires two dimensional projections of three dimensional objects rather than the one dimensional projections of two dimensional objects. The

projection data can be acquired in approximately 50 ms (Yoshikawa, 2004), which is fast enough the image the moving parts like a beating heart, therefore, this scanner is used mostly in the medical field rather than the industrial applications.
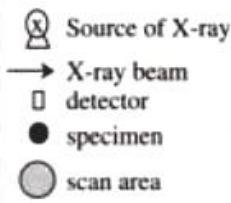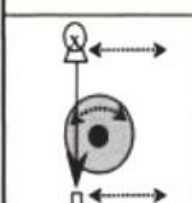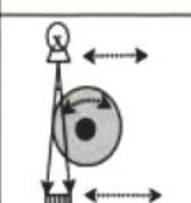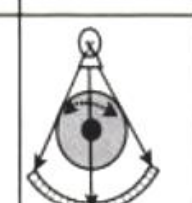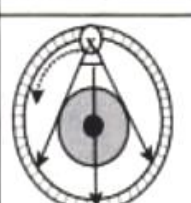
Scan type	1st generation (Translate-Rotate)	2nd generation (Translate-Rotate)	3rd generation (Rotate-Rotate)	4th generation (Stationary-Rotate)
☒ Source of X-ray → X-ray beam ▯ detector ● specimen ◯ scan area				
X-ray beam Angular aperture	0° Parallel beam	3°~30° Narrow fan beam	30°~40° Wide fan beam	30°~40° Wide fan beam
Number of detectors	1	3~60	500~600	1000~2000
Scanning time	4~5 min.	20~120 sec.	3~10 sec.	1~10 sec.

Figure 4. Several types of CT scanners. Extract from Otani (2004).

2.3 DESCRIPTION OF SCANNING PROCESS

2.3.1 SCANNING CONFIGURATION

The simplest common elements of X-ray radiography are an X-ray source, an object to be imaged through which the X-rays pass, and a series of detectors that measure the extent to which the X-ray signal has been attenuated by the object (Figure 4).

The fundamental principle behind computed tomography is to acquire multiple sets of views of an object over a range of angular orientations. By this means, additional dimensional data are obtained in comparison to conventional X-radiography, in which there is only one view. These data are used to create two-dimensional images that are called slices because they correspond to what would be seen if the object were sliced along the scan plane.

2.3.2 X-RAY SOURCE

The important variables that determine how effective an X-ray source will be for a particular task are the size of the focal spot, the spectrum of X-ray energies generated, and the X-ray intensity. The focal-spot size partially defines the potential spatial resolution of a CT system by determining the number of possible source–detector paths that can intersect a given point in the object being scanned. The more such source–detector paths there are, the more blurring of features there will be. The energy spectrum defines the penetrative ability of the X-rays, as well as their expected relative attenuation as they pass through materials of different density. Higher-energy X-rays penetrate more effectively than lower-energy ones, but are less sensitive to changes in material density and composition. The X-ray intensity directly affects the signal-to-noise ratio and thus image clarity.

The energy spectrum generated is usually described in terms of the peak X-ray energy (keV or MeV), but actually consists of a continuum in which the level with maximum intensity is typically less than half of the peak (Figure 5). According to Ketcham & Carlson (2001) the total ''effective'' spectrum is determined by a number of factors in addition to the energy input of the X-ray source itself, including autofiltering both by absorption of photons generated beneath the surface of a thick target (Silver, 1994) and by passage through the tube exit port; other beam filtration introduced to selectively remove low-energy X-rays; beam hardening in

the object being scanned; and the relative efficiency of the detectors to different energies. As discussed below, changes in the X-ray spectrum caused by passage through an object can lead to a variety of scanning artifacts unless efforts are made to compensate for them.
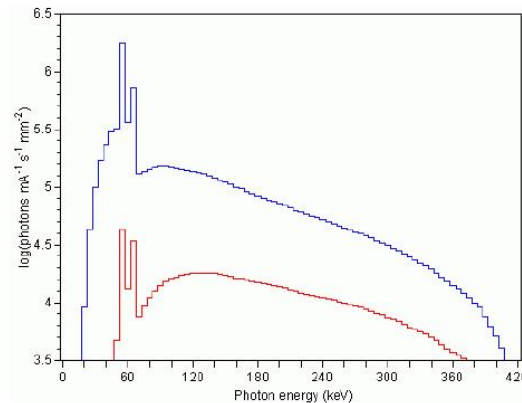
Figure 5. Theoretical energy spectra for 420-KV W-ray source. Upper spectrum is modified only by inherent beam filtration by 3 mm of aluminum. Mean X-ray energy is 224 KeV. Lower curve represents spectrum that has also passed through 5cm of quartz. Preferential attenuation of low-energy X-ray causes average energy to rise to 178 KeV (from Ketcham & Carlson, 2001).

2.3.3 X-RAY ATTENUATION

When the X-ray hit the object only part of the photons go through the material. The rate of removal of photons from the original X-ray is a function of the linear attenuation coefficient (μ) which depends on the photon energy (X-ray energy), the chemical composition, and physical density of the material (Amersham Health, 2003). X-ray interaction with matter is a function of the material density, the material thickness, and the X-ray energy. Dense materials (i.e., materials with high atomic numbers) attenuate more the X-ray beam energy than less dense materials and this difference in attenuation provides the contrast that forms the image. The capacity of X-rays to penetrate an object is highly material dependent. The number of photons, i.e., the radiation intensity along the incident direction, decreases exponentially while the X-ray passes through the object along the incident direction, as each photon is removed individually from the incident beam by an interaction. This attenuation is due to both absorption and scattering, as discussed in the following paragraphs.

As mentioned above when the X-rays pass through the object, the signal is attenuated. The basic equation for attenuation of a monoenergetic beam through a homogeneous material is given by Beer-Lambert's law as follows:

$$I = I_0 \cdot exp[-\mu x]$$ Equation 1

where I_0 is the initial or incident X-ray radiation, μ is the linear attenuation coefficient of the material, x is the length of the X-ray path through the material and I is the transmitted radiation. Figure 6 shows a schematic illustration of photons passing through an object of thickness x with a constant attenuation coefficient μ.
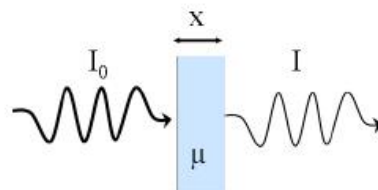
Figure 6. Schematic illustration of X-ray attenuation for a homogeneous object with a monochromatic beam.

Linear attenuation coefficients are expressed in units of inverse centimeters (cm^{-1}) and are proportional to the density ρ of the absorber. It is, therefore, common to express the attenuation property of a material in terms of its mass attenuation coefficient μ/ρ in units of cm^2/g.

If the scan object is composed of a number of different materials, the equation becomes:

$$I = I_0 \cdot exp\left[\sum_i (-\mu_i x_i)\right] \qquad \text{Equation 2}$$

where each increment is reflects a single material with attenuation coefficient μ_i over a linear extent x_i. To take into account the fact that the attenuation coefficient is a strong function of X-ray energy, the complete solution would require solving the equation over the range of the effective X-ray spectrum (Ketcham & Carlson, 2001), as follows.

$$I = \int I_0 (E) exp\left[\sum_i (-\mu_i(E) x_i)\right] dE \qquad \text{Equation 3}$$

There are three dominant physical processes responsible for attenuation of an X-ray signal (Ketcham & Carlson, 2001): photoelectric absorption, Compton scattering, and pair production. Photoelectric absorption occurs when the total energy of an incoming X-ray photon is transferred to an inner electron, causing the electron to be ejected (Figure 7). In Compton scattering, the incoming photon interacts with a free or loosely bound electron, ejecting the electron and losing only a part of its own energy, after which it is deflected in a different direction. In pair production, the photon interacts with a nucleus and is transformed into a positron-electron pair, with any excess photon energy transferred into kinetic energy in the particles produced.
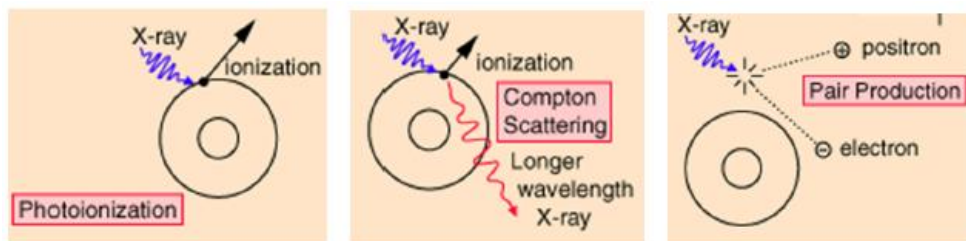
Figure 7. The three dominant physical processes of X-ray attenuation. (a) photoelectric effect; (b) Compton scattering; (c) pair production (Nave, 2010).

For geomaterials, photoelectric absorption is generally the dominant attenuation mechanism at low X-ray energies (up to 50-100 keV), while at higher energies (up to 5-10 MeV) Compton scattering is dominant (Duliu, 1999), after which pair production predominates (see Figure 8). Thus, unless higher-energy sources are used, only photoelectric absorption and Compton scattering need to be considered. The practical importance of the distinction between mechanisms is that photoelectric absorption is proportional to Z^4 - Z^5 (where Z is the atomic number), whereas Compton scattering is proportional only to Z (Markowicz, 1993). Consequently low energy X-rays are more sensitive to variations in composition than higher energy X-rays (Ketcham & Carlson, 2001). The distinction between absorption and scattering is important as each of these attenuation mechanisms affects the final image in a different way. Barrett & Swindell (1981) highlight the negative impact that scattered photons can have on the quality of the obtained image. In fact, a scattered photon has lost its "memory" regarding its direction of travel and therefore cannot be expected to cast a sharp shadow image on the

detector, instead they form a broad, diffuse distribution on the detector, impairing the image contrast.
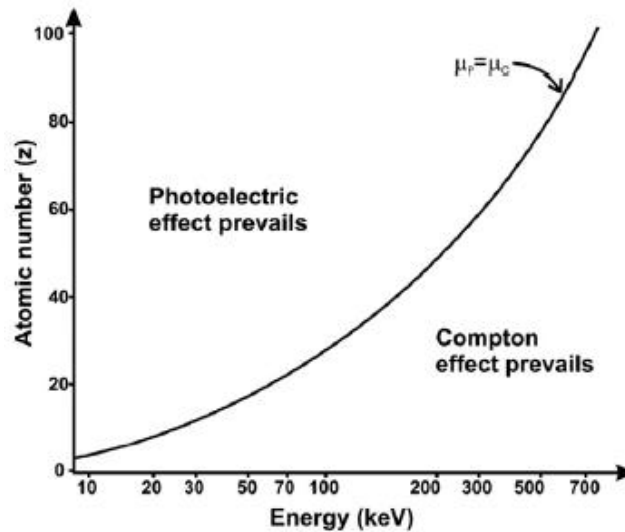
Figure 8. Repartition of the photoelectric and the Compton effects in function of the energy and the atomic number. Extract from Duchesne et al. (2009).

According to Ketcham & Carlson (2001), the best way to gain insight into what one might expect when scanning a geological sample is to plot the linear attenuation coefficients of the component materials over the range of the available X-ray spectrum. These values can be calculated by combining experimental results for atomic species (e.g., Markowicz, 1993). Alternatively, mass attenuation coefficients (μ/ρ) can be obtained from the XCOM database managed by The National Institute of Standards and Technology (NIST) website. Mass attenuation coefficients must be multiplied by mass density to determine linear attenuation coefficients. To illustrate, Ketcham & Carlson (2001) create Figure 9 which shows curves for four minerals: quartz, orthoclase, calcite, and almandine garnet.
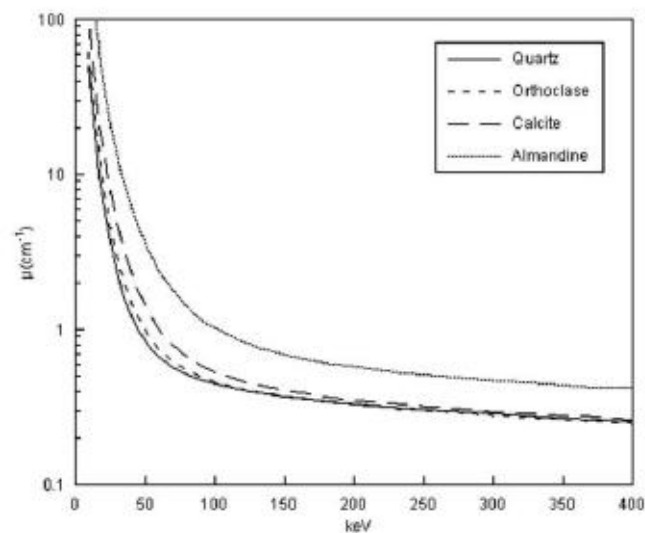
Figure 9. Linear attenuation coefficient as function of X-ray energy for four rock-forming minerals. Such curves, when combined with the X-ray spectrum utilized for scanning, allow prediction of ability to differentiate between minerals in CT images. Extract from Ketcham & Carlson (2001).

Quartz and orthoclase are very similar in mass density (2.65 g/cm^3 vs. 2.59 g/cm^3), but at low energy their attenuation coefficients are quite different because of the presence of relatively high-Z potassium in the feldspar. With rising X-ray energy, their attenuation coefficients

converge, and at approximately 125 keV they cross; above ~125 keV quartz is slightly (but probably indistinguishably) more attenuating, owing to its higher density. Thus, one would expect that these two minerals could be differentiated in CT imagery if the mean X-ray energy used is low enough, but at higher energies they would be nearly indistinguishable (Figure 10). Calcite, though only slightly denser (2.71 g/cm^3) than quartz and orthoclase, is substantially more attenuating, owing to the presence of calcium. Here the divergence with quartz persists to slightly higher energies, indicating that it should be possible to distinguish the two even on higher-energy scans. High-density, high-Z phases such as almandine are distinguishable at all energies from the other rock-forming minerals examined by Ketcham & Carlson (2001).
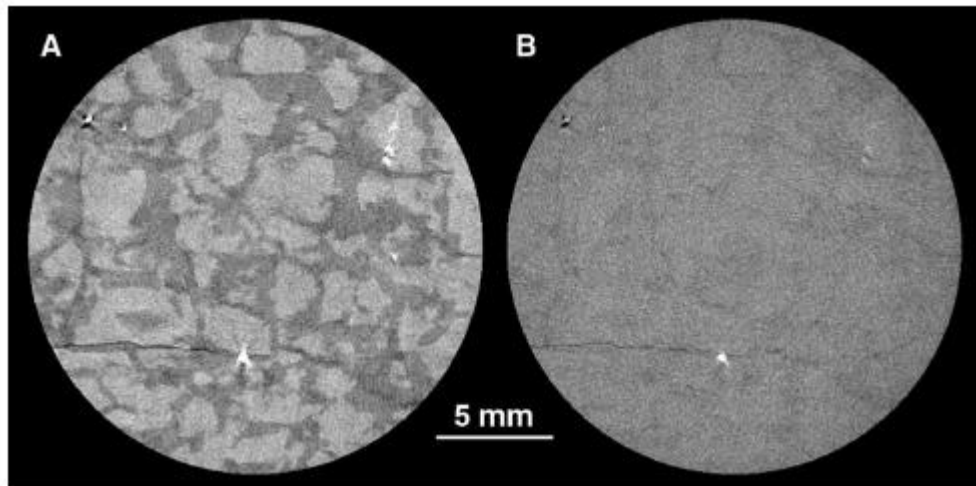
Figure 10. Core of graphic granite imaged at various energy conditions. Scan (A) was created using X-ray energy of 100keV and scan (B) was adquired with X-ray energy of 200keV. Extracted from Ketcham & Carlson (2001).

As well, Otani et al. (2010) mentioned that using lower X-Ray energy higher contrast is probably obtained. To illustrate this, Otani et al. (2010) tested the same sample with three different X-ray energy, and plot histograms of the obtained CT-values (see Figure 11).
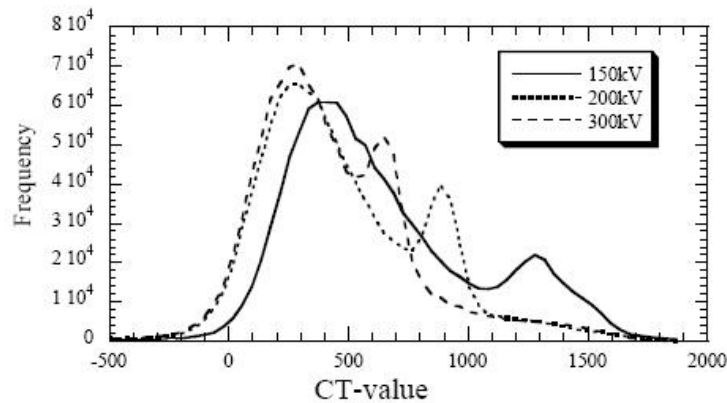
Figure 11. Voltage influence. Extract from Otani et al. (2010).

2.3.4 X-RAY DETECTORS

Detectors for CT scanners make use of scintillating materials in which incoming X-rays produce flashes of light that are counted. Detectors influence image quality through their size and quantity, and through their efficiency in detecting the energy spectrum generated by the source. The size of an individual detector determines the amount of an object that is averaged into a single intensity reading, while the number of detectors determines how much data can be gathered simultaneously.

In third-generation scanning, the number of detectors also defines the degree of resolution possible in a single view, and thus in an image overall. The film used in conventional X-ray radiography is an excellent detector in that it consists, in essence, of a very large number of small and sensitive detectors. Unfortunately, it is not amenable to quickly producing the digital data needed for computed tomography.

The efficiency of scintillation detectors varies with Xray energy, precisely because higher-energy X-rays are more penetrative than lower-energy ones, indicating that they are more capable of traveling through materials without interactions. This factor must be taken into account when determining the level of expected signal after polychromatic X-rays pass through materials.

2.3.5   RESOLUTION OF A CT SCANNER

The resolution of a CT scanner at the object is determined by the source and detector dimensions and the position of the object under test with respect to them (Bossi et al., 1990). The spatial resolution and the density resolution are two different things, but are related in a complex way. A method for estimating the scanner's density resolution is follow the recommendation of McCullough et al. (1976), which used CT scans of distilled water to compute its standard deviation. Since distilled water is a homogeneous substance, only cause of local error is the noise of the apparatus (dominated by quantic noise of the source). Scanner noise as given by the standard deviation statistic is equivalent to the density resolution of the scanner. However, when heterogeneous specimens are measured, the spatial resolution plays a role in the local measurement. The spatial resolution of an imaging system is the parameter that specifies how far apart two very small high-contrast objects must be to be detected as separate in the displayed image.

2.3.6   DATA ACQUISITION

2.3.6.1   Sample preparation

Strictly speaking, the only preparation that is absolutely necessary for CT scanning is to ensure that the object fits inside the field of view and that it does not move during the scan. Because the full scan field for CT is a cylinder (i.e., a stack of circular fields of view), the most efficient geometry to scan is also a cylinder (Ketcham & Carlson, 2001). Thus, when possible it is often advantageous to have the object take on a cylindrical geometry, either by using a coring drill or drill press to obtain a cylindrical subset of the material being scanned, or by packing the object in a cylindrical container with either X-ray-transparent filler or with material of similar density. For some applications the sample can also be treated to enhance the contrasts that are visible. Examples have included injecting soils and reservoir rocks with NaI-laced fluids to reveal fluid-flow characteristics (Wellington & Vinegar, 1987; Withjack, 1988), injecting sandstones with Woods metal to map out the fine-scale permeability, and soaking samples in water to bring out areas of differing permeability, which can help to reveal fossils (Zinsmeister & De Nooyer, 1996).

2.3.6.2   Calibration

Calibrations are necessary to establish the characteristics of the X-ray signal as read by the detectors under scanning conditions, and to reduce geometrical uncertainties. The latter calibrations vary widely among scanners. The two principal signal calibrations are offset and gain, which determine the detector readings with X-rays off, and with X-rays on at scanning conditions, respectively. An additional signal calibration, called a wedge, used on some third-generation systems consists of acquiring X-rays as they pass through a calibration material over a 360° rotation. The offset-corrected average detector reading is then used as the baseline from which all data are subtracted. If the calibration material is air, the wedge is

equivalent to a gain calibration. A typical non-air wedge is a cylinder of material with attenuation properties similar to those of the scan object. Such a wedge can provide automatic corrections for both beam hardening and ring artifacts (described later), and can allow utilization of high X-ray intensities that would saturate the detectors during a typical gain calibration. Although widely employed in medical systems, which use phantoms of water or waterequivalent plastic to approximate the attenuating properties of tissue, the wedge calibration is relatively uncommon in industrial systems.

2.3.6.3 Collection

The principal variables in collection of third-generation CT data are the number of views and the signal acquisition time per view. In most cases, rotation is continuous during collection.

Each view represents a rotational interval equal to 360° divided by the total number of views. The raw data are displayed such that each line contains a single set of detector readings for a view, and time progresses from top to bottom. This image is called a sinogram, as any single point in the scanned object corresponds to a sinusoidal curve. Second-generation CT data are collected at a small number of distinct angular positions (such as 15 or 30), but the progression of relative object and source–detector position combinations allows these data to complete a fairly continuous sinogram.

2.3.6.4 Reconstruction

Reconstruction is the mathematical process of converting sinograms into two-dimensional slice images. The most widespread reconstruction technique is called filtered backprojection, in which the data are first convolved with a filter and each view is successively superimposed over a square grid at an angle corresponding to its acquisition angle. The Shepp-Logan filter (Shepp & Logan, 1974), which is used more frequently in medical systems and reduces noise at some expense in spatial resolution (ASTM, 1992).

During reconstruction, the raw intensity data in the sinogram are converted to computer tomograph numbers or CT values (measured in Hounsfield units) that have a range determined by the computer system.

$$CT\ number = \frac{(\mu_t - \mu_w)}{\mu_w} \cdot 1000 \qquad\qquad \text{Equation 4}$$

Where μ_t is the linear attenuation of the material and μ_w is the linear attenuation of water. The most common scale used to date has been 12-bit, in which 4096 values are possible. These values correspond to the grayscale in the image files created or exported by the systems. Although CT values should map linearly to the effective attenuation coefficient of the material in each voxel, the absolute correspondence is arbitrary.

According to this scale, air takes a CT number of -1000 HU while for water this value is equal to 0 HU. Hence, each CT number corresponds to a change of the linear attenuation coefficient equal to 0.1%, i.e., 1 kg/m^3 for water. Consequently, the greater the value of the μ coefficient is, the higher the corresponding CT number is. This determines one of the most important property of the reconstructed image, i.e., the representation of the attenuation coefficients over a linear scale. Industrial CT systems are sometimes calibrated so that air has a value of 0 HU, water of 1000 HU, and aluminum of 2700 HU, so the CT number corresponds roughly with density (Johns et al., 1993). The calibration of CT values is straightforward for fixed-geometry, single-use systems, but far less so for systems with flexible geometry and scanning modes, and multiple uses each requiring different optimization techniques.

Although a link to a reference scale can be useful in some circumstances, the chemical variability of geological materials and the wide range of scanning conditions used preclude any

close correspondence to density in most cases. Furthermore, because material components can range from air to native metals, a rigid scale would be counterproductive. Given the finite range of CT values, a single scale may be insufficiently broad if there are large attenuation contrasts, or needlessly desensitize the system if subtle variations are being imaged. For geological purposes, it is commonly more desirable to select the reconstruction parameters to maximize the CT-value contrast for each scanned object. According to Ketcham & Carlson (2001) this can be done by assigning arbitrary low and high values near the limits of the available range to the least and most attenuating features in the scan field. In general we try to ensure that no CT value is generated beyond either end of the 12-bit range, lest some dimensional data be lost. For example, the boundary of an object being scanned in air is usually taken to correspond to the CT-value average between the object and air. If air is assigned to a CT value below zero, the apparent boundary of the object may shift inward.

2.3.7   ANALYSIS OF THE SCANS

Although the output of computed tomography is visual in nature and thus lends itself to straightforward interpretation, subtle complications can render the data more problematic for quantitative use. Scanning artifacts can obscure details of interest, or cause the CT value of a single material to change in different parts of an image. Partial-volume effects, if not properly accounted for, can lead to erroneous determinations of feature dimensions and component volume fractions. In this section discuss commonly encountered problems, and some approaches for solving them.

2.3.7.1   Artefacts

An artifact can be defined as any information in the CT image that does not reflect the actual composition of the scanned object. Many types of artifacts are encountered during a CT scan. Artifacts in a CT image can be originated by many factors like the characteristics of the scanned object including its shape and chemical composition, the x-ray nature, the detectors quality, and the resolution of the system.

- Beam hardening

The most frequently encountered artifact in CT scanning is beam hardening or cupping artifact (Ketcham & Carlson, 2001), which causes the edges of an object to appear brighter than the center, even if the material is the same throughout (Figure 12). The artifact derives its name from its underlying cause - the increase in mean X-ray energy, or ''hardening'' of the X-ray beam as it passes through the scanned object. Because lower-energy X-rays are attenuated more readily than higher-energy X-rays, a polychromatic beam (which is an x-ray whose spectrum contains photons with different energies) passing through an object preferentially loses the lower energy parts of its spectrum. The end result is a beam that, though diminished in overall intensity, has a higher average energy than the incident beam (Figure 5), in other words, it is hardening. This also means that, as the beam passes through an object, the effective attenuation coefficient of any material diminishes, thus making short ray paths proportionally more attenuating than long ray paths. In X-ray CT images of sufficiently attenuating material, this process generally manifests itself as an artificial darkening at the center of long ray paths, and a corresponding brightening near the edges. In objects with roughly circular cross sections this process can cause the edge to appear brighter than the interior, but in irregular objects it is commonly difficult to differentiate between beam hardening artifacts and actual material variations.
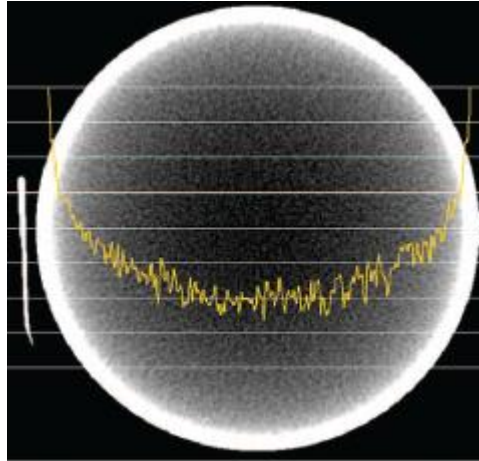
Figure 12. Slice and profile of the CT numbers obtained across the center of a uniform water phantom. Extract from Barret et al. (2004).

Beam hardening can be a pernicious artifact because it changes the CT value of a material (or void) depending upon its location in an image. Thus, the attempt to utilize a single CT number range to identify and quantify the extent of a particular material can become problematic. One measure that is sometimes taken is to remove the outer edges of the image and analyze only the center. Although this technique removes the worst part of the problem, the artifact is continuous and thus even subsets of the image are affected. Furthermore, if the cross-sectional area of the object changes from slice to slice, the extent of the beam-hardening artifact also changes, making such a strategy prone to error.

There are a number of possible remedies for beam hardening, ranging from sample and scanning preparation to data processing. The simplest approach is to use an X-ray beam that is energetic enough to ensure that beam hardening is negligible, and can thus be ignored. Unfortunately, most materials of geological interest are attenuating enough that beam hardening is noticeable unless the sample is quite small. Furthermore, high energy beams are less sensitive to attenuation contrasts in materials, and thus may not provide sufficient differentiation between features of interest (Stonestrom et al., 1981). Another possible strategy is to pre-harden (or post-harden) the X-ray beam by passing it through an attenuating filter (see Figure 13) before or after it passes through the scanned object (Ketcham & Carlson, 2001). Filters are normally flat or shaped pieces of metal such as copper, brass or aluminum. The drawback to beam filtration is that it typically degrades the X-ray signal at all energies to some degree, thus leading to greater image noise unless longer acquisition times are used. It is also characteristically only partially effective. Another method is to employ a wedge calibration using a material of similar attenuation properties to the object. To be effective, the wedge material should be cylindrical, and the scanned object should either be cylindrical or packed in an attenuating material (ideally the wedge material) to achieve an overall cylindrical form. If the latter is necessary, images may be noisier because of the additional X-ray attenuation caused by the packing material. The wedge material in the images also commonly interferes with 3-D analysis of the object of interest, in which case it must be eliminated during image processing.
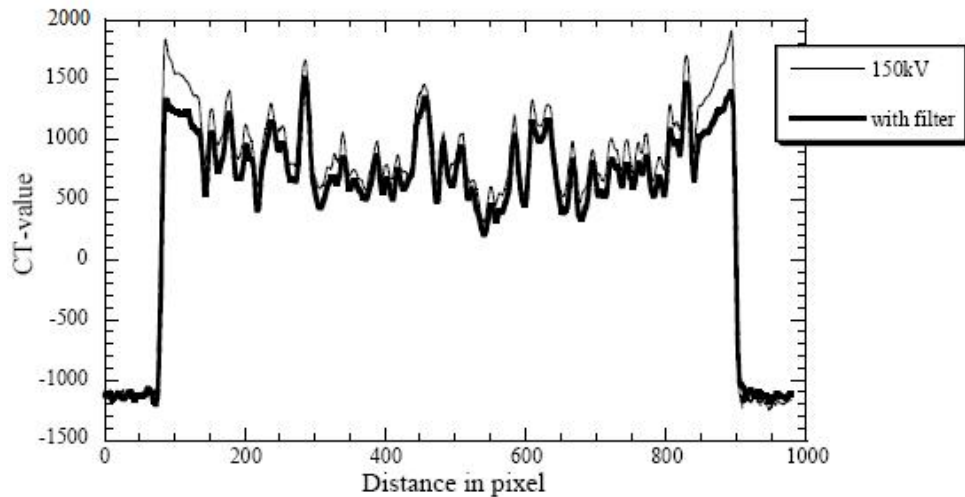
Figure 13. Filter effect over beam hardening artifact. Extract from Otani et al. (2010).

Beam hardening is characteristically more difficult to alleviate at the data-processing stage, and such measures are usually available only in special circumstances. If the scanned object is materially uniform, a correction can be applied to the raw scan data that converts each reading to a non-beam-hardened equivalent before reconstruction takes place; unfortunately, the requirement of uniformity is more often met in industrial applications than geological ones. If the object is cylindrical and fairly uniform (i.e., a rock core), it may be possible to construct an after-the-fact wedge correction by compiling a radial average of CT values for a stack of slices. A Fourier filter that removes long-wavelength variations in CT value has also been effective in some circumstances (Wevers et al. 2000).

- Ring artifacts

Ring artifacts are often observed in the computed tomographic (CT) images of modern scanners with solid-state detectors. In X-ray CT, ring artifacts are caused by imperfect detector elements such as a gain error at a specific position in the detector array (Ter-Pogossian, 1976). They appear on CT images as a number of dark concentric rings (see Figure 14) of one pixel width superimposed on the structures being scanned (Kinney, et al., 1989). As the grey levels in the reconstructed images are influenced by these ring artifacts, quantitative analysis becomes a major problem. Moreover, post processing such as noise reduction or image segmentation is significantly hampered by the presence of such artifacts. This problem is frequently raised while discussing medical CT image quality, especially third generation systems (Hiriyannaiah, 1997).

There are many causes for the appearance of ring artifacts, but all of them are associated with individual pixel response. In any case, the ring artifact, which manifests in the sinogram as a stripe artifact. In worst case, if some detector elements show severely reduced performance due to manufacturing defects, ring artifacts show up as circles with no gray level difference. In modern scanners, this situation is exceptional and detector elements are generally of high quality. However, their response to the incoming signal is usually not as expected due to the following reasons:

- drifts in detector element sensitivity in between white-field calibrations (e.g., caused by temperature instability);
- non-linear detector element response, caused by beam-hardening effects;
- drifts in the detector white-field correction caused by hardware short comings such as irregularities in the X-ray tube, different scintillator thicknesses, and errors in read-out electronics (Raven, 1998).

Depending on the cause and intensity of the ring artifact, impairment of the CT images by the ring artifacts may lead to severe degradation of the diagnostic quality of the tomographic images by obscuring characteristic features in the regions of interest (Ketcham 2006).
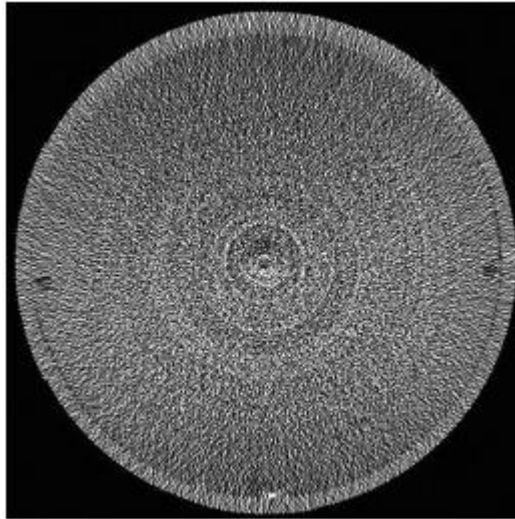
Figure 14. CT image of water-filled phantom with ring artifacts. Extract from Barret et al. (2004)

Though a number of ring artifact reduction techniques have been reported in the literature, according to Mohammad et al. (2010), no single technique is optimum in dealing with different sources causing the ring artifacts. The moving average (MA) and median filtering-based methods (Ketcham 2006, Boin & Haibel 2006) are only suitable for removing constant bias in the response of the pixels due to mis-calibration. The detector array moving technique (Davis & Elliott 1997) can mask only the effect of non-uniform sensitivity of different detector elements at the cost of a special hardware (Doran 2001, Jenneson 2003). The 2D wavelet-based method presented in Tang et al (2001) has been designed to eliminate ring artifacts from a conebeam CT image. The performance of the very recently reported wavelet-Fourier method (Münch et al., 2009) significantly degrades when an image is particularly corrupted by a sharp ring of varying intensity. Most recently, works based on a center-weighted median filter (Sadi et al., 2010) and a morphological filter (Hasan et al., 2010) has been reported to eliminate the ring artifacts from a tomographic image. But these techniques do not classify types of rings to deal with them separately, which has been found to be a prerequisite to an effective ring removal technique (Mohammad et al., 2010). In Prell et al. (2009) two post-processing techniques, both using mean and median filtering but working in different geometric planes (i.e. polar and cartesian), are proposed for the correction of ring artifacts. The authors have shown that the algorithm in polar coordinate (RCP) is more effective than that in the cartesian coordinate for removing artifacts. Furthermore, Kyriakou et al. (2009) have shown that the RCP method can also remove ring artifacts from the micro-CT images. The method may, however, fail to effectively eliminate the often seen varying intensity rings in the images, because they generally contain significant high frequency information but the mean (low-pass) filtering in the RCP method is not appropriate to retain the correct varying intensity ring structures in the difference image and thereby may result in poor performance of the algorithm. Because of the complex nature of the problem, the ring artifact removal techniques need more improvement in all cases according to Mohammad et al. (2010), and also the residual artifacts after correction by the algorithms are not believed to be within the acceptable range in many instances.

- Atomic number effect

Until recently, authors (e.g. Wellington & Vinegar, 1987; Kawamura, 1990) have assumed that X-ray attenuation was linearly related to the density of the sample (Figure 15a). This is actually true for biological samples like the human body, but becomes more complex for plastic denser samples (McCullough, 1975). Kantzas et al. (1992) also noted that CT-number and density were correlated in sediment cores (Figure 15b), but the linear correlation was different among the samples. These authors interpreted this observation in term of "atomic number effect"; they suggested that when high atomic number elements were contained in the sediment, X-ray attenuation was higher than expected from the density alone. In fact, a simple linear relation between CT-number and density cannot be used (Kenter, 1989). Boespflug et al. (1994) analyzed selected samples of minerals and liquids (Figure 15c), which were free of pores and water. They showed that X-ray absorption of samples depends both upon density and mean atomic number, due to the occurrence of Compton scattering and photo-electric absorption. For example, the presence of Ca or Cl may enhance X-ray absorption, giving rise to a higher CT number. By using empirical equations, the contribution of each process may be estimated, yielding a linear relation between a "corrected" CT-number and sample density. Orsi et al. (1994) have found good agreement between bulk density determined by gamma-ray (GRAPE), and X-ray analysis.
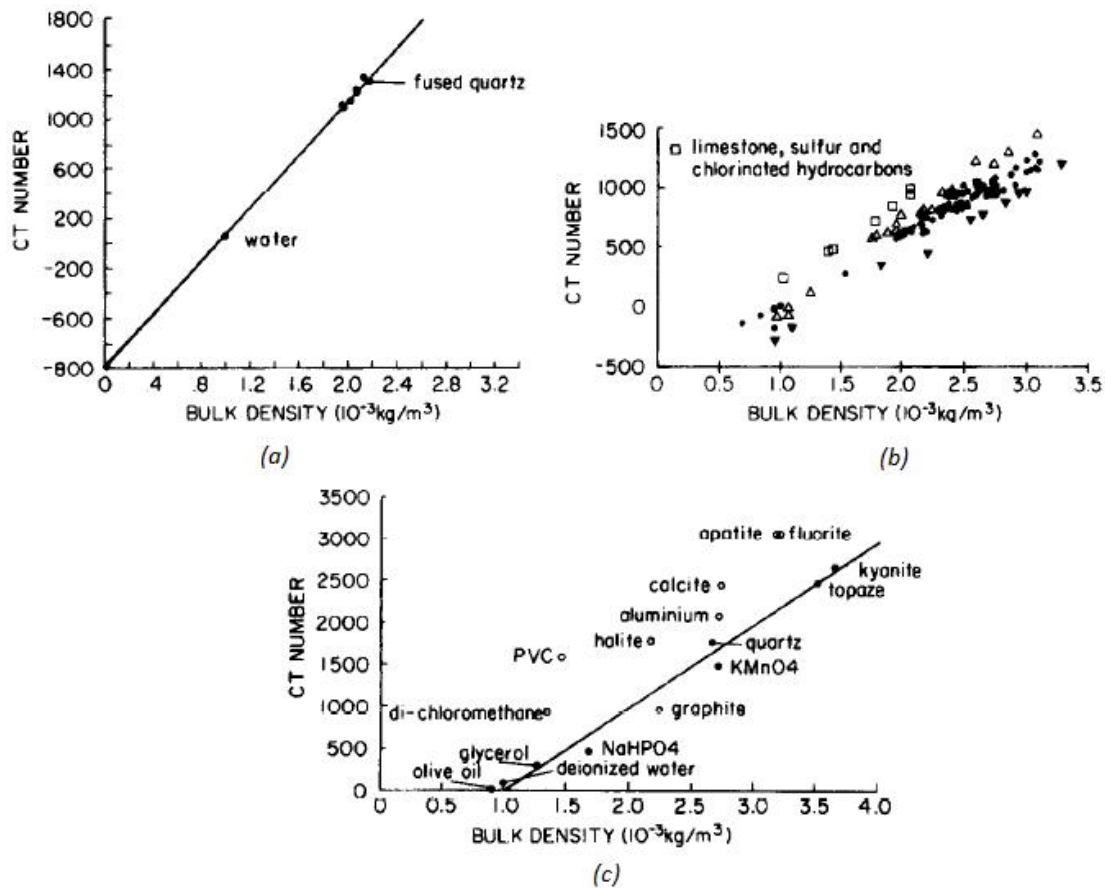
Figure 15. Comparison of CT number-density correlations reported from 1987 to 1994. (a) From Wellington & Vinegar (1987); (b) from Kantzas et al. (1992); (c) from Boespflug et al. (1994). Extract from Boespflug et al. (1995).

Boespflug et al. (1994) have shown that HU values are largely influenced by the atomic number effect. For the different compounds they used, photoelectric effect contribution ranges from 0 to 90% of the HU values. Concerning the minerals employed in their study, atomic number effect contribution varies from 11 to 38%. Thus, to obtain relative density values, it is

necessary to subtract this contribution from the HU values. To correct the atomic number effect, the absolute density ($\rho_{absolute}$) and the Z_{eff} of the samples were used in the equation:

$$HU_{photoelectric} = \left[\left(\frac{1 + K \cdot Z_{eff}^{n}}{1 + K \cdot Z_{eff}^{water}}\right) \cdot \rho_{absolute} - 1\right] \cdot 1000 \qquad \text{Equation 5}$$

in which $HU_{photoelectric}$ is the HU value corrected for the atomic number effect and K is a coefficient defined by

$$K = \frac{b}{a \cdot E^{3.2}} \qquad \text{Equation 6}$$

where b is a constant value of 9.8×10^{-24} $keV^{3.2}$, a is the Klein–Nishira coefficient and E is the energy in keV (Knoll, 1999; Garg et al., 1996).

However, quantitative information on X-ray absorption is not always very clear. Since it is related both to the bulk density of the sample and to the atomic number, the porosity of the material, the water content, and also the chemical composition must be taken into account. Presently, it is still preferable to consider the CT-number as a specific unit and to interpret its variation empirically.

- Other artifacts

A variety of other artifacts can arise in certain situations, like the ones caused by the motion of the scanned object, which produces the greatest degree of artifacts in the medical field (Strumas et al. 1995). Also, if a highly attenuating object is noncircular in cross-section, streaks that traverse the longest axes of the object can occur (Wevers et al. 2000). For example, a scanned cube of a dense material may have dark streaks connecting opposite corners. These streaks can intensify ring artifacts where they overlap, making remediation more difficult. If the scanned material includes features that are of much higher density (i.e. metal) than the surrounding matrix, a ''starburst'' artifact can form in which bright streaks emanate from the object for a short distance into nearby material, potentially obscuring features. In several instances have found that fossils have been repaired with steel pins, resulting in severe artifacts. Similar artifacts have been caused by crystals of sulfide or oxide minerals.

2.3.7.2   Partial volume effects

Because each pixel in a CT image represents the attenuation properties of a specific material volume, if that volume is comprised of a number of different substances then the resulting CT value represents some average of their properties. This is termed the partial volume effect. Furthermore, because of the inherent resolution limitations of X-ray CT, all material boundaries are blurred to some extent, and thus the material in any one voxel can affect CT values of surrounding voxels. Although these factors can make CT data more problematic to interpret quantitatively, they also represent an opportunity to extract unexpectedly fine-scale data from CT images. For example, medical CT data have long been used to trace two-phase fluid flow in soil and sedimentary rock cores (Wellington & Vinegar, 1987; Withjack, 1988), even though the fluids themselves appear only as subtle attenuation changes in the matrix they are passing through. Partial-volume effects have also been used to measure crack sizes in crystalline rocks (Johns et al., 1993) and pores in soil columns (Peyton et al., 1992) down to a scale that is considerably finer than even the pixel dimensions.

The interpretation of CT values in voxels containing multiple components is not necessarily straightforward. Wellington & Vinegar (1987) utilize the approximation that the CT value in a voxel containing two components is equal to a linear combination of the CT values of the two end-members according to their volumetric proportions, which provides a reasonable solution

if their attenuation values are fairly close (Pullan et al., 1981). If the end-member attenuation values are far different, as is the case for rock and void space, significant errors of 10% or more can result from this approximation if their boundary is nearly parallel with the scan plane. However, in most cases where randomly oriented voids are studied, this error is significantly lower, and is commonly neglected without large consequence (Johns et al., 1993; Kinney et al., 1993; Wellington & Vinegar, 1987).

Ketcham & Carlson (2001) showed an example of the possible utility of partial-volume effects in Figure 16. A core of limestone from the lower Ismay member of the Paradox Formation was scanned and subsequently cut for petrographic analysis. Individual fractures that appear on the scan were measured petrographically and found to have widths that were significantly smaller than the pixel dimensions. The fracture width can be estimated using partial volume calculations similar to those used by Johns et al. (1993), although at least one additional step is required to take fracture dip into account.
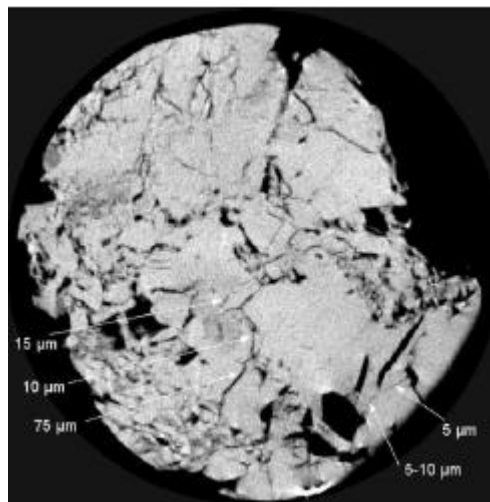
Figure 16. 100μm slice through fractured limestone from lower Ismay member of Paradox Formation. Extract from Ketcham & Carlson (2001).

Figure 17 illustrates the relation between soil particles and voxel dimension (Adopted Otani et al., 2002). This diagram indicates; (a) a soil particle is larger than size of a voxel, (b) a soil particle is larger than base area of a voxel and (c) a soil particle is much smaller than size of a voxel. Otani et al. (2002) investigated the relationship between voxel dimensions and pore space in the soil material and evaluated the pore size based on an X-ray CT binary image. Since the CT-value is proportional to the material density, the CT-value should be different in each situation in Figure 17.
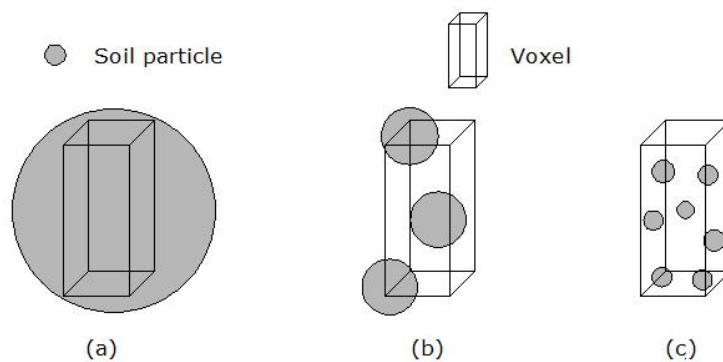
Figure 17. Factor of partial volume effect (Adopted Otani et al., 2002)

Figure 18 (a) and (b) show the distributions of CT-values on the CT image at the location showing two arrows for dry granite soil with mean-particles diameter of (a) .2.0 - 4.25 mm and (b) 75 - 106μm contained in a vinyl chloride mould (Otani et al., 2002). The CT-value of the granite particles is about 1000 to 1500 and those of the air voids among the particles are about -1000 (air). The variation of the CT-values in the distribution shown in Figure 18 (b) is less than that of the CT-value distribution as shown in Figure 18 (a). CT-values in Figure 18 (a) distinguish air voids (i.e. CT-value is -1000) from granite particles (i.e. 1000 to 1500) so that the mean CT-value to represent bulk density in a mould involves a large variety. Meanwhile, the case shown in Figure 18 (b) has rather smooth distribution of CT-values because the sizes of all the soil particles are much smaller than the size of resolution and thus, it is obvious that this case rather reflects the bulk density of the materials (Otani et al., 2002).

(a) Mean particle size: 2.0 – 4.25mm   (b) Mean particle size: 75 – 106μm
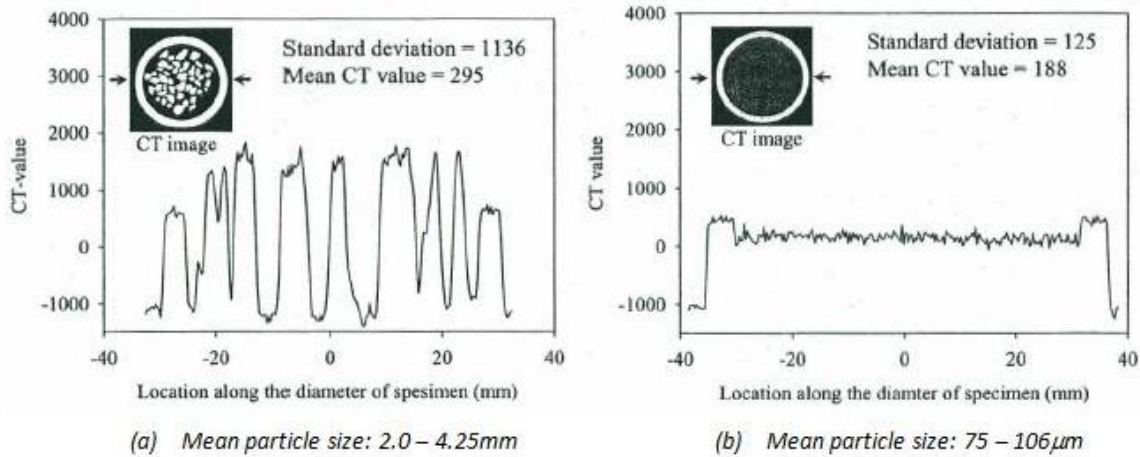
Figure 18. CT-value distribution of granite material. Extract from Otani (2010).

Figure 19 presents the relationship between CT-value and grain size investigated by Otani et al. (2002). Error bar means the variation of test results for three trials. As shown in Figure 19, CT-value increases in the grain size range of 425-2000μm, with greater standard deviation than that of 106-425μm grain size. The increase of CT value in the grain size of 425-2000μm is caused by the increase of grain size with respect to voxel size; namely, a voxel is partially occupied by particles with a grain size similar to voxel dimension (i.e. 850 - 2000μm). Thus, when the CT-value is converted to bulk density, the occupation ratio of grain size to a voxel dimension should be examined by calibrating CT-value and bulk density with each range of the grain size.
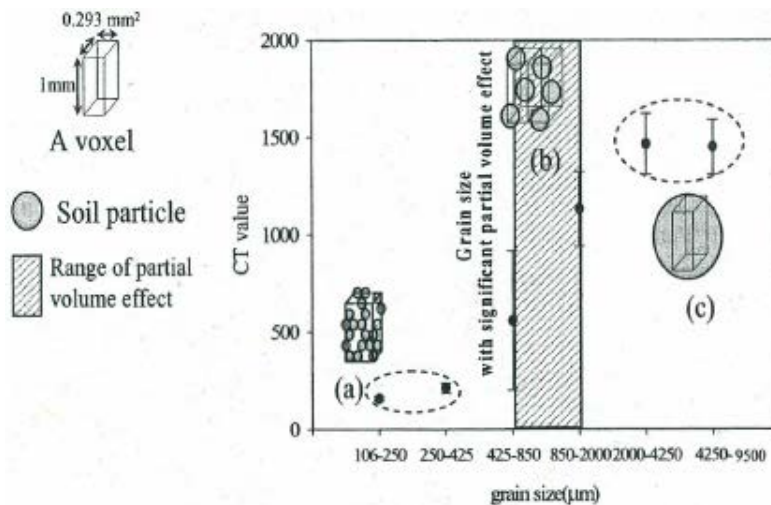
Figure 19. Relationship between CT-value and grain size by Otani et al. (2002).

Another consequence due to the presence of two or more materials lie in the area of the voxel (e.g. air and soil) is that the true structure of soil particles will not be represented (Mukunoki et al., 2003). This problem mainly appears when very small particle sizes are used in the CT scan, increasing the possibility of having more than one material within a voxel. Increasing the resolution of the system, in other words, reducing the size of the voxel will reduce the possibility of the partial volume artifacts, and the internal structure would be represented more accurately (Alramahi, 2004). It should be noted that increasing the spatial resolution will significantly increase the scanning time, and the size of the data sets, therefore, a tradeoff between these factors has to be considered.

2.4 CAT-ADVANTAGES AND LIMITATIONS

CAT represent a complete nondestructive imaging technique which can be used to investigate a large category of objects. The advantages of x-ray CT scanning include time savings and minimal sample disturbance. Tollner (1998) noted that x-ray CT scanning can provide aggregate size data consistent with traditional testing methods but without the time-consuming sample preparations involved with traditional tests. In particular, CT scan testing provides significant savings in time and effort when compared to sample coupon preparation techniques. The non-destructive nature of CT scanning allows the same soil sample to be scanned many different times. Since the sample is not affected by the testing, CT scanning provides an opportunity to investigate particle and pore interactions at any time and location within the sample. With the proper test equipment, CT scans could even be taken as a sample is loaded or experiencing changes in stress state or environment.

Generally, CAT has only few limitations. One of them is related to the capacity of the untrained human eye to distinguish between 16 shades of gray. In the case of CAT images, each of these shades corresponds to a variation of the attention coefficient of about 6%. This limit can be reduced by a further digitally image processing, but no less than 0.5% to 1%. In this way, CAT can evidences variations of the attenuation coefficients no smaller than this limit.

The other limitation of the CAT performances consists on a negative correlation between the values of the attenuation coefficient and the spatial resolution. Hence, the lower the attenuation contrast, the greater the linear size of minimum detectable detail is (Petrovici et al., 1982). CAT images thus obtained usually show a good spatial resolution up to 0.5mm (Siemens, 1991; Orsi et al., 1994; Amos et al., 1996) for an acquisition time of 2–6 s (Siemens, 1991; Coshell et al., 1994). This constraint can be avoided by replacing, the classical X-ray tubes either by a microfocal X-ray generators (Simons et al., 1997) or by a beam of synchrotron radiation whose diameter (0.05–0.1mm) increased the resolution to 10 to 100mm at a spatial frequency of between 50 and 670mm, close to classical radiographs (Hirano et al., 1990; Johns et al., 1993; Coles et al., 1995; Simons et al., 1997).

The use of medical CT equipped with intense X-ray tubes has the advantage of an extremely short running time (a few seconds and even less) but presents some disadvantages known as beam hardening and absorption edges effects (Herman, 1980). These effects which are intrinsically related to the polychromatic nature of the X-ray generated by classical tubes need special mathematical (Brooks & Di Chirico, 1976) or physical corrections. These corrections usually work well, but for some kind of samples, as soils, they cannot ensure perfect, free of artifacts CAT images (Petrovici et al., 1982; Tollner & Murphy, 1991).

Other principal limitations of the CAT applications do not exist.

2.5   SOME EXAMPLES OF APPLICATIONS

The following sections show some applications of the CT scanners outside the medical or industrial field.

2.5.1   CAT IN SOIL SCIENCE

Soil is a ubiquitous component of our environment. It consists of four major components, i.e., mineral matter, water, air and organic matter whose proportions are subject of a great variability, but are all characterized by low atomic numbers (7 to 15). Therefore, for photon energies greater than 30 keV, the Compton effect is predominant which implies a linear dependency between the linear attenuation coefficient and physical density of the soil (Cesareo et al., 1994) or between the attenuation coefficient and the moisture content (Cruvinel et al., 1989). At the same time, iron oxide and other heavy mineral components of the soil are characterized by significantly greater effective atomic numbers or densities. Hence, any mineralized component of the soil will be characterized by a larger linear attenuation coefficient and thus will be better distinguished on CAT images.

According to Duliu (1999), the soil investigation by CAT presents two major potential uses. The first one refers to the soil structure as pore distribution or local mineralization, while the second one permits a detailed investigation of the water content distribution and the water circulation around plant roots.

Concerning the first trend, CAT has been successfully applied to a direct and accurate determination of the spatial distribution and the total volume of pores (if microtomography is used) or macropores (Phogat & Aylmore, 1989; Grevers et al., 1989; Ketcham & Iturrino, 2005; Nakashima & Kamiya, 2007; Yanbin Yao et al., 2009; Lingtao Mao et al., 2012). Furthermore, CAT, due to its ability to reveal density changes of about 0.1%, proved to be useful method to characterize the degree of soil compactness.

Concerning the second trend, following a great volume of work meant to determine nondestructively and with high precision both the volumetric water content and the bulk density of soil columns by using the gamma-ray attenuation (Ferguson & Gardner, 1962; Soane, 1967; Cesareo et al., 1994; Orsi, 1994; Amos et al., 1996; Soh, 1997; Van Geet et al., 2000; Duchesne et al., 2009; Tanaka et al., 2011) (see Figure 20). In this way, it has been proved that the spatial resolution of CAT permits a good reconstruction of the soil pore system as well as of the 3-D changes of the soil bulk density (Petrovici et al., 1982). These measurements have proved that the attenuation of low-energy gamma- or X-ray can be used for a quantitative determination of density for both dry and water saturated soils.
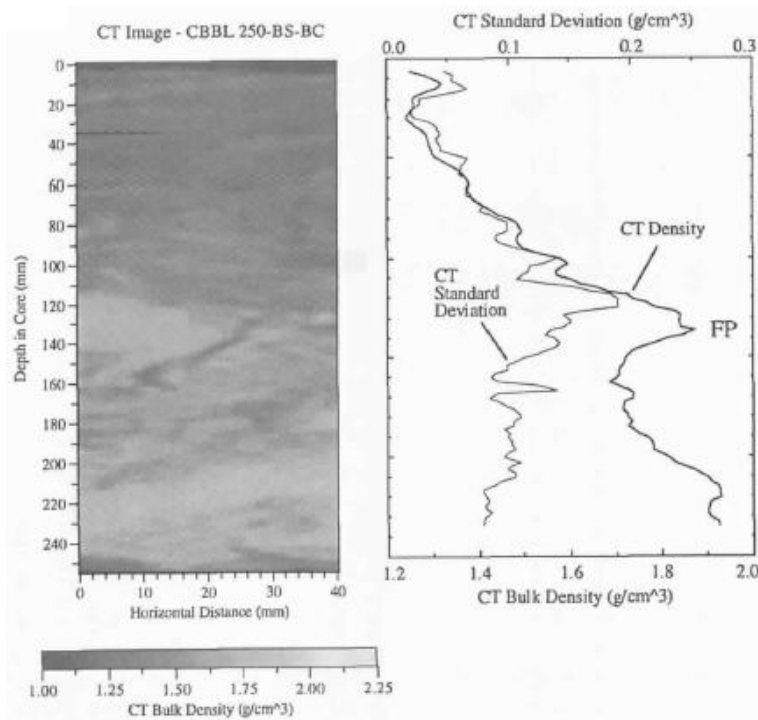
Figure 20. Reconstructed vertical CT sections and sediment depth profiles of CT bulk density and its standard deviation. Extract from Orsi (1994).

The CAT studies permitted a detailed investigation of the dynamics of the soil–plant–water system. Hence, it was possible to investigate the evolution in time of the spatial distribution of the water content in soil in the vicinity of a single plant root and to display it in a 3-D model (Aylmore, 1993; Hainsworth & Aylmore, 1983, 1986, 1989).

CAT also has been applied with good results in computing the hydraulic conductivity of porous materials as glass beads or soil aggregates. It has been proved that between the hydraulic conductivity and the spatial distribution of porosity, as determined by CAT, there is a positive correlation that allows the development of empirical relationships between these parameters (Phogat & Aylmore, 1996).

The quantification of soil structure by using different mathematical approaches as topological (Moreau et al., 1997) or fractal analysis (Zeng et al., 1996), starting from structure data obtained by CAT, represents another trend which has given interesting results. Thus, Moreau et al. (1997) have shown that only by using a 3-D reconstruction of soil porosity and fissure network, the percolation threshold can be correctly determined which implies a better quantitative evaluation of soil permeability. Zeng et al. (1996) have characterized the small-scale soil structure by means of two fractal parameters: fractal dimension and fractal lacunarity. In this way, by using the joint distribution of these parameters it was possible to better discriminate soils with similar, yet slightly different structures.

Accordingly, the use of CAT data acquisition in conjunction with modern mathematical data interpretation represents a promising procedure in soil science.

2.5.2 CAT IN SEDIMENTOLOGY

Sediments represent deposits of primarily rock and soil particles, transported from land areas to the lakes or seas by wind, ice, and rivers, as well as the remains of living organisms, chemical precipitates from water that accumulate on the lakes or sea beds.

Therefore, sediments present a great variety of internal structures as different types of laminae, worms tubes, plant roots, gas bubbles, mineral inclusions, etc. The same kind of

features excepting recent traces of living organisms can also be found in a large number of sedimentary rocks as sandstone or shales. All these characteristics are reflected in local changes of the sediment density as an important index of sediment strength.

CAT has been frequently used in sedimentology and particularly in petroleum geology. CAT investigation of sedimentary rocks has both a qualitative and a quantitative approach. Quanlitative investigations reveal various details of the core structure as bioturbation (Holler & Kögler, 1990; Cremer et al., 2002) (see Figure 22), presence of mollusk shells, (Duliu & Tufan, 1996; Muzi et al., 2004), heavy mineral inclusions (Verhelst et al., 1995), heterogenous discontinuities (Vinegar et al., 1991) as fissures (Queisser, 1988) or alternate beddings in compact sandstone (Swennen et al., 1991), biogenetic structures (Schaoping et al., 1994), partially filled fractures, vein selvage and vuggy porosity in limestone (Swennen et al., 1991), invasion of the mud induced by the capillarity of the small scale porosity (Bonner et al., 1995), facies succession composed of fine and thick rhythmites (Boespflug et al., 1995), rotational fractures in air dried oil shales (Coshell et al., 1994). By assembling together more sections, it was possible to obtain genuine 3-D representations of the investigated structures (Bonner et al., 1995; Duliu et al., 1997). Joschko et al. (1991, 1993), Muzi et al. (2004), and Capowiez et al. (2010) used CT for the three-dimensional reconstructions and visualization of the earthworm burrow system. The three-dimensional reconstruction revealed morphological features of the burrows which were not obvious from two-dimensional section images (see Figure 21). Since sedimentary structures reflect the environmental conditions during their accumulation, CAT has been used in description of facies as a result of transport processes and climatic variations (Long & Ross, 1991; Boespflug et al., 1995).
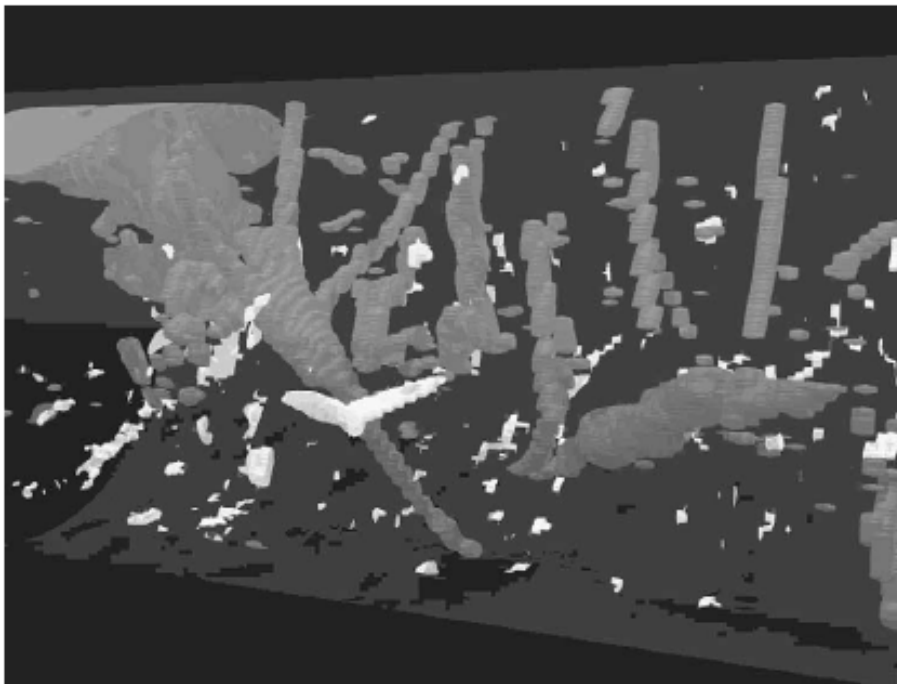
Figure 21. 3-D visualization of burrows and water pockets (gray) and shell pieces (white) in core. Extract from Muzi et al. (2004)
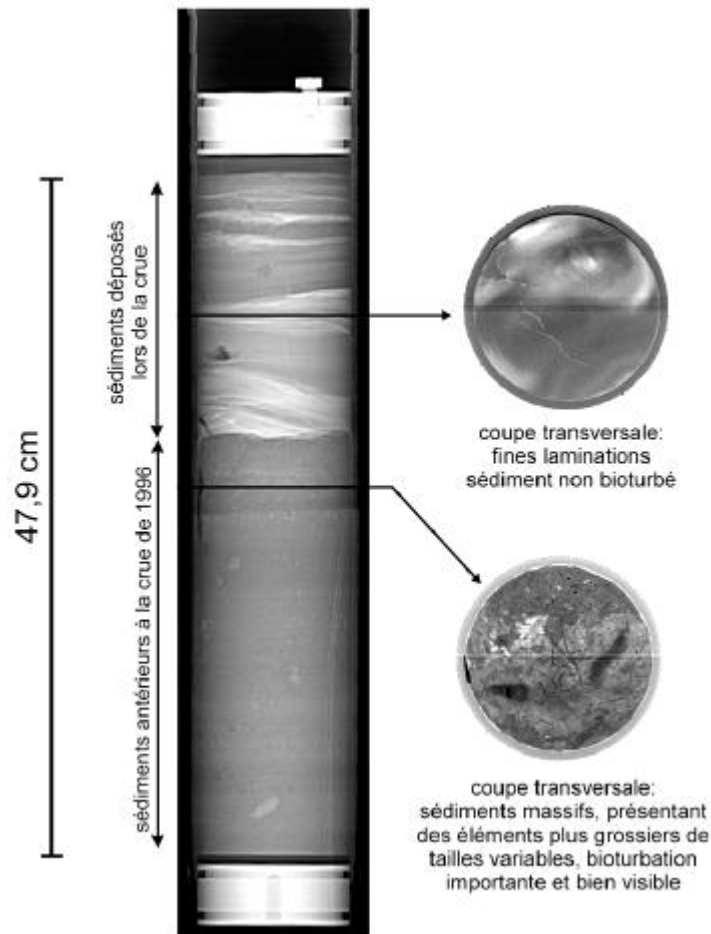
Figure 22. Topogram and CT slices. It is observed that the sediments deposited in 1996 are strongly bioturbated (burrows of benthic fauna). Extract from Cremer et al. (2002).

The quantitative approach is connected primarily with the sediment bulk density determinations as seen earlier.

The numeric data thus obtained (a CAT image represents, in fact, a set of CTN that can be processed by using any appropriate mathematics model) have been used in studies of oil displacement through porous rocks as a part of single or multiple-phase processes. Due to the great interest of rapid, non-destructive investigation of oil containing rocks, CAT has been utilized to examine the fluid flow in porous media with particular application to reservoir engineering and enhanced oil recovery. Therefore, CAT in view of its high ability in evidencing density differences less than 0.5%, has been utilized to measure the fraction of pore occupied by up to three distinct phases (oil, water and utilized to mea sure gas) (Vinegar & Wellington, 1987) as well as to investigate the relationship between residual saturation and porosity (Hicks et al., 1992). In a few experiments, the gamma-ray attenuation has have been used to study various three-component flows as gas–crude oil–tap water (Johansen et al., 1996) or air–water–sand (Torczynski et al., 1995). Laboratory CAT tests made it possible to compare experimental and numerical saturation profiles in the investigation of heavy oil displacement by water in a linear core (Fransham & Jelen, 1987), or to characterize the heterogeneites in porous media used in Enhanced Oil Recovery coreflood tests (Withjak et al., 1990; Peters & Afzall, 1992; Deterding et al., 1993; Robertson et al., 1994).

Another interesting approach consists in applying spectral analysis to investigate the periodicity of the annual rhythmites in correlation with bed thickness as they have been determined from longitudinal CAT densitometry of sedimentary cores (Boespflug et al., 1995).

The combined utilization of magnetic resonance imaging (MRI) and X-ray CAT has proved to be very useful in the investigation of water distribution in various rocks like limestone, granite or water saturated sandstone. Applied to the same core, the MRI and CAT showed to be two complementary methods. MRI can display with accuracy the presence of hydrogen-containing water but is insensitive to adjacent rocks while the CAT provides digital maps concerning local bulk density of the sample. In this way, MRI pictures only mobile hydrogen rich fluids and thus the distribution of porosity while the X-ray CAT displays rock matrices (Vinegar, 1986; Jeandey et al., 1991). The method of combining two complementary imaging techniques could be very useful in petrophysics and reservoir engineering or in any other study concerning the displacement of several different fluids in porous media.

2.5.3 CAT IN COAL GEOLOGY

Coal is the only organic rock which has been intensively investigated by CAT. Coal is composed of organic matter (maceral) and minerals. Mineral matter consists mainly of quartz with a small amount of pyrite and iron oxides, with a density which normally exceeds $2\,10^3\,kg\,m^{-3}$ and an effective atomic number between 11.8 and 23.6. The density of coal maceral (consisting of vitrinite, liptinite and inertinite) ranges between 1.2 to $1.7\,10^3\,kg\,m^{-3}$ while its atomic number is equal to 6. An entire network of cleats and pores are spread more or less uniformly over the entire rock. If empty, the density of cleats and pores can be considered equal to that of the air, if filled with liquid (usually water) their density becomes $1.0\,10^3\,kg\,m^{-3}$. Usually, coal has a banded structure, very heterogeneous in all directions. At the same time, the coal components present a regional distribution. These properties make coal very suitable material for CAT investigation.

To increase the performances of CAT investigation of coal, xenon (atomic number 54) (Maylotte et al., 1986) or Wood's metal has been used as a tracer and contrast agent (Pyrak-Nolte et al., 1997; Montemagno & Pyrak-Nolte, 1999) revealing with accuracy the fracture networks.

Quantitatively, as in the case of soil or sediments, CAT has been successfully used in the determination of coal densities during different processes as microbial desulphurization either cyclic oxidation (Kister et al., 1993).

More detailed information concerning coal composition has been obtained by combining 3D-CAT with and 2-D color image analysis of the same samples. CAT maps the coal density while color image analysis provides data about mineral content and maceral composition (Verhelst et al., 1996; Simons et al., 1997).

Van Geet & Swennen (2001), Mazumder et al. (2006), Yanbin Yao et al. (2009), Permana (2012) studied spatial disposition of pores, fractures and minerals of coal through 3D view that was built by specific softwares (see Figure 23 and Figure 24). Pyrak-Nolte et al. (1995; 1997) and Montemagno & Pyrak-Nolte (1999) used the Wood's metal as high-density contrast agent to extend the spatial resolution in revealing the volumetric geometry of fracture network in coal samples. The numerical values of the CTN corresponding to the entire samples have been use as raw data for further mathematical processing such as graph theory analysis or 3-D auto-correlation analysis to derive numerical data like correlation length of fracture network porosity, aperture distribution or fracture connectivity.

As in previous cases, the use of numerical CAT data in association with mathematical processing proved to be an elusive goal since the 3-D internal structure of rocks is very difficult to be investigated by conventional techniques.
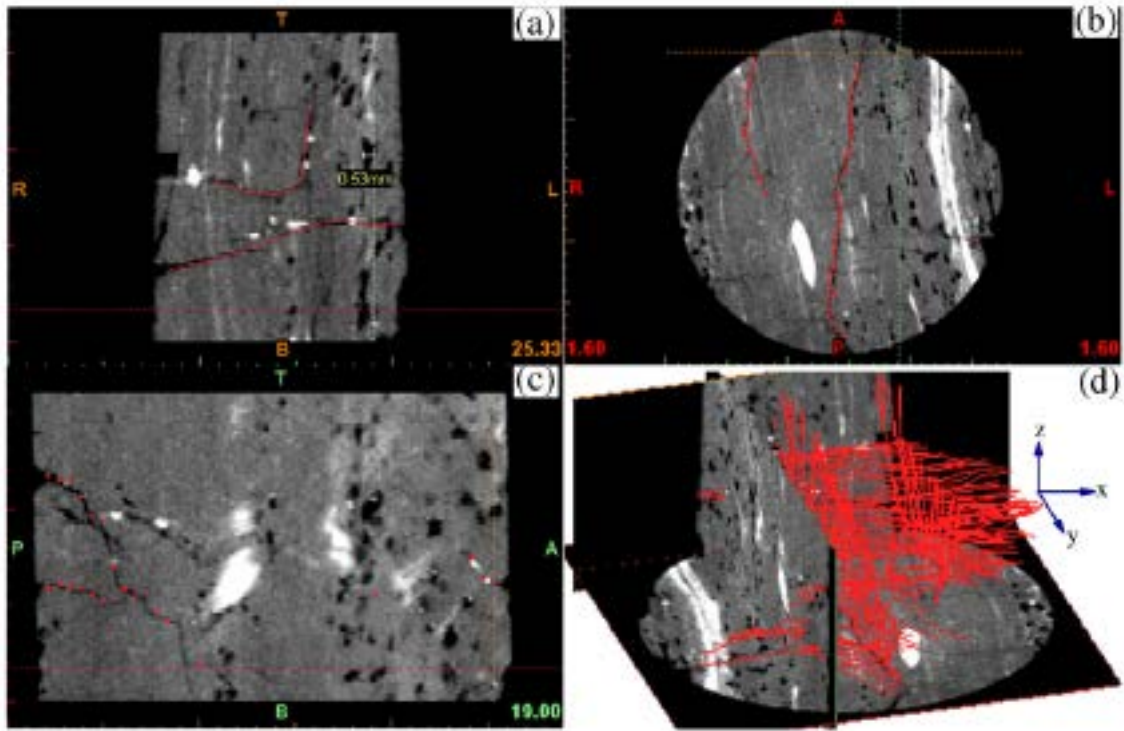
Figure 23. CAD 3D-view of pores (black spot), fractures (black line) and minerals (light white area) of a coal sample. 3D-view image shows the distribution of fractures (red lines). Extract from Yanbin Yao et al. (2009).
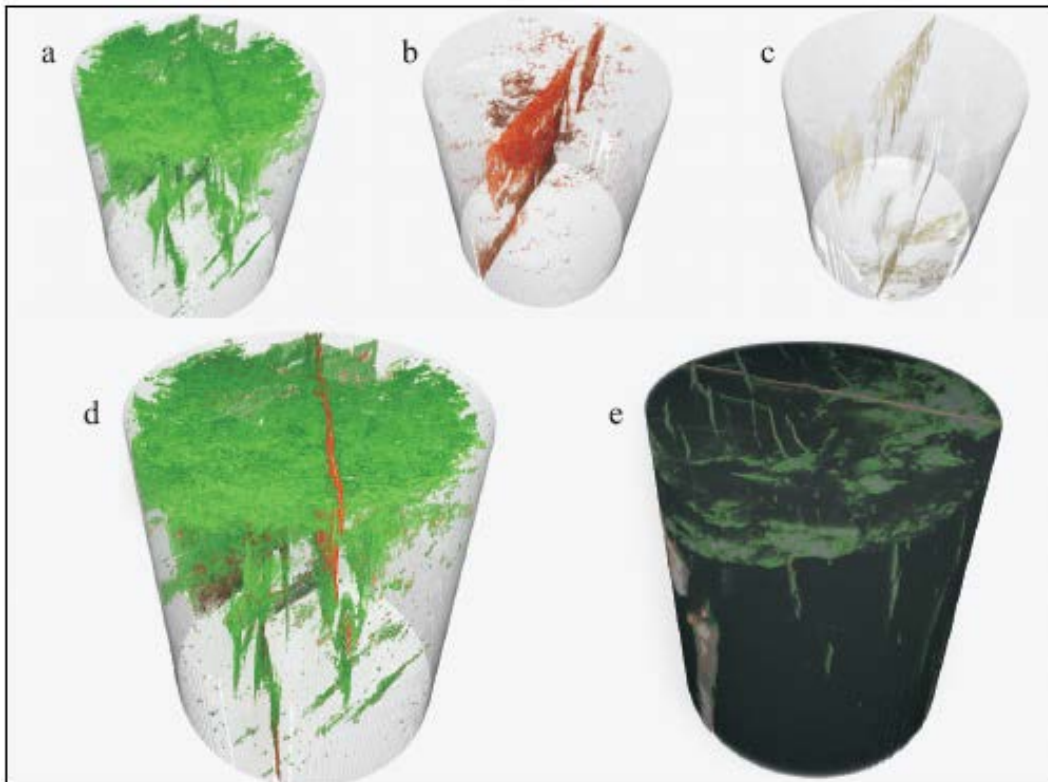
Figure 24. 3-D images showing the cleat development and mineralization from the X-ray CT analysis of the coal sample. (a) Low density minerals (kaolinite). (b) High density minerals (calcite). (c) Very high density minerals. (d) Integrated image from a, b and c, showing the pattern of cleat mineralization. (e) Complete 3-D image, showing the cleat pattern and mineralization in the coal sample. Extract from Permana (2012).

2.5.4   *CAT IN ROCK AND SOIL MECHANICS*

In geotechnical engineering, a correct determination of the degree of sample disturbance is very important. At the same time, there are an appreciable number of cases where the effects of local heterogeneities or discontinuities are of great importance. Such kind of defects can be encountered at different scales ranging from microns to a few meters and more. The local unhomogeneities often influence the mechanical properties and thus need a careful investigation. Hence, prior to any mathematical modeling of the rock behavior, an appropriate investigation of these defects could be very useful. The ability of CAT to reveal minor density fluctuations or defects having linear dimension comparable with the spatial resolution of the actual CT scanners makes this technique suitable for such kind of tests. In a more quantitative approach, these attributes are very useful to determine the mineralogical composition of different filling materials in inclusions or fractures. This numerical information can be used as input data for a mathematical modeling at a small scale of the materials being investigated. Generally, these data are collected prior, during and after the sample have been submitted to various tensile tests in order to monitor the changes therefore generated.

In one of the first paper related to this subject, CAT has been used to control the local changes induced in sandstone sample by a triaxial test (Raynauld et al., 1989). Quantitatively, as any variation of the local density is reflected in proportional changes of the attenuation coefficients, CAT allows precise determination of uniaxial compressibility. In order to avoid having to retrieve samples from the test cell to be scanned, a permeable to X-ray aluminum cell was constructed which allows the rock local deformations to be monitored during the test. From these data, Poisson's ratio and bulk compressibility were calculated (Vinegar et al., 1991). Therefore, CAT images permitted on the basis of the numerical values of gray shades to distinguish between veins filled with ferroan carbonates (HU~ 2500, density $3.5 \cdot 10^3$ kg/m^3) or with kaolinite (HU~1730, density $2.7 \cdot 10^3$ kg/m^3) in sandstone samples submitted to a direct shear test (Caers et al., 1997). These data have been further utilized to evaluate the results of mechanical tests on sandstone strength. Also it was possible to examine the generation of fault zones in a set of sandbox-model experiments (Colleta et al., 1991). In the same way Viggiani et al. (2004), Bésuelle et al. (2006) and Otani et al. (2010) monitoring with CT scan the triaxial tests over sedimentary soils/rocks (see Figure 25).
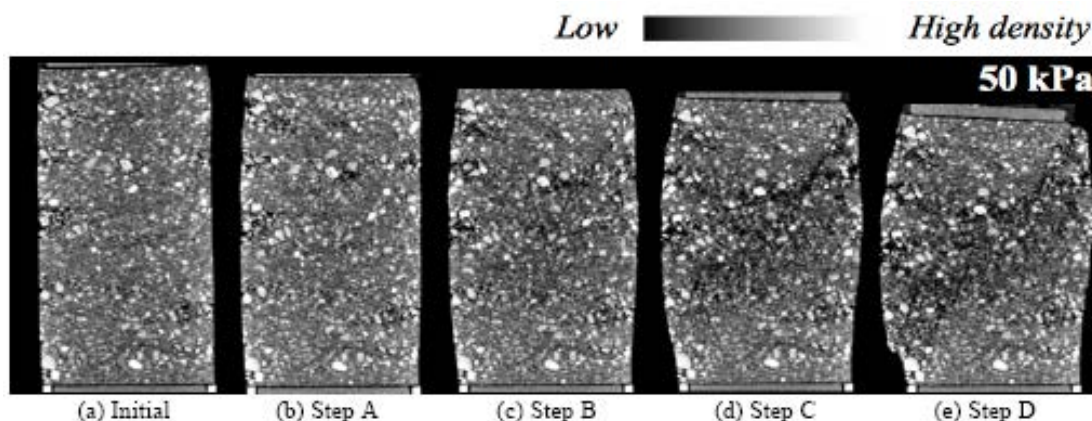
Figure 25. Vertical CT slices through the loading test. Extract from Otani et al. (2010)

Chapter III. CT SCANNER AND IMAGE POSTPROCESSING PROGRAMS

In this section, the type and the characteristics of CT scanner used for this study, the main imaging acquisition scanner parameters, image quality features and the programs used for post-processing are presented.

3.1 TYPE OF CT SCANNER AND IMAGING ACQUISITION SCANNER PARAMETERS

A medical X-ray CT scanner (Siemens Somatom Spirit® scanner, Figure 1 Chapter II) of the Hospital Veterinari Montjuïc (Barcelona, Spain), was used to acquire the CT images. It is a third generation Multislice CT scan.

A medical X-ray CT system such as used in this study was originally designed for use on human subjects to image soft tissue and bone. Cores used in this study consist mainly of sediments with densities of ~2 g/cm^3, which is similar to that of human bone. It might be reasonable to use medical X-ray for internal structures of wet sediments.

There are several imaging acquisition parameters that shall be known before use a CT scan and make a scan test. The concepts of these parameters are explained below.

3.1.1 SCAN PROTOCOLS

There are various protocols within medical CT scan. The scan protocols for adult and children are defined according to body regions – Head, Neck, Shoulder, Thorax, Abdomen, Pelvis, Spine, Upper Extremities, Lower Extremities, Specials, and Vascular.

The availability of scan protocols depends on the system configuration.

3.1.2 SCAN MODES

There are three scan modes in the Siemens Somatom Spirit® scanner. The modes describe how the table moves during an exam.

3.1.2.1 Sequential Scanning

This is an incremental, slice-by-slice imaging mode in which there is no table movement during data acquisition. A minimum interscan delay in between each acquisition is required to move the table to the next slice position.

3.1.2.2 Spiral Scanning

Spiral scanning is a continuous volume imaging mode. The data acquisition and table movements are performed simultaneously for the entire scan duration. The object on the table is moved continuously through the scan field in the z direction while the gantry performs multiple 360° rotations in the same direction. The X-ray thus traces a spiral around the object and produces a data volume. Figure 26 shows a scheme.
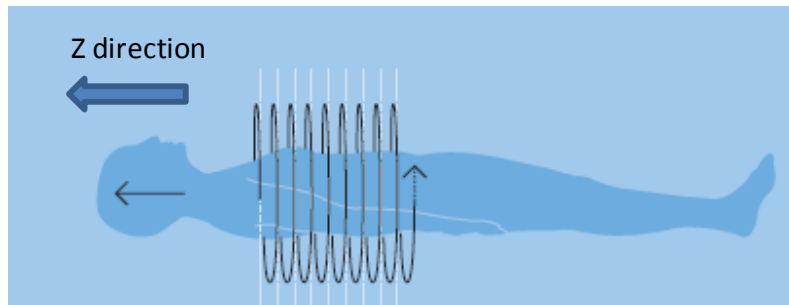
Figure 26. Scheme of the spiral scanning. Extracted from Siemens Medical Solutions (www.medical.siemens.com).

Each acquisition provides a complete volume data set, from which images with overlapping can be reconstructed at any arbitrary slice position. Unlike the sequence mode, spiral scanning does not require additional radiation to obtain overlapping slices.

3.1.2.3 Dynamic Serioscan

Multiple continuous rotations at the same table position are performed for data acquisition.

3.1.3 X-RAY TUBE VOLTAGE (KVP)

Is the electrical potencial (measured in kV or kVp) applied across the x-ray tube to accelerate electrons toward the target material.

3.1.4 TUBE CURRENT (MA)

Tube current is defined as the number of electrons accelerated across an x-ray tube per unit time, expressed in units of milliampere (mA).

3.1.5 ROTATION TIME

Rotation time is the time interval needed for a complete 360° rotation of the tube-detector system around the object. It affects the spiral scan length and thus the coverage of the scan range during a certain period of time.

3.1.6 RADIOGRAPHIC EXPOSURE (MAS)

The radiographic exposure (mAs) value is the product of the tube current and the rotation time.

3.1.7 SLICE COLLIMATION & SLICE WIDTH

Slice collimation is the slice thickness resulting from the effect of the tube-side collimator and the adaptive detector array design. In Multislice CT, the Z-coverage per rotation is given by the product of the number of active detector slices and the collimation (e.g., 2 x 1.0 mm).

Slice width is the FWHM (full width at half maximum) of the *sensitivity profile*, in the center of the scan field; its value can be selected by the operator according to the clinical requirement and generally lies in the range between 1mm and 10mm.

3.1.8 INCREMENT

The increment is the distance between the reconstructed images in the Z direction. If an appropriate increment is used, overlapping images can be reconstructed. In sequential CT, overlapping images are obtained only if the table feed between two sequences is smaller than the collimated slice thickness.

In spiral CT the increment is freely selectable as a reconstruction parameter, i.e. by selecting the increment the user can retrospectively and freely determine the degree of overlap without

increasing the dose. This technique is useful to reduce partial volume effect, giving better detail of the object and high quality 2D and 3D post-processing.

An illustrative example: A 100 mm range was acquired in the spiral mode with 10 mm collimation. After the acquisition, slices of 10 mm thickness can be reconstructed at any point of this range. If an increment of 10 mm is used, contiguous slices of 10 mm thickness are reconstructed every 10 mm. (see Figure 27.a).

If an increment of 5 mm is used, slices of 10 mm thickness are reconstructed every 5 mm (see Figure 27.b). The slices overlap by 50%. With an appropriate increment an overlap of 90% can be achieved.

(a)   *(b)*
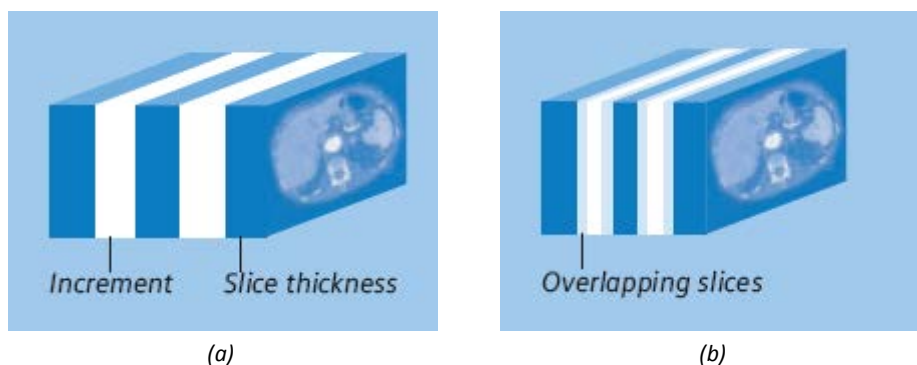
Figure 27. Illustrative examples of the choice of the increment. Extracted from SIEMENS Medical Solutions (www.medical.siemens.com).

3.1.9 PITCH

An important factor in spiral scanning is the table displacement per rotation. The larger the table displacement, the faster (i.e. with fewer rotations) an object region would be scanned. However, if the table feed is too large, image quality will be impaired. In this context the term "pitch" is used.

pitch = table feed per rotation/collimation

With the Siemens Multislice CT, we differentiate between:

Feed/Rotation: the table movement per rotation

Volume Pitch: table movement per rotation / single slice collimation.

Pitch Factor: table movement per rotation/ complete slice collimation.

E.g., slice collimation = 2 x 5 mm, table moves 10 mm per rotation, then Volume Pitch = 2, Pitch Factor = 1 (see Figure 28).
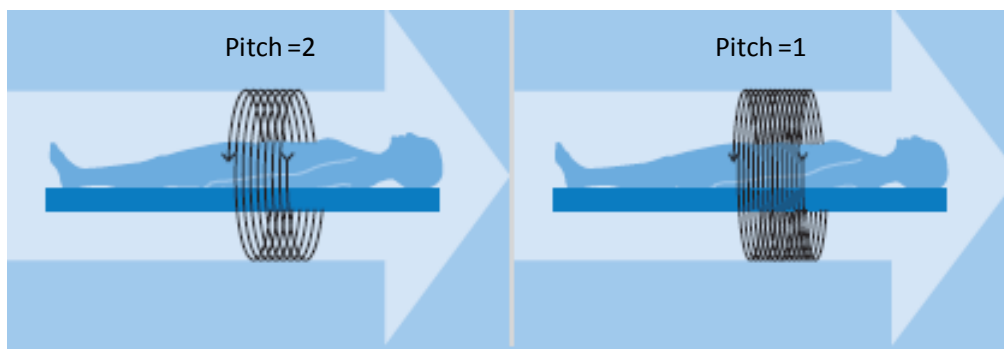
Figure 28. Examples of pitch models. Extract from SIEMENS Medical Solutions (www.medical.siemens.com).

With the Somatom Spirit, the pitch, slice, collimation, rotation time, and scan range can be adjusted. The pitch factor can be selected in between 0.5 and 2.

3.1.10 DISTANCE SOURCE TO PATIENT

It is defined as the distance between x-ray beam source and the patient/object; the square of Distance Source to Patient is inversely proportional to Exposure (Cordoliani et al., 2008, and Darlymple et al., 2005).

3.1.11 RESCALE INTERCEPT

Along with Rescale Slope, this parameter specifies the relationship between CT values measured in Hounsfield Units (HU) and the values encoded in pixel format (called "stored values"). The relationship is defined as:

$$CT values = m \cdot SV + b$$

<div align="right">Equation 7</div>

Where *m* is the Rescale Slope, *SV* is the stored values and *b* is the Rescale Intercept.

3.1.12 PIXEL SPACING

Pixel spacing is the physical distance between the centers of each two-dimensional pixel, specified by two numeric values. The first value is the row spacing in mm, that is the spacing between the centers of adjacent rows, or vertical spacing. The second value is the column spacing in mm, that is the spacing between the centers of adjacent columns, or horizontal spacing. These values are defined from reconstruction diameter.

To illustrate, consider the following example:
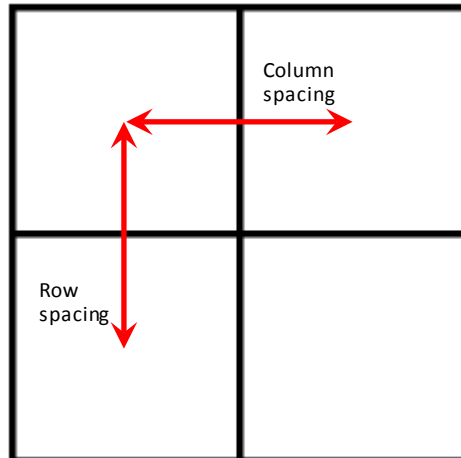
Figure 29. Illustrative example of pixel spacing.

3.1.13 RECONSTRUCTION MATRIX

Reconstruction matrix is the array of rows and columns of pixels in the reconstructed image, typically 512 x 512.

3.1.14 RECONSTRUCTION DIAMETER

Also known as Field of View (FOV), is defined as the diameter of the region used to reconstruct the image. This parameter is given by the product of Pixel Spacing and 512. Its value can be selected by the operator (which, in doing so, would indirectly establish the value of pixel spacing) and generally lies in the range between 12 and 50 cm. The choice of a small FOV

allows increased spatial resolution in the image, because the whole reconstruction matrix is used for a smaller region than is the case with a larger FOV; this results in reduction of the pixel size.

3.1.15 WINDOWING

In the CT image, density values are represented as gray scale values (the Scale of the CT Hounsfield Units is from -1024 to +3071). However, since the human eye can discern only approximately 80 gray scale values, not all possible density values can be displayed in discernible shades of gray. For this reason, the density range of diagnostic relevance is assigned the whole range of discernible gray values. This process is called windowing and is used to optimize contrast and brightness of images (see Figure 30).

To set the window, it is first defined to which CT number the central gray scale value is to be assigned to (window center). By setting the window width, it is then defined which CT numbers above and below the central gray value can still be discriminated by varying shades of gray, with black representing material of the lowest density and white representing material of the highest density.
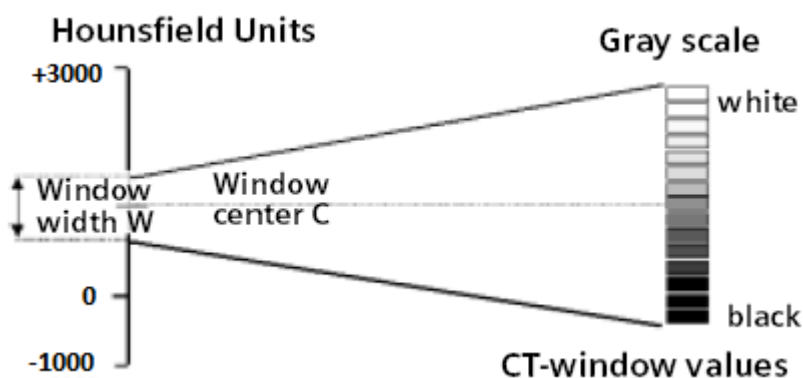
Figure 30. Windowing process scheme. Extract from SOMATOM Spirit Application Guide.

3.1.16 RECONSTRUCTION ALGORITHM

Reconstruction algorithms (filter or kernel) are defined as the mathematical procedure used for the convolution of the attenuation profiles and the consequent reconstruction of the CT image. The appearance and the characteristics of the CT image depend strongly on the algorithms selected.

3.1.16.1 Kernels

There are three different types of kernels: "H" stands for Head, "B" stands for Body, "C" stands for Child Head.

The image sharpness is defined by the numbers – the higher the number, the sharper the image; the lower the number, the smoother the image.

A set of 18 kernels is supplied, consisting of:

- 6 body kernels: smooth (B20s), medium smooth (B31s), medium (B41s), medium sharp (B50s), sharp (B60s), high resolution (B70s)

- 7 head kernels: smooth (H21s), medium smooth (H31s), medium (H41s), medium sharp (H50s), sharp (H60s), high res (H70s), ultra high res (H80s)

- 3 child head kernels: smooth (C20s), medium (C30s), sharp (C60s)

- 2 special kernels: S80s, U90s

3.1.16.2 Image Filters

There are three different filters available:

- **LCE:** The Low-contrast enhancement (LCE) filter enhances low-contrast detectability. It reduces the image noise.

- **HCE:** The High-contrast enhancement (HCE) filter enhances high-contrast detectability. It increases the image sharpness, similar to reconstruction with a sharper kernel.

- **ASA:** The Advanced Smoothing Algorithm (ASA) filter reduces noise in soft tissue, while edges with high contrast are preserved.

3.2 IMAGE QUALITY

CT images are the result of the interplay of physical phenomena giving rise to attenuation by the object of a thin fan beam of x-rays, and complex technical procedures. Each image consists of a matrix of pixels whose CT numbers (measured in Hounsfield Units, HU) represent attenuation values for the volume elements (voxels) within the slice. The quality of the image relates to the fidelity of the CT numbers and to the accurate reproduction of small differences in attenuation (low contrast resolution) and fine detail (spatial resolution). In the medical field, good imaging performance demands that image quality should be sufficient to meet the requirement for the examination, whilst maintaining the dose to the patient at the lowest level that is reasonably practicable. However dose limitations are not usually important in geosciences. However, dose and image noise are related.

Fundamentally, CT image quality is judged on four basic factors: image contrast, image noise, spatial resolution, and presence of artifacts (see Chapter II). Depending on the study, these factors interact to determine sensitivity (the ability to perceive low-contrast structures) and the visibility of details.

Image quality depends primarily on two types of scan parameter: dose-related parameters and those related to processing and viewing of the image. Both are hardware related. Dose-related parameters are the slice thickness, inter-slice distance, pitch factor, volume of investigation, exposure factors and gantry tilt. Processing parameters are field of view, number of measurements, reconstruction matrix size, reconstruction algorithm and window settings.

The purpose of this section is to describe the technical and physical parameters necessary for a good imagining technique. European guidelines on quality criteria for computed tomography (1999) has been consulted to carry out this purpose. In the present work clinical parameters are not important since it relates to field of geosciences.

3.2.1 PARAMETERS AFFECTING CT IMAGE QUALITY

Most of technical parameters with an influence on image quality and dose have been described in the previous section. Here we emphasize their influence on image quality.

3.2.1.1 Slice thickness

In general, the larger the slice thickness is, the greater the attenuation or low contrast resolution in the image; and the smaller the slice thickness is, the greater the spatial resolution. If the slice thickness is large, the images can be affected by artefacts, due to partial volume effects; if the slice thickness is small (e.g. 1-2mm), the images may be significantly affected by background noise.

3.2.1.2 Inter-slice distance/pitch factor

Inter-slice distance is defined as the increment minus slice thickness.

In general, for a constant volume of investigation, the smaller the inter-slice distance or pitch factor, the higher both the local dose and the integral dose to the object. Consequently, image noise diminishes.

3.2.1.3 Volume of investigation

Volume of investigation, or imaging volume, is the whole volume of the region under examination. In general the greater is its value the higher image noise.

3.2.1.4 Exposure factors

Exposure factors are defined as the settings of x-ray tube voltage (kVp), tube current (mA) and rotation time (s), and therefore radiographic exposure (mAs).

In general, increasing tube voltage (kVp) reduces image noise but can (slightly) reduce subject contrast as well.

Radiation dose is directly proportional to the tube current, whereas image noise is inversely proportional to the square root of the tube current; hence, lowering the tube current proportionally lowers the radiation dose, but increases image noise.

The selected radiographic exposure (mAs) and tube voltage (kVp) determine the dose. Higher mAs values reduce the image noise, thus improving the detectability of lower contrasts. This is illustrated in the water phantom images below where the image on the left was scanned with 80 mAs, while the image of the right was scanned with 40 mAs. The measured standard deviation of gray values is nearly 40% higher for the lower mAs scan.

(a)   (b)
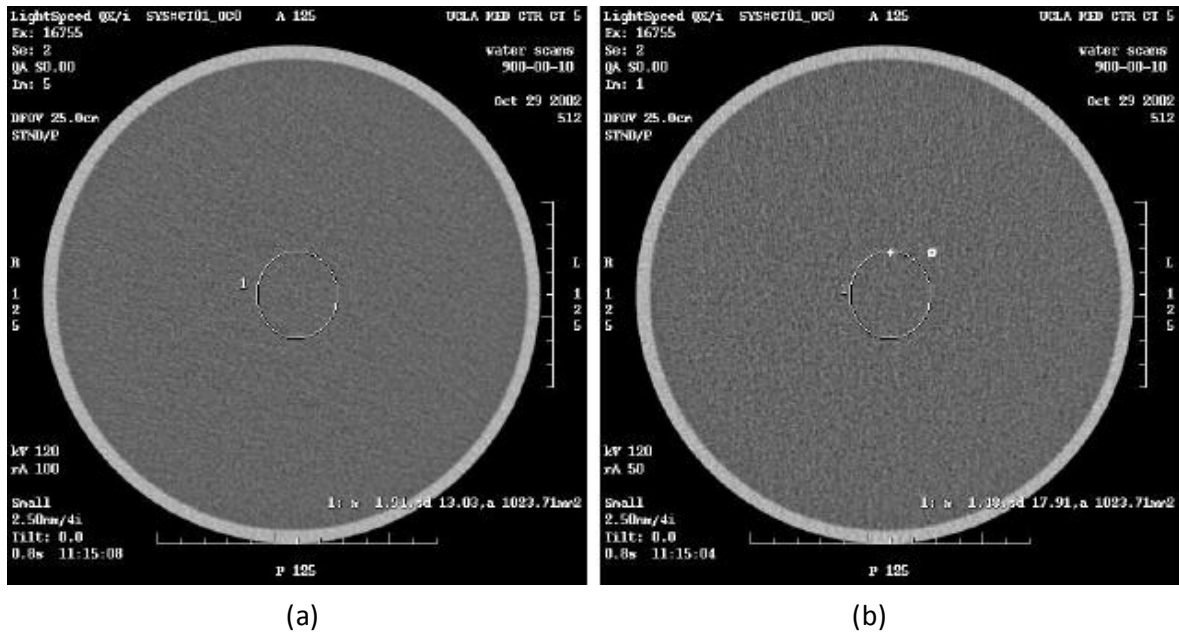
Figure 31. (a) water phantom scanned at 80 mAs; (b) same phantom scanned at 40 mAs and all other parameters identical. Extracted from McNitt-Gray (2006).

3.2.1.5   Reconstruction Diameter

The choice of a small reconstruction diameter allows increased spatial resolution in the image, because the whole reconstruction matrix is used for a smaller region than is the case with a larger field of view; this results in reduction of the pixel size. If raw data are available the field of view can be changed by post-processing.

3.2.1.6   Gantry tilt

Gantry tilt is defined as the angle between the vertical plane and the plane containing the x-ray tube, the x-ray beam and the detector array. Its value normally lies in the range between -25° and +25°. It may be used to reduce the radiation dose to sensitive organs or tissues and/or to reduce or eliminate artefacts.

3.2.1.7   Reconstruction algorithm

The appearance and the characteristics of the CT image depend strongly on the reconstruction algorithm selected. Depending on requirements, it may be necessary to select one or another filter and kernel which provides greater image quality.

3.2.1.8   Window width and window center.

The windowing process is used to optimize contrast and brightness of images. Narrower window widths adjusted to diagnostic requirements are necessary to display details with acceptable accuracy.

Window center should be selected by the viewer according to the attenuation characteristics of the structure under examination.

3.2.2   PARAMETERS DESCRIBING CT IMAGE QUALITY

The quality of a CT image may be expressed in terms of physical parameters such as uniformity, linearity, spatial resolution, low contrast resolution and absence of artefacts according to IEC recommendations (1994). Quality may be assessed by quantitative measurement of the parameters listed above, using suitable test phantoms, and by the appearance of artefacts.

3.2.2.1 Test Phantoms

Test phantoms are used for the purposes of *calibration* and evaluation of the performance of CT scanners. A number of test phantoms are commercially available and most manufacturers provide one or more test objects.

The test phantoms should allow for the following parameters to be checked: mean CT number, uniformity, noise, spatial resolution, slice thickness, dose and positioning of couch (IEC recommendations, 1994).

3.2.2.2 CT Number

The accuracy of CT number is verified by scanning a test object using the usual operating parameters and reconstruction algorithms. The CT number is affected by the x-ray tube voltage, beam filtration and object thickness. The CT number of water is by definition equal to 0 HU and the mean CT number measured over the central Region Of Interest (ROI) should be in the range +/- 4 HU.

3.2.2.3 Linearity

Linearity concerns the linear relationship between the calculated CT number and the linear attenuation coefficient of each element of the object. It is essential for the correct evaluation of a CT image. Deviations from linearity should not exceed +/- 5 HU over specific ranges.

3.2.2.4 Uniformity

Uniformity relates to the requirement for the CT number of each pixel in the image of a homogeneous object to be the same within narrow limits over various regions of the object such as a cylindrical 20 cm diameter phantom of water-equivalent plastic. The difference in the mean CT number between a peripheral and a central region of a homogeneous test object should be 8 HU. Such differences are largely due to the physical phenomenon of beam hardening.

3.2.2.5 Noise

Image noise is the local statistical fluctuation in the CT numbers of individual picture elements of a homogenous ROI. Noise is characterized by a grainy appearance of the image. The magnitude of the noise is indicated by the standard deviation of the CT numbers over a ROI in a homogeneous substance like water. It should be measured over an area of about 10% of the cross-sectional area of the test object.

When the phantom of water is used to evaluate the quality image, it is expected that every portion of that phantom would have a CT number zero. Due to the statistical fluctuation in every scan it is impossible for this to occur. CT system manufacturers have minimum and maximum values for allowable differences in CT numbers of a water phantom. Generally the range of $+3$ to -3 difference in CT numbers is negligible. Many of the spiral/helical scanners have a +4 to -4 allowable range because of the mathematical process of interpolation is included with the image reconstruction process.

The major sources of noise include quantum noise, electronic noise and computational noise. Quantum noise is a result of too few photons reaching a detector after being attenuated by the body. Any factor that limits the number of attenuated photons at the detector will increase image noise. Anatomical structure size, reduction of slice thickness without increasing technical factors, decreasing pixel size and scatter radiation are all factors that contribute to image noise. Electronic noise is noise contained within the image that can be caused by vibrations of any of the physical components of the scanner, especially the rotational components or power fluctuations. Computational noise is primarily caused by all the

statistical fluctuations that occur from the reconstruction algorithms that are essential to produce a CT image.

Image noise diminishes with the use of simultaneous reduction of spatial resolution and an increase in low contrast resolution. Image noise is inversely proportional to the square root of the dose and to the slice thickness. For example, if the dose is halved then the noise will only increase by about 40%. Conversely, a reduction in slice thickness requires a proportionate increase in dose in order to avoid an increase in noise.

3.2.2.6   Spatial Resolution

Spatial resolution at high and low contrasts is interdependent and critical to image quality.

The spatial resolution at high contrast (high contrast resolution) determines the minimum size of detail visualized in the plane of the slice. It is affected by the reconstruction algorithm, the detector width, the slice thickness, the object to detector distance, the x-ray tube focal spot size, the matrix size, the pixel size and the reconstruction diameter (field of view).

The spatial resolution at low contrast (low contrast resolution) determines the size of detail that can be visibly reproduced when there is only a small difference in density relative to the surrounding area. The size of the object that is visible depends on three factors: the level of contrast in the object, the image noise and the window setting used to display an image.

Common terms used when discussing low-contrast resolution are contrast scale, contrast-detail response, receiver operator characteristics (ROC), quantum noise, and dose.

- Contrast scale is affected by the window width and window level.

- Contrast-detail response (sometimes referred to as the contrast-detail curve) shows that for a given technique, the level of contrast that is visible will decrease as the object size decreases. To greatly simplify the concept, all other factors staying the same, smaller objects are harder to see than larger objects.

- ROC describes the fact that different observers will look at the same image and evaluate it differently. Therefore, the degree of contrast measured on an image is somewhat subjective.

- Quantum noise produces visible fluctuations in the image (i.e., a salt-and-pepper look). This factor will degrade images, particularly their low-contrast resolution. Since noise and radiation dose are linked; as radiation dose increases, image noise is suppressed. As the noise decreases, small low-contrast objects are more visible. Smoothing algorithms can help to reduce the visibility of noise by averaging each pixel with its neighbor.

3.3   IMAGING ACQUISITION PARAMETERS USED IN CAT TESTS

Table 1 shows the imaging acquisition parameters used during the reference CT scans tests. The choice of the acquisition parameters in reference CT scans was totally taken by the operator. He judged the results visually and qualitatively.

Table 1. Imaging acquisition parameters.

Imaging acquisition parameters	Reference CT scan tests											
	Sherbrooke				Shelby ($\phi_{int}\approx$83mm)		Shelby ($\phi_{int}\approx$67mm)		Österberg ($\phi_{int}\approx$95mm)		Österberg ($\phi_{int}\approx$76mm)	
	Set 1	Set 2	Set 3	Set 4	Set 1	Set 2	Set 1	Set 2	Set 1	Set 2	Set 1	Set 2
Scan Protocol	Pelvis	Pelvis	Pelvis	Pelvis	Hip	Hip	Hip	Hip	Hip	Hip	Hip	Hip
Scan Mode	Spiral	Spiral	Spiral	Spiral	Spiral	Spiral	Spiral	Spiral	Spiral	Spiral	Spiral	Spiral
X-ray tube voltage (kVp)	130	130	130	130	130	130	130	130	130	130	130	130
Tube current (mA)	178	178	178	178	63	63	63	63	63	63	63	63
Rotation time (s)	1000	1000	1000	1000	1000	1000	1000	1000	1000	1000	1000	1000
Radiographic Exposure (mAs)	122	122	122	122	31	31	31	31	32	32	32	32
Slice width	5	5	5	5	3	3	3	3	3	3	3	3
Increment	5	5	5	5		1.5	3	3	1.5	1.5	1.5	1.5
Pitch	1.2	1.2	1.2	1.2	1.2	1.2	1.2	1.2	1.2	1.2	1.2	1.2
Distance Source to patient	535	535	535	535	535	535	535	535	535	535	535	535
Rescale Intercept	-1024	-1024	-1024	-1024	-1024	-1024	-1024	-1024	-1024	-1024	-1024	-1024
Rescale Slope	1	1	1	1	1	1	1	1	1	1	1	1
Reconstruction Diameter	411	411	411	411	164	164	150	150	166	166	164	164
Pixel Spacing	0,802734/0,8 02734	0,802734/0,8 02734	0,802734/0,8 02734	0,802734/0,8 02734	0,320312/0,3 20312	0,320312/0,3 20312	0,292968/0,2 92968	0,292968/0,2 92968	0,324218/0,3 24218	0,324218/0,3 24218	0,320312/0,3 20312	0,320312/0,3 20312
Reconstruction matrix	512 x 512	512 x 512	512 x 512	512 x 512	512 x 512	512 x 512	512 x 512	512 x 512	512 x 512	512 x 512	512 x 512	512 x 512
Window center	300/40	400/35	400/700	450/40	300/40	400/35	300/40	400/35	300/40	400/35	300/40	400/35
Window width	1400/500	2000/280	2000/4000	1500/300	1400/500	2000/280	1400/500	2000/280	1400/500	2000/280	1400/500	2000/280
Kernel	B60s	B60s	B70s	U90s	B60s	B60s	B60s	B60s	B60s	B60s	B60s	B60s

3.4 POST-PROCESSING

Very many software allow image display of DICOM (Digital Imaging and Communication in Medicin) standard files, but only a few offer the possibility of analyzing them (measurements, histograms, etc.) and obtain rendering volumes, such as those of interest in this study.

Two programs are used in this study: ImageJ and GIMIAS software.

3.4.1 IMAGEJ SOFTWARE

ImageJ is a public domain Java image processing and analysis program inspired by NIH Image for the Macintosh. It can display, edit, analyze, process, save and print 8-bit, 16-bit and 32-bit images. It can read many image formats including TIFF, GIF, JPEG, BMP, DICOM, FITS and 'raw'. It supports 'stacks' (and hyperstacks) which are series of images that share a single window. It is multithreaded, so time-consuming operations such as image file reading can be performed in parallel with other operations.

It can calculate area and pixel value statistics of user-defined selections. It can measure distances and angles. It can create density histograms and line profile plots. It supports standard image processing functions such as contrast manipulation, sharpening, smoothing, edge detection and median filtering.

It does geometric transformations such as scaling, rotation and flips. Images can be zoomed up to 32:1 and down to 1:32. All analysis and processing functions are available at any magnification factor. The program supports any number of windows (images) simultaneously, limited only by available memory.

Spatial calibration is available to provide real world dimensional measurements in units such as millimeters. Density or gray scale calibration is also available.

ImageJ was designed with an open architecture that provides extensibility via Java plugins. Custom acquisition, analysis and processing plugins can be developed using ImageJ's built in editor and Java compiler. User-written plugins make it possible to solve almost any image processing or analysis problem.

3.4.2 GIMIAS SOFTWARE

GIMIAS is a trademark of Center for Computational Image and Simulation Technologies in Biomedicine (CISTIB), Universitat Pompeu Fabra (UPF), Barcelona, Spain.

GIMIAS (Graphical Interface for Medical Image Analysis and Simulation) is a software framework designed to be an integrative tool for fast prototyping of medical applications. It is a workflow oriented environment for advanced biomedical image computing and simulations, and it can be extended through the development of problem-specific plugins.

GIMIAS is particularly tailored to integrate tools from medical imaging, computational modeling, numerical methods and computer graphics in order to provide scientific developers and researchers with a framework for building a wide variety of tools. Multi-modal image processing, personalized model creation, numerical simulation and visualization of simulation results are some of the possible applications for which GIMIAS has been designed. The aim of this framework is to combine tools from different areas of knowledge providing a framework for multi-disciplinary research and medical study.

GIMIAS provides a graphical user interface with all main data IO, visualization and interaction functions for images, meshes and signals. It includes additional tools for image segmentation, mesh editing, signal navigation and specific visualizations.

Chapter IV. DESCRIPTION OF THE SAMPLING CAMPAIGN

4.1 OBJECTIVES

The main objective of the Soft Soil Project (Arroyo et al., 2012) was the evaluation of the soft soil sample quality depending on the type of sampler used. Three types of samplers were used: Sherbrooke, Shelby and hydraulic piston sampler (see Section 4.4), at three clayey levels (z=4.5m, 5.4m and 13.8m).

In order to not disturb soil samples, a rigorous methodology was carried out in both the field work (sampling, transport and storage) and the laboratory. Some examples are detailed below:

- The cutting of the steel tube samplers upright to prevent possible creep of the sediments (superficial samples).

- The cutting of the steel tube by a Dremel (multitasking tool with mini radial saw), in order to avoid overheating of the steel tube and therefore the drying of the soil sample.

- The development of an extraction system for tube samples (see Section 4.5).

- Triaxial and oedometer specimens retrieval in an enclosed and isolated space from the laboratory where relative humidity (95%) is controlled.

The evaluation of sample quality was carried out according to Lunne et al (1997). It is based on the determination of the relationship $\Delta e/e_0$. According to this methodology, there are four types of sample quality varying from excellent to very poor. Table 2 describes the sample quality categories as proposed by Lunne et al (1997).

Table 2. Sample quality categories (Lunne et al, 1997)

Sample quality	$\Delta e/e_0$
Very Good to excellent	< 0.04
Good to fair	0.04 – 0.07
Poor	0.07 – 0.14
Very poor	> 0.14

4.2 GEOLOGICAL SETTING

4.2.1 REGIONAL GEOLOGY

The test site is located in the vicinity of Castelló d'Empúries. Castelló de Empúries is located within the Quaternary deposits that form the coastal plain of l'Alt Empordà, which are placed between Paleozoic reliefs of Creus Cape to the north and the Mesozoic massif of Montgrí to

the south (see Figure 32). These materials are placed on Neogene materials of the tectonic depression l'Empordà, which emerge to the western part.
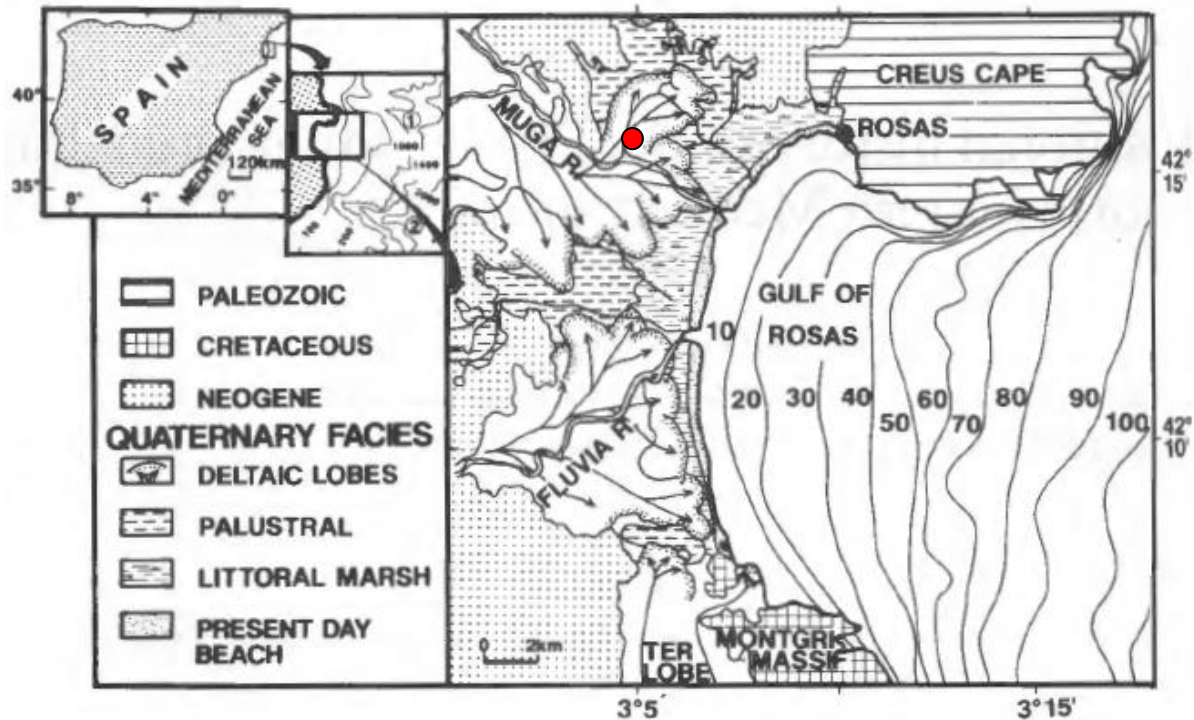
Figure 32. Test site location (red dot). Extract from Diaz & Ercilla (1993).

Morphologically it form a plain, embedded in foothill and Pleistocene alluvial-colluvial materials or in Pliocene and Plio-Quaternary materials, with a smooth relief, slopes below 0.2%, from levels of 10-15 m.a.s.l. (meters above sea level) inland to levels slightly higher or even lower than sea level.

Physiographic features along with structural behavior of the area conditioned facies distribution, result of the interaction between fluvial contributions and marine dynamics, in a sedimentary environments, partly recognizable although human action, that make up a delta plain.

Fluvial contributions that converge in this area comes mainly from La Muga and Fluvià rivers (north to south), and in the past Ter river too. This area is known as Corridor d'Albons. Thus, delta plain extended through this corridor to Ter delta plain (Baix Empordà), forming a continuous plain from the Creus Cape reliefs to Begur massif. Figure 33 shows a sketch of the delta plain evolution, where lobes (old) from the main water arteries (La Muga, Fluvià and Ter rivers) are individualized. In the coalescence areas of the lobes, bay zones are created, and with the formation of barrier islands would become lagoon areas (marsh ambient).

Figure 33. Sketch map of the recent Alt Empordà delta plain evolution. Extract from Bach & Plaza (1987).

According to Bach & Plaza (1987), stratigraphy consist of underlying Pliocene formations and two materials, called lower and upper unit as shown in Figure 34. The lower unit consists of coarse detritic beds (sands and gravels) interspersed between more powerful clay and silt beds. Bach & Plaza (1987) assume a pre-Holocene origin for these materials, formed in the first Versiliese transgression pulses, so that each cycle is a sea-level rise followed by periods of stillstand (or decreasing sea-level rise).

The upper unit is considered Holocene. Includes materials located above the alluvial gravels beds of the lower unit, that are very continuous throughout the area. The deposit power reaches about 50 m below the present coastline and about 25-30 m inland, where it connects with alluvial valleys materials.

Bach & Plaza (1987) divides upper unit on three levels:

1 - Lower level preferably sandy. It marks the beginning of the transgressive sequence. Sometimes, it is difficult to separate from alluvial gravels of the lower unit.

2 – Middle level with blackish clayey silts. It has a power about 25 m that decrease to inland, where interspersed with sand bodies, most abundant in Fluvià river contribution area. Samples obtained at this level present gastropods, foraminifers and ostracodes. This marine fauna, with little diversity of species observed, can be considered an indicator of protected or enclosed environments, with variable salinity calm waters and muddy bottoms, or areas close to river mouths. This level corresponds to the concept of fluvialmarine wedge described by Maldonado (1972) for Ebro Delta and by Marques (1975) for Llobregat Delta.

3 - Upper level groups sandy formations covered by clayey silts. Its power is about 20 m near the coastline, becoming thinner inland (see Figure 34). The basis of this level usually shows a coarser granulometry and presents shallow water fauna accumulations. The sands, that may form a continuous power about 20 m, shows granulometry from fine sand up to very fine sand, with shell fragments and dark tonalities. Sand level development is maximum at coalescence areas of river contribution, passing laterally to fluvialmarine sedimentation zones. This level is covered by silty sediments of marsh deposits or floodplain or marsh inland environments.
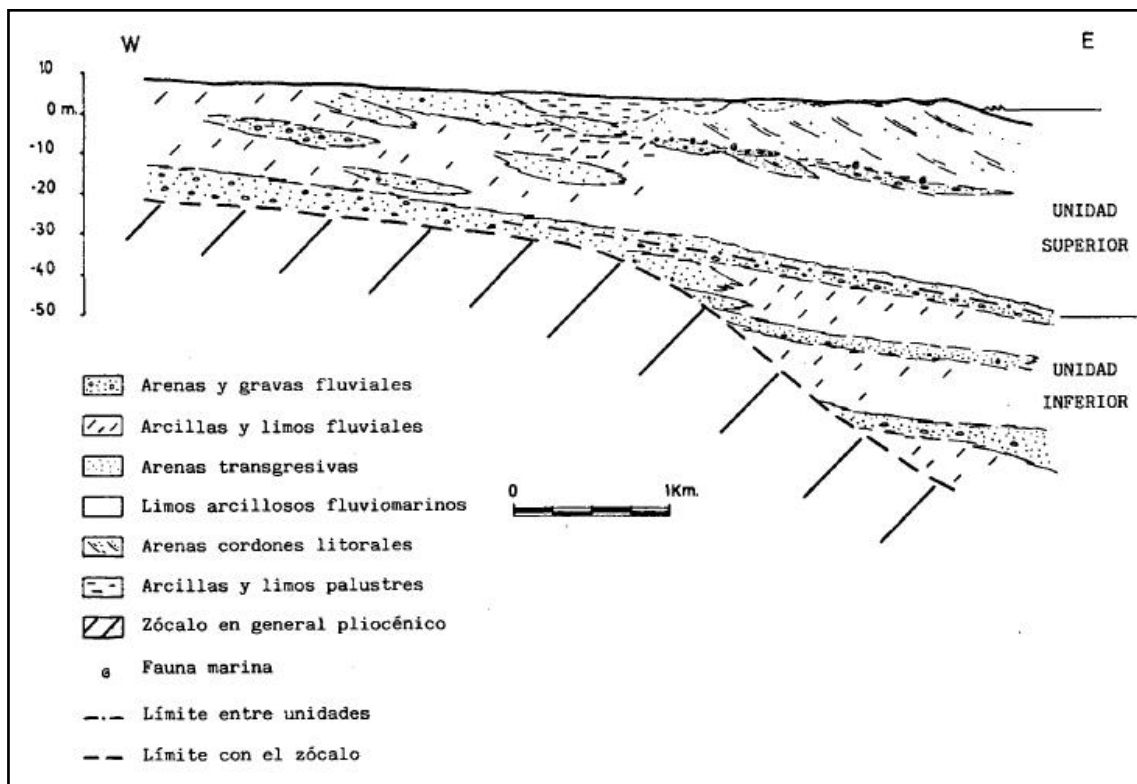
Figure 34. Interpretative sketch of the Holocene deposits. Extract from Bach & Plaza (1987).

4.2.2   STUDY ZONE

The study zone is in a parcel of industrial estate called el Pla, to the south of Castelló d'Empúries. The test site is flat and lies at about 10 m above the local datum, having a roughly rectangular shape of 30 by 50 m (see Figure 35). The water table oscillates significantly from 1.5 to 3.8m depth.

According to geological map (see Figure 36) the study zone is on Quaternary deposits of old deltas distributary channels of the floodplain (Qpas), formed by a sequence of sands and gravels. However, the stratigraphic column of boreholes carried out not corresponds to a sequence of sands and gravels, but predominantly the presence of silt and blackish clayey silts.

Considering Bach & Plaza (1987) stratigraphic classification, the materials of the study area looks like middle level of the upper unit, so they are considered proximal deposits of the fluvialmarine wedge of La Muga deltaic lobe.

Figure 35. Study zone location (Industrial estate of Castelló de Empúries)
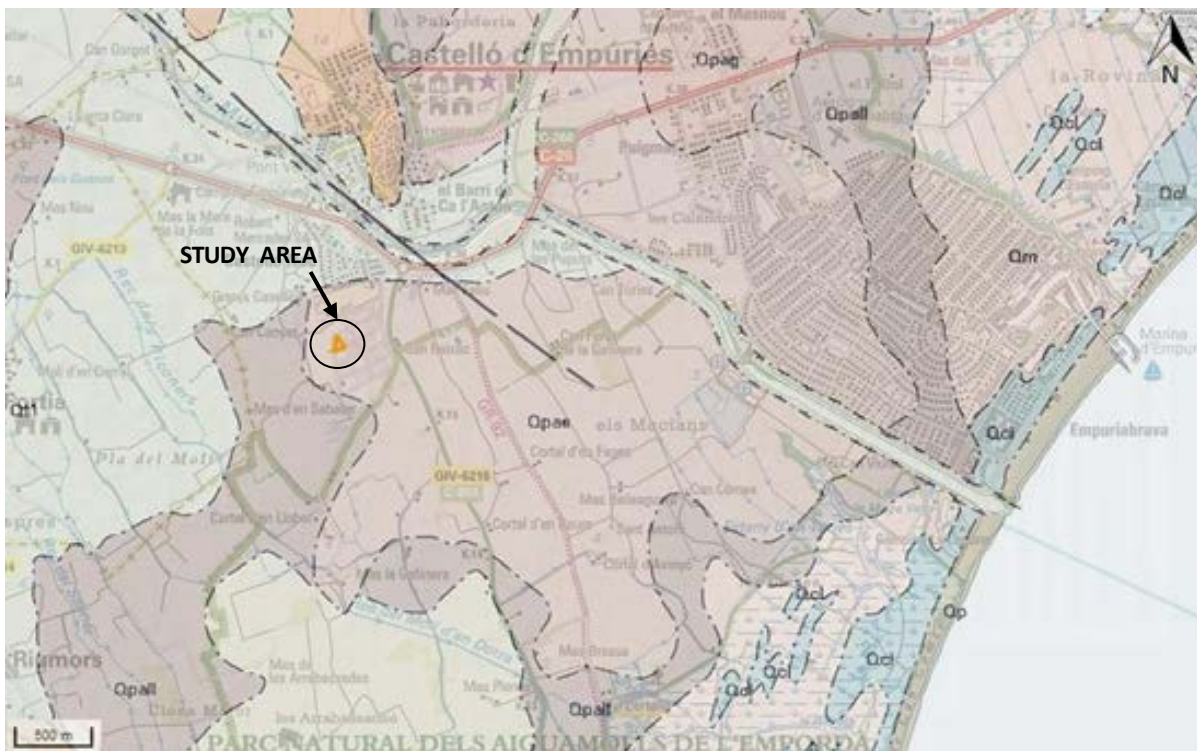
Figure 36. Geological – topographic map 1:50000. Extract from www.icc.cat.

4.3 GEOTECHNICAL PROFILE

The geotechnical exploration at the site included a large number of in situ tests, like CPTu, SDMT. This section summarizes the stratigraphic interpretation of CPTU (3 tests) and SDMT (2 tests). These tests were used to choose the soft soil levels to study (quality evaluation).

Figure 37 shows the tip cone resistance curves, uncorrected q_c are shown because pore pressure readings were lost due to transducter malfunctioning. Clay levels with qc $\leq$ 2500 kPa (from 2 to 6m depth and from 12.5 to 15m depth) and sandy levels are clearly identified. CPTU test also provide SBT (Soil Behaviour Type) profiles. Figure 38 shows SBT profiles.
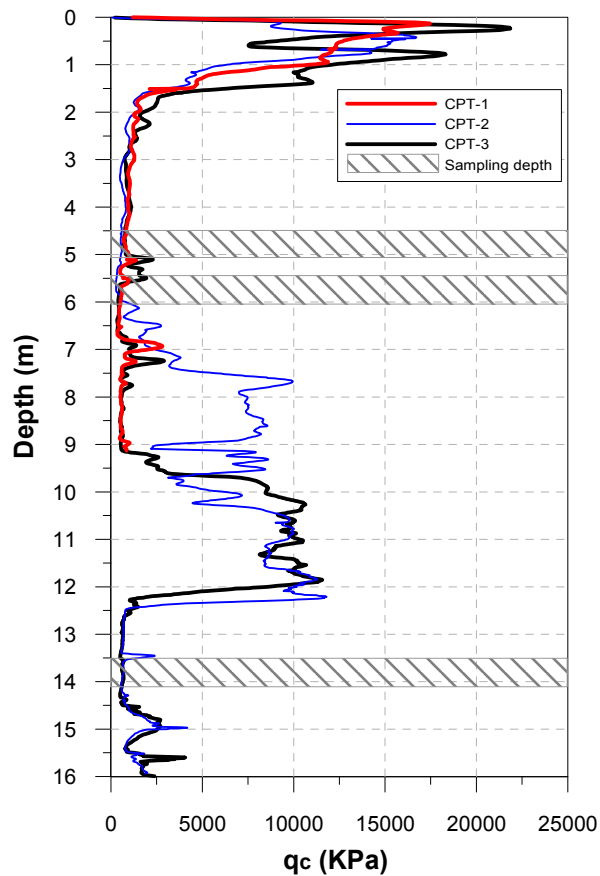
Figure 37. CPT qc profile.
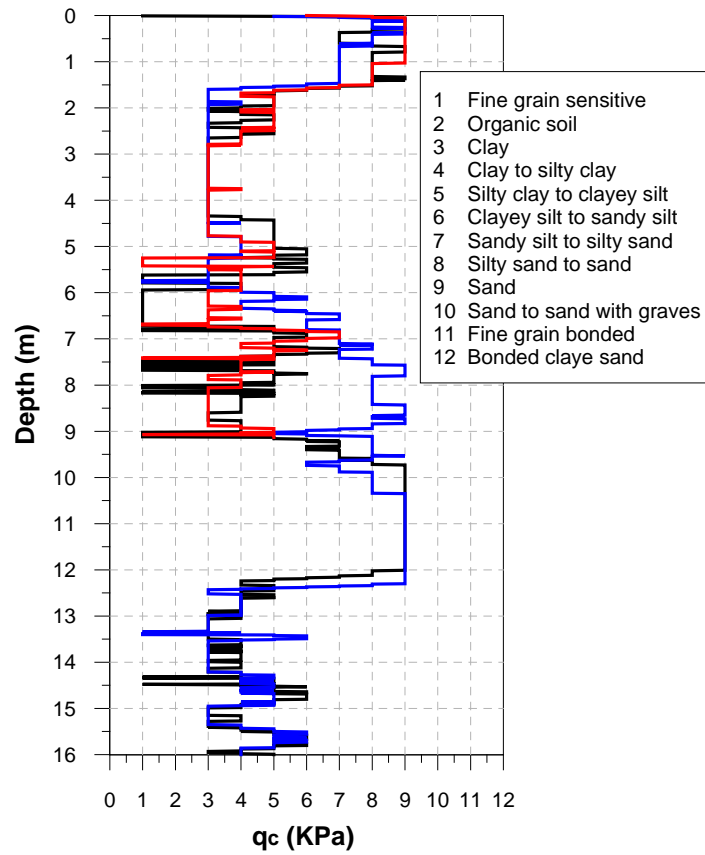
Figure 38. CPT SBT profile.

The I_D values deducted from SDMT tests also provide an indication of stratigraphic profile (see Figure 39).
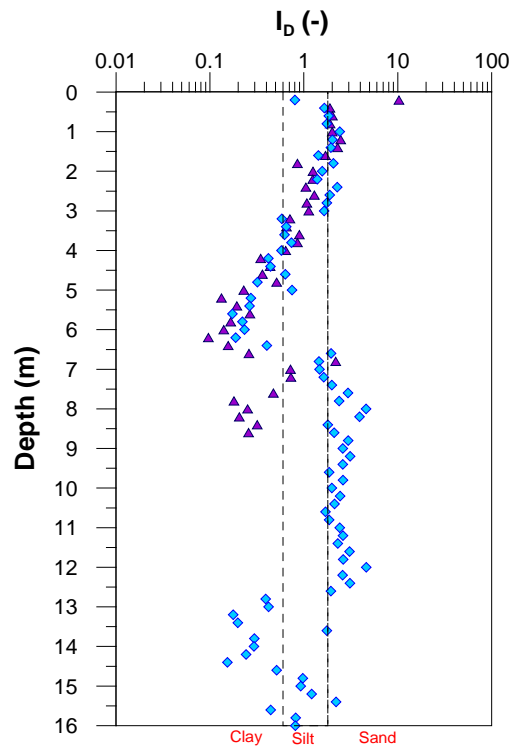
Figure 39. SDMT I_D profile.

4.4 SAMPLING CAMPAIGN

The sampling program was conducted jointly by Igeotest ® company and Department of the Geotechnical Engineering and Geosciences of Universitat Politècnica de Catalunya, UPC. The sampling campaign was divided into two phases, conducted on November 2010 and July 2011. In the first phase block samples were obtained using unconventional Sherbrooke sampler (Lefebvre & Poulin, 1979), developed for soft soil sampling. Norwegian Geotechnical Institute (NGI, Oslo) collaborated on Sherbrooke sampling campaign, because is the only one in Europe that have the required equipment. In the second phase, conducted on July 2011, was used two types of tube samplers (Shelby and hydraulic piston type, Österberg), normally used by Igeotest ® in conventional sampling campaigns.

4.4.1 BLOCK (SHERBROOKE) SAMPLING

The block sample extraction process was divided into three stages, following the guidelines suggested by Lefebvre & Poulin (1979) and the Norwegian Geotechnical Institute. These stages are: (i) a previous phase of drilling by a twist drill (ϕ = 500mm), (ii) the cutting and cleaning of the borehole bottom (corresponding to the top of the sample) using a cutting plane tool, and (iii) the cutting and extraction of the sample block.

Figure 40. Sampling procedure using Sherbrooke sampler.

In all cases, samples were coated with plastic wrap + aluminum foil + plastic wrap, and finally were placed into airtight containers which were filled with polystyrene to confine the block and prevent possible shocks during transport and storage in laboratory (see Figure 41).

Figure 41. Covering and protection of the block samples.

Six block samples ($\phi \approx$ 250mm, h $\approx$ 300mm) were obtained using sherbrooke sampler at interest layers / depths (see Table 3). Four of the six block samples were classified as "good", while the remaining two were classified as "regular". Figure 42 shows photographs of the block samples obtained.

Table 3. Block samples obtained with sherbrooke sampler.

ID Block	Depth (m)	Quality
Sherbrooke 1	-4.50 / -4.85	Good
Sherbrooke 2	-4.85 / -5.20	Regular
Sherbrooke 3	-5.37 / -5.70	Good
Sherbrooke 4	-13.05 / -13.40	Regular
Sherbrooke 5	-13.45 / -13.80	Good
Sherbrooke 6	-13.80 / -14.10	Good

Sherbrooke 1   Sherbrooke 2   Sherbrooke 3

Sherbrooke 4   Sherbrooke 5   Sherbrooke 6
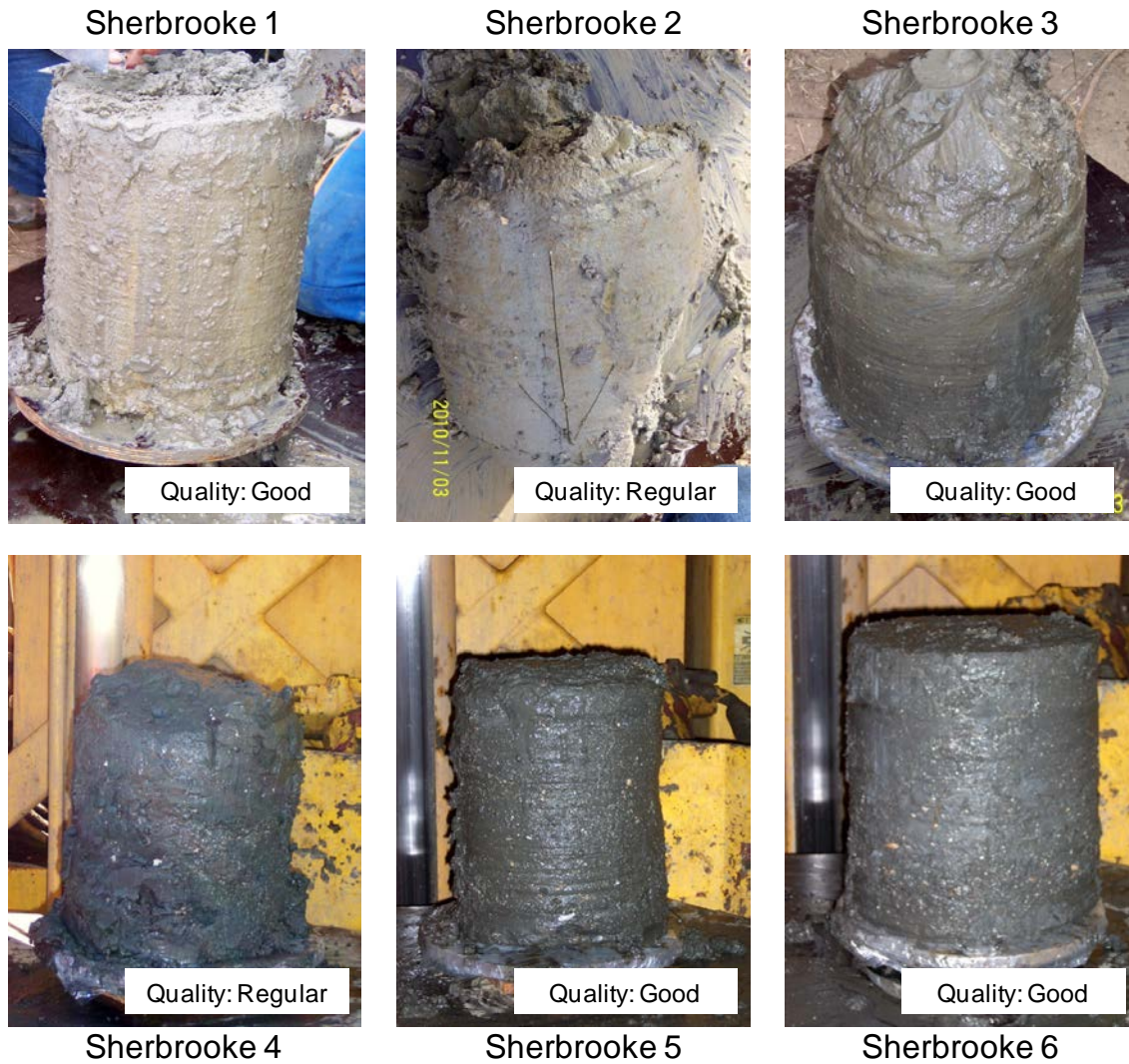
Figure 42. Block samples obtained with the sherbrooke sampler.

4.4.2 CORE SAMPLING

In the second phase, sampling was performed using tube samplers and it was conducted by Igeotest ® following the procedures normally used in field sampling. Two tube samplers were used: (i) Shelby tube and (ii) hydraulic piston sampler (Österberg, 1973) with two different diameters (but same length) as shown in Table 4. In all cases, both previous drilling to reach the sampling depth as the sampling process itself were performed by mechanical rotation.

Table 4. Type of tube sampler used.

ID Borehole	Sampler
B1	Shelby ($\phi_{int} \approx 83mm$)
B2	Shelby ($\phi_{int} \approx 76mm$)
B3	Österberg ($\phi_{int} \approx 95mm$)
B4	Österberg ($\phi_{int} \approx 76mm$)

The sampling procedure using tube sampler (Shelby and Österberg) was divided into 7 stages: (i) drilling up to the sampling depth using casing, (ii) assembly of the sampler, (iii) coupling the sampler with the drill rods, (iv) descent of the sampler up to the sampling depth, (v) insertion

of the sampler in the field, (vi) extraction of the sampler (with the soil sample) to surface, and (vii) disassembly of the sampler from the drilling equipment, previous sealing of the steel tube lower end, with a rubber stopper and duct tape. A summary of this process is presented in Figure 43.

The assembly of the hydraulic piston sampler was generally cumbersome because it has more parts than the open tube sampler (see Figure 44). The tube insertion process into the soil was monitored from the surface, by checking the fluid pressure into the interior chamber of the sampler until an abrupt increase was obtained. This was an indication that the interior tube had reached maximum travel length inside the field. The disassembly phase was also much more complicated than the open sampler, because it is necessary to disassemble the outer cylinder and uncouple the drill rods.
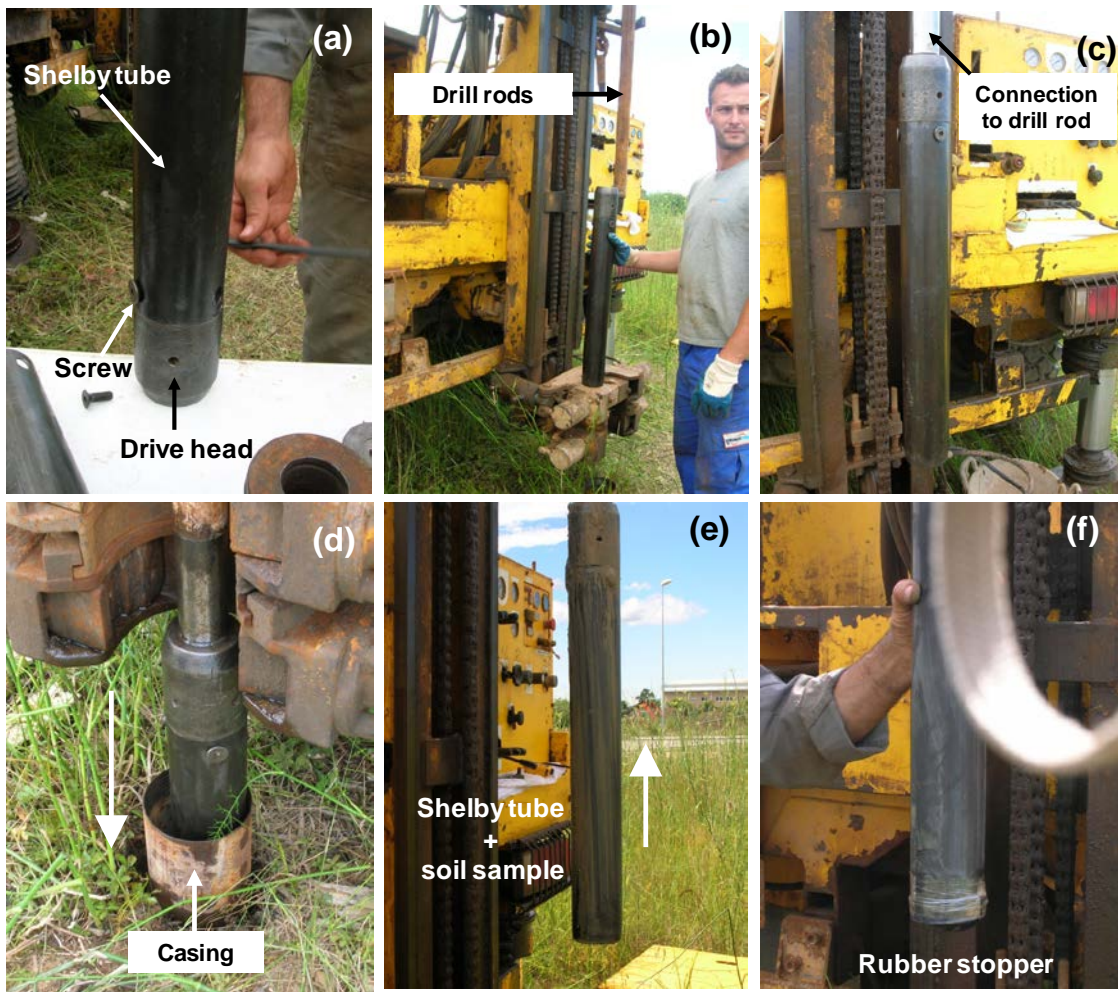
Figure 43. Sampling procedure using Shelby sampler.

Sampler head

Pressure cylinder

Fluid under pressure

Floating piston

Air vent

Thin wall tube
(Shelby)

Fixed piston

Soil sample

Cut shoe

Vacuum breaker duct
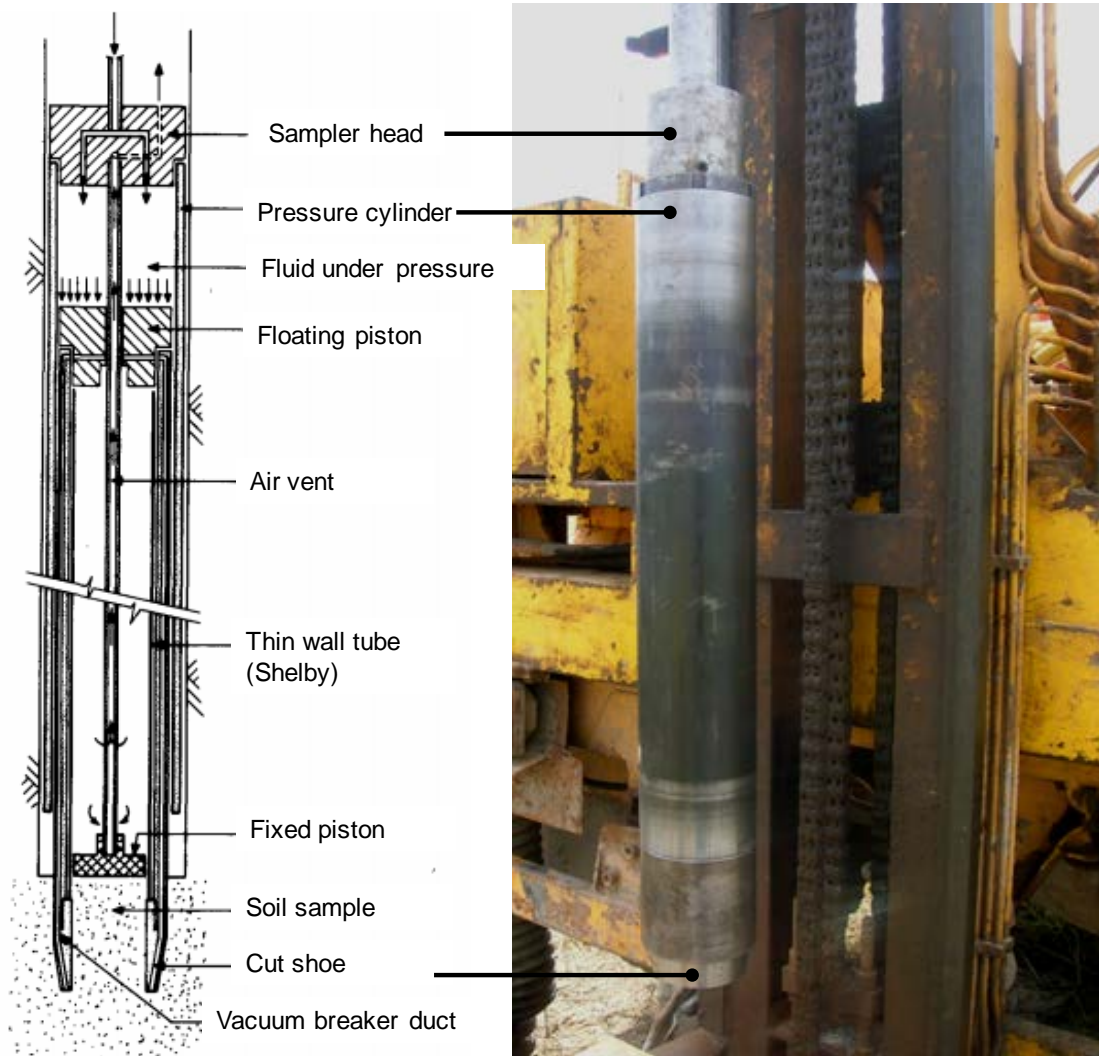
Figure 44. Österberg sampler.

Having been dismantled the sampler (previous sealing of the lower end), the tubes were placed on a steel support to carry out the sealing of the upper end (see Figure 45). For that, plastic wrap was placed inside the tube coating the top of the sample and then liquid paraffin was poured to produce a solid cap in order to prevent loss of moisture during storage and transportation (see Figure 45). Finally, the upper end of the tube was sealed with a rubber stopper and duct tape.

Figure 45. Sealing of sampling tubes.

Ten samples were obtained from four different boreholes. One kind of sampler was used in each borehole as shown in Table 4. Shelby sampler was used in boreholes B1 and B2, while hydraulic piston sampler was used in boreholes B3 and B4.

The initial objective was to obtain three tube samples (for borehole) at three depths on which sherbrooke samples were obtained: (1) between -4.5/-5.1m, (2) between -5.5/-6.1m, and (3) between -13.5/-14.1m. However, due to problems during sampling process and sampler extraction, it was impossible to obtain the three samples in each borehole. Table 5 presents the retrieved tube samplers and the recovered sample length.

Table 5. Recovered sample length of tube samplers.

ID Borehole	Depth (m)	Sampler type	Sample length (mm)
B1	-4.5/-5.1	Shelby (ϕint ≈83mm)	560
	-5.5/-6.1		585
	-13.5/-14.1		340
B2	-4.5/-5.1	Shelby (ϕint ≈76mm)	527
	-13.5/-14.1		563
B3	-4.5/-5.1	Österberg (ϕint ≈95mm)	153
	-13.5/-14.1		521
B4	-4.5/-5.1	Österberg (ϕint ≈76mm)	511
	-5.5/-6.1		223
	-13.5/-14.1		521

ESTING PROGRAM

4.5   TESTING PROGRAM

This section summarizes the number of specimens, their location in samples, and the retrieval methods (block and tube cases).

4.5.1   BLOCK SPECIMEN RETRIEVAL

In order to locate each test specimen, block was divided into sectors according to an established reference. Block was referenced with directions North (N), East (E), South (S) and West (W) as shown in Figure 46 (upper). Additionally, four sectors were established (A, B, C and OED). The pieces A, B and C are for triaxial specimens of 38x76mm and the pieces OED for oedometer specimens of 50x20mm (diameter x high).

Taking into account the high ratio between the total height of the block (H ≈ 310mm) and the height of triaxial specimens (h = 76mm), the block was divided into two pieces (upper and lower) to double the amount specimens to be obtained (see Figure 46 (bottom)). The height of each piece was approximately 120mm. Two oedometer specimens were obtained for each piece (4 specimens in total), with a minimum distance of 25mm between specimens to avoid including altered material produced during the retrieval.

In summary, the specimens obtained were:

- o 6 triaxial specimens of 38x76mm (3 in the upper piece and 3 in the lower piece) in the pieces A, B and C.

- o 4 oedometer specimens of 50x20mm (2 for piece) in the piece OED.
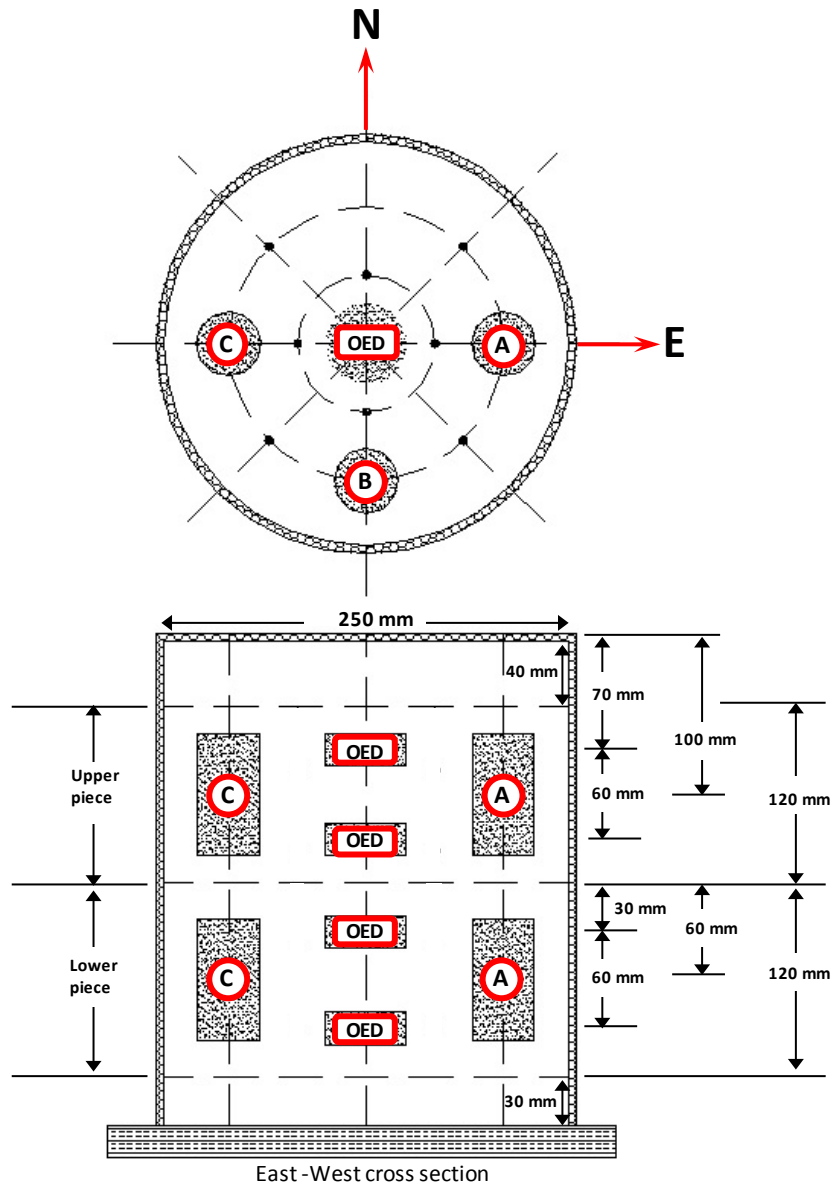
Figure 46. Triaxial and oedometer specimen distribution in block sample.

4.5.2 TUBE SPECIMEN RETRIEVAL

Sample retrieval from tube sampler was divided into three phases: (i) cutting of the tube, (ii) extraction of the soil sample and (iii) retrieval of the triaxial and oedometer specimens. For phases (i) and (ii) an ad-hoc methodology was followed because it is focused to induce the minimum alteration to the soil. The tube cutting was performed using a mini-disc cutter (Dremel ®) (10000r.pm) as shown in Figure 47. With this equipment was avoided the heating of the steel tube. The cutting process was performed by placing the tube upright on a press in order to block its movement during Dremel use. Afterwards, the tube was cutted into lengths of approximately 120 mm for triaxial and oedometer specimens retrieval (see Figure 48).

Figure 47. Tube cutting.

The most delicate stage of the process was the removal of the soil sample from the steel tube. In order to do this, a simple extraction system using thrust piston and reaction frame was developed. The procedure consisted to gently push the soil sample with a solid piston aid which was being introduced into the steel tube as the sample was expelled from the top. For that, two rings were placed on top and bottom, fitted with the tube wall (see Figure 48). The bottom ring was the guide for the thrust piston while the upper ring was the support of a hollow steel cylinder (with larger diameter than the sampler tube) used to laterally restrain of the soil sample during extraction. Figure 49 shows the extraction process and the final state of the sample. As shown in Figure 49, the quality of the samples from this procedure was good in all cases.

Figure 50 shows triaxial and oedometer specimens location in the tube sampler topograms.
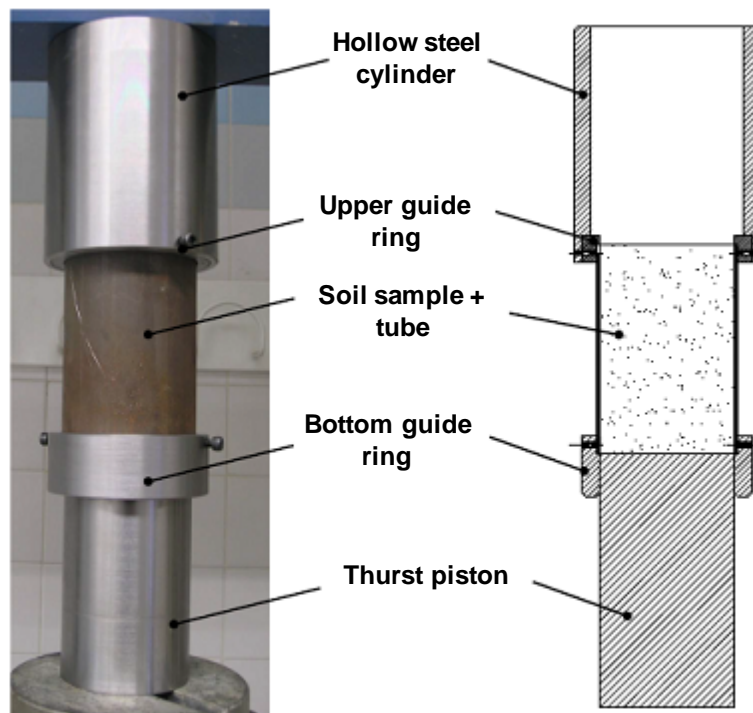
Figure 48. Extraction system for tube samples.

Figure 49. Extraction process of tube samples.

Shelby φ=88 mm   Shelby φ =80 mm   Österberg φ =100 mm   Österberg φ =80 mm
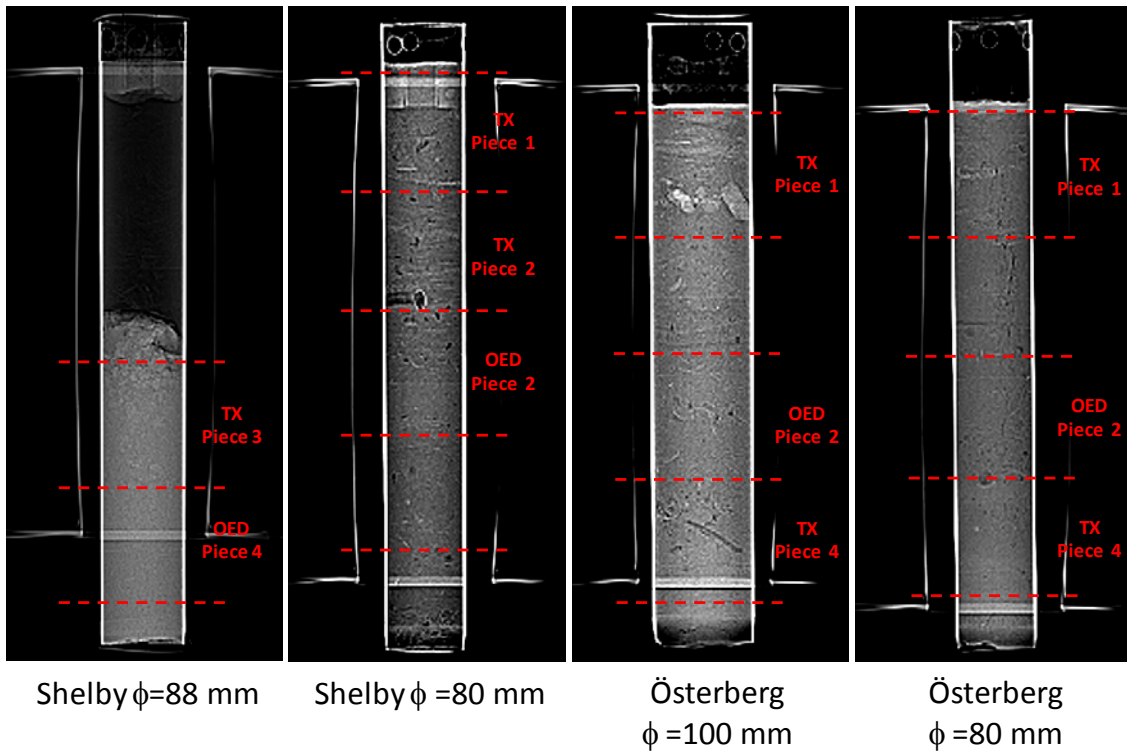
Figure 50. Triaxial and oedometer specimens location on in tube sampler topograms (CT).

4.5.3 *TRIAXIAL AND OEDOMETER SPECIMENS*

Taking into account that the present study only examines the clayey silt level at 13.8m depth, a total of 11 oedometer and 10 triaxial specimens are studied. The following table summarizes the sampler source, location (depth), reference and type of each specimen.

Table 6. Reference for each test specimen.

ID sampler	Depth (m)	Type of specimen	ID specimen
Sherbrooke 6	13.86	Oedometer	OED1-SHK6-L
			OED 2-SHK6-L
	14.01		OED 3-SHK6-L
	14.01	Triaxial	TX1-MA-SHK6-L
	13.86		TX2-MB-SHK6-L
			TX3-MC-SHK6-L
Shelby φ=88mm	14.15	Oedometer	OED 1-SHB88-L
			OED 2-SHB88-L
	14.00	Triaxial	TX1-SHB88-L
Shelby φ=80mm	13.80	Oedometer	OED 1-SHB80-L
			OED 2-SHB80-L
			OED 3-SHB80-L
	13.50	Triaxial	TX1-SHB80-L
	13.65		TX2-SHB80-L
Österberg φ=100mm	13.80	Oedometer	OED 1-ÖST100-L
			OED 2-ÖST100-L
			OED 3-ÖST100-L
	13.50	Triaxial	TX1-ÖST100-L
	13.95		TX2-ÖST100-L
Österberg φ=80mm	13.80	Oedometer	OED 1-ÖST80-L
			OED 2-ÖST80-L
			OED 3-ÖST80-L
	13.95	Triaxial	TX1-ÖST80-L
	13.50		TX2-ÖST80-L

Chapter V. LAB TEST RESULTS

5.1 CHARACTERIZATION

This section summarizes the results from basic characterization tests. These include analysis of grain size distribution (UNE 103101-1995), determination of consistency index (UNE 103103-1994 and 103104-1993), determination of specific weight of solid particles (UNE 103302-1994) and determination of carbonates content (UNE 103200-1993) carried out on three block samples (Sherbrooke) and samples collected during execution of borehole 2.

Figure 51 shows grain size distribution profile from samples taken on borehole 2. Fine grained levels dominate at 2-6m and again at 12.5-14m.
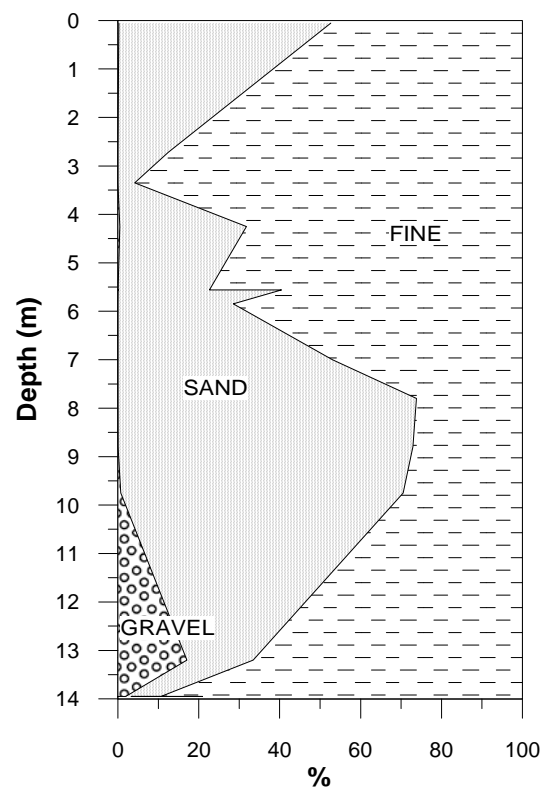
Figure 51. Grain size distribution profile.

This work focuses on the study of samples taken at 13.8m depth on boreholes perforated in close vicinity (5 m radius) from borehole 2. These samples were intended to be representative of the bottom dominated clay layer. Lateral variability at the site has not been assessed in detail, but due to the deposit characteristics it is likely to be large. For instance, the soil sample of the large Shelby (ϕ_{int}=93mm) was extracted also at 13.8m depth, but this soil is clearly different, more granular in nature, and more akin to the material that in borehole 2 lies just above the target level. Figure 52 shows the grain size distribution of samples at 13.8m depth and the sample extracted with Shelby (ϕ_{int}=93mm).
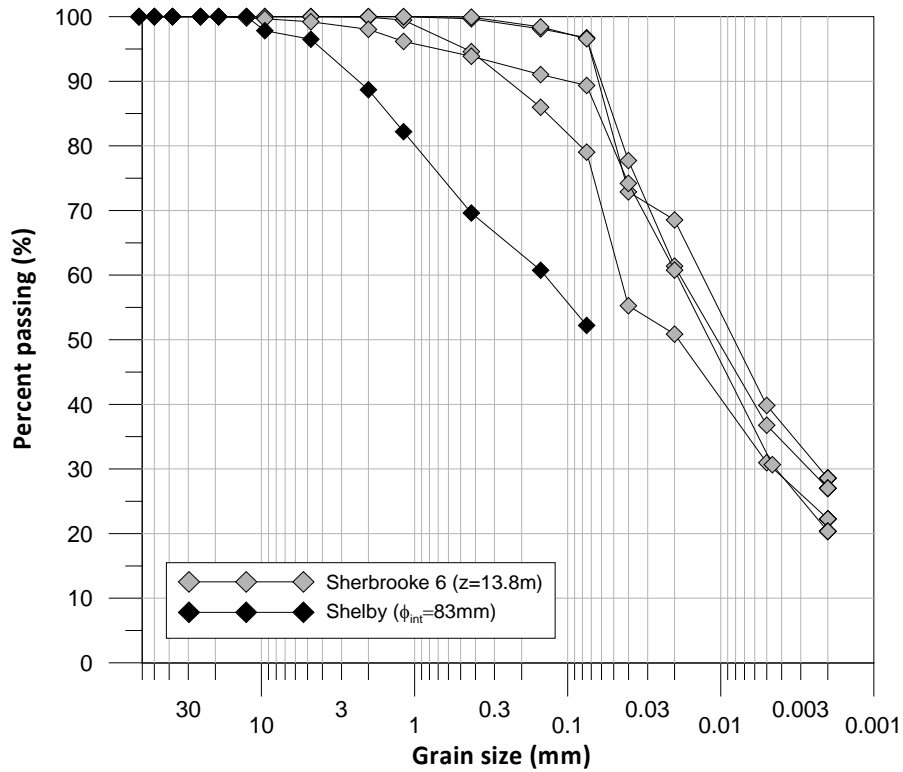
Figure 52. Grain size distribution of Sherbrooke samples and Shelby (ϕint=83mm), 13.8m depth.

Figure 53 shows the Casagrande Plasticity Chart of the fine fraction, where results of samples from 13.8m depth are presented. The most of the samples are classified as CL (USCS).
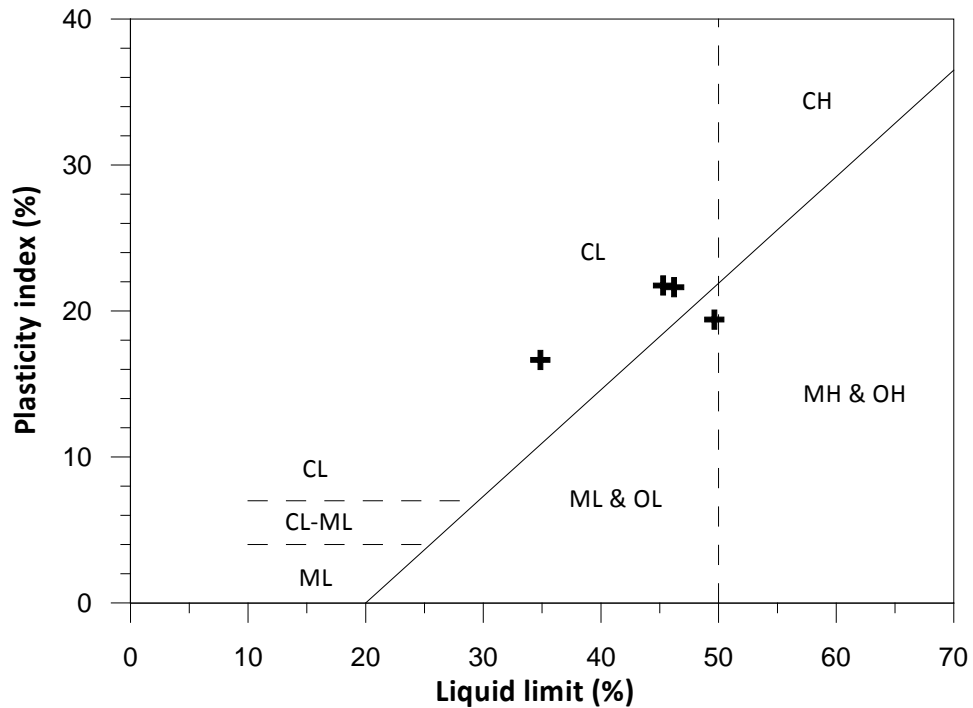
Figure 53. Casagrande Plasticity Chart.

Figure 54 and Figure 55 show the profiles of the values obtained from analysis of specific weight of the solid particles (pycnometer method) and carbonate content (Bernard calcimeter). The level of interest is marked.
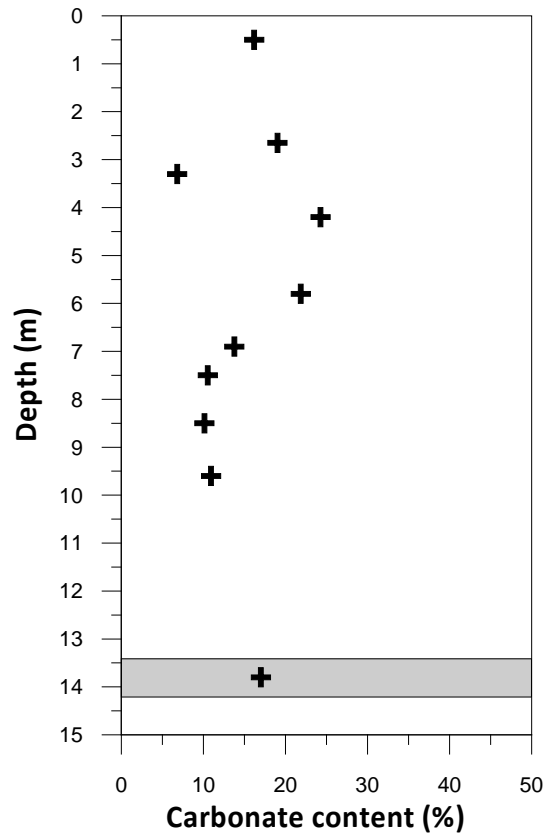
Figure 54. Carbonate content profile.
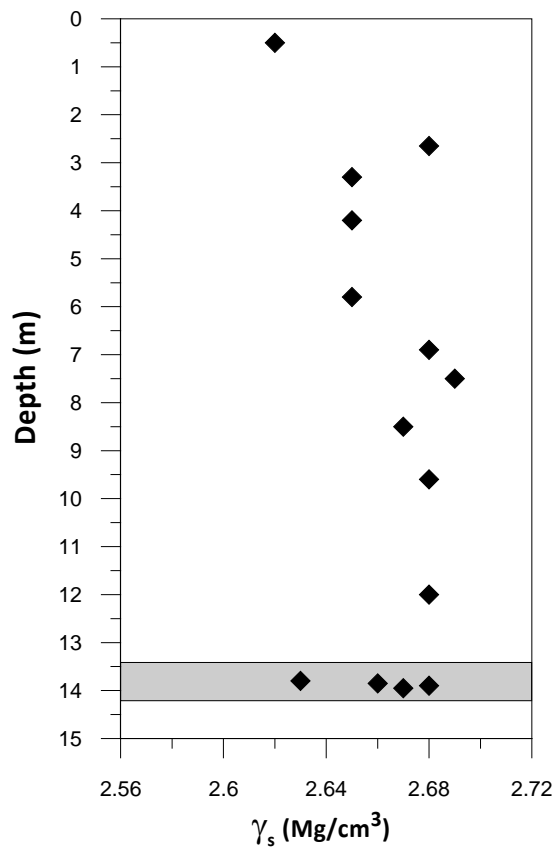
Figure 55. Specific weight of solid particles profile.

5.2 EXPERIMENTAL METHODOLOGY IN THE SOFT SOIL PROJECT

This section summarizes the testing methodology followed in the soft soil project. Some examples of the results obtained are included. More details about equipment and testing procedures are given in Arroyo et al. (2012).

5.2.1 OEDOMETER TESTS

Oedometer tests were carried out in a CRS oedometer. The procedures used for CRS oedometer tests include the following main steps:

i.   *Saturation stage*: a vertical stress equal to σ_{net}= 23kPa and a back pressure at the bottom of the specimen equal to u_w=20kPa were applied in this stage. During this process, the upper face was maintained at atmospheric pressure. A vertical water flow was thus induced to saturate the specimen. The saturation stage lasted between 24 and 48h.

ii. *Load stage*: after the saturation stage, each specimen was loaded with constant rate of strain. The applied strain rate was always less than 0.01%/min, in order to avoid excessive increments of pore pressure. The maximum total stress attained in the tests varied from 800 to 1250kPa.

iii. *Unload stage*: each specimen was unloaded with constant rate of stress. The applied unloading rate was 1kPa/s until total stress equal to 50kPa was reached. Then, dissipation of excess pore pressure was allowed during 24 hours.

Figure 56 shows a example of the variation of the void ratio, e, and the coefficient of consolidation, Cv, with the effective vertical stress, σ_v', during the load stage. The coefficient of consolidation is estimated with the formula developed by Wissa et al. (1971) for interpreting CRS tests. The coefficient of consolidation is defined as:

$$C_V = \frac{h_0^2}{2u_w} \cdot \left(\frac{\Delta\sigma}{\Delta t}\right)$$
Equation 8

Where h_o is the initial height of the specimen, σ is the total vertical stress, u_w is the excess pore pressure at the non-drained face and t is the time.
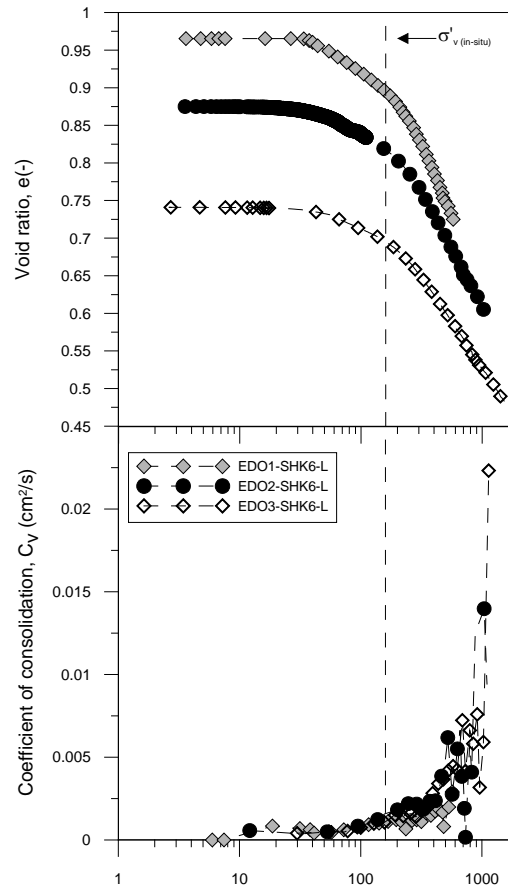
Figure 56. Variation of the void ratio and the coeffient of consolidation during the load stage. Specimens from sherbrooke sample.

5.2.2 TRIAXIAL TESTS

Anisotropically consolidated undrained triaxial compression tests (CAUC) were carried out using two different equipments.

The specimens from Sherbrooke sample were tested in triaxial equipment from the University of Porto (Portugal) while specimens obtained from tube samplers were tested in triaxial equipment of the Geotechnical Laboratory of UPC.

The procedure used in CAUC tests had the following main steps:

i. *Percolation stage:* this stage was carried out under a effective mean stress, p', which varied from 5 to 10kPa. For this, variable isotropic confining stresses $\sigma_3 = \sigma_2 = \sigma_1$ between 15kPa and 30kPa were applied while the back pressure varied from 10 to 20kPa. During this process, the upper drainage line of the sample was kept open (at atmospheric pressure) to induce a water flow through the sample and thus start the saturation process of the soil. This stage lasted between 36 and 48 hours.

ii. *Saturation stage:* full saturation of the specimens was ensured by applying a pressure ramp. The confining stress and back pressure was increased up to 510kPa and 500kPa, respectively, whereupon the effective mean stress was always equal to p'= 10kPa. Applied load rate at this stage was equal to 30kPa/hour. At the end of the ramp, the pressures were kept at their final value to achieve complete saturation of specimens. This stage was lasted 48 hours.

iii. *Anisotropic consolidation stage:* each specimen was consolidated anisotropically to the in situ vertical effective stress, following a stress ratio defined by K_0 value (inferred

from CPTU tests, 0.55 for 13.8m depth). The back pressure was kept constant at u_w= 500kPa. The loading rate during anisotropic consolidation stage was 10kPa/hour. The final stress values were kept for 48 hours to ensure the excess pore pressure dissipation prior to the shearing stage.

iv. _Undrained shearing stage:_ this stage was prolonged until reaching a axial strain equal to 20%. During the shearing, the confining stress was kept constant at the final value of the consolidation stage. The excess pore pressure induced during undrained shearing was measured. For the specimens tested in the University of Porto, a loading rate of 2%/hour was used, and thus the shearing stage lasted approximately 12 hours. In the case of the specimens tested in the UPC, a loading rate of 60%/hour was used.

Figure 57 shows an example of the stress path of the specimens from Shelby (ϕ_{int} =76mm).
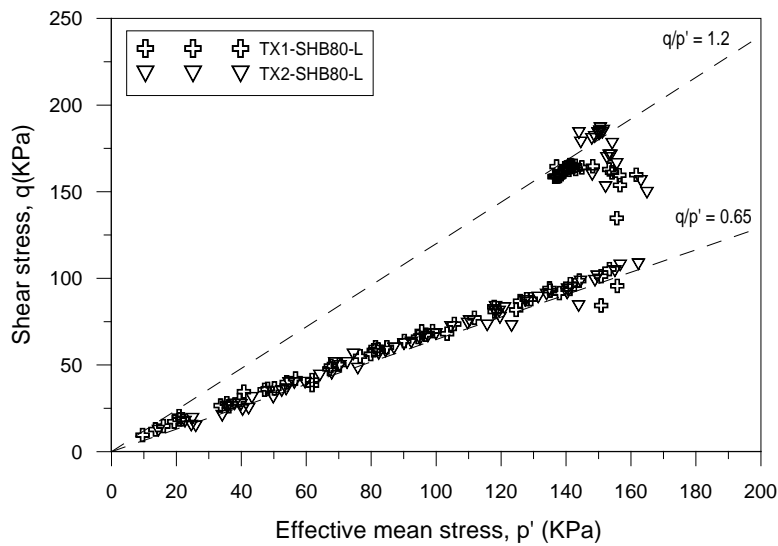
Figure 57. Stress path from Shelby (ϕ_{int} =76mm) specimens.

Chapter VI. DETAILED ANALYSIS OF CT RESULTS

This chapter summarizes the process of calibration and the results of the CT scans analysis.

6.1 CT SCAN CALIBRATION

X-ray attenuation depends on the bulk density of the sample, its porosity, water content, and chemical composition (atomic number effect, see Chapter II, section 2.3.7) in a complex way.

Therefore, experimental calibration is necessary to properly determine the wet bulk density of soils. In the literature several examples of such calibrations can be found (Orsi & Anderson (1999); Ashi (1997); Cortellazzo et Al. (1995)), however these calibrations cannot be applied directly in this study for several reasons:

- Acquisition parameters such as tube voltage, tube current and others that influence the CT numbers are not the same as those used in this work. Furthermore, the information about the acquisition parameters used is not usually published.
- The soils used for the calibrations have a very different chemical composition compared with the soils of this study. The calibration curve of a soil with high percentage of calcium carbonate is very different from a soil without any calcium carbonate.
- The degree of saturation of the soils used for calibrations differs greatly. The CT values of water and air are very different and the impact on the final results also.
- The relation between voxel size and particle size is different. This relation influences on CT values is known as Partial Volume Effect (see Chapter II, section 2.3.7).

In consequence, it was decided to perform a new calibration specifically for these tests. A complementary experimental campaign was required for that purpose. The following subsections present the objectives of that campaign, the materials employed, the experimental methodology, the results obtained and their discussion.

6.1.1 OBJECTIVES

The general objective of the calibration campaign was to obtain an appropriate calibration curve relating CT values of the tube and Sherbrooke samples to their wet bulk density. Due to the nature of the soils and after initial inspection of the CAT results, some aspects were identified for particular study

- ❖ The impact of the $CaCO_3$ content on the CT values.
- ❖ Whether the source of $CaCO_3$ (natural or industrial origin) is important.
- ❖ The impact of particle size on CT values.
- ❖ The level of background noise in the CT scanner.
- ❖ The occurrence of beam hardening artifact during CT scans of tube samples

6.1.2 MATERIALS

The choice of materials for the calibration specimens was based on the materials available at the Soil Mechanics Laboratory of the UPC.

Among available materials, a mixture of silica sand and Kunigel bentonite (80% and 20% by weight) and Boom clay were chosen.

Both Kunigel bentonite and Boom clay are soils widely studied. Several publications (Decleer et al. 1983; Rhattas 1994; Griffault et al. 1996; de Craen et al. 2000; Nakashima, 2004) present their grain size distribution, mineralogy and chemical composition. The following tables show the chemical and mineralogical composition of both materials.

Table 7. Chemical component (wt%) of Boom clay and Kunigel bentonite.

Chemical component	Kunigel bentonite Nakashima (2004)	Boom Clay Decleer et al. (1983)
SiO_2	70.7	62.65
Al_2O_3	13.8	14.61
TiO_2	0.2	0.83
Fe_2O_3	1.49	3.35
FeO	0.62	1.33
MgO	2.26	1.19
CaO	2.3	1.36
Na_2O	2.56	0.42
K_2O	0.33	3.07
P_2O_5	-	0.09
Organic carbon	-	1.66

Table 8. Mineral composition(wt%) of Boom clay and Kunigel bentonite.

Mineral	Kunigel bentonite (Nakashima 2004)	Boom Clay Griffault et al. (1996).
Kaolinite		10
Illite		17
Smectite		
Chlorite		2
Montmorillonite	46-49	29
Quartz	29-38	20
Albite	-	2.8
Plagioclase	-	6
Feldspar	2.7-5.5	
Calcite	2.1-2.6	1-5
Dolomite	2.0-2.8	0.9
Siderite	-	0.4
Analcite	3.0-3.5	
Pyrite	0.5-0.7	4.2
Hematite	-	2.7
Rutile	-	1
Apatite	-	0.1
Organic matter	0.33-0.36	1-3

The tables above show that the percentage of mineral or chemical elements that can distort the CT values, such as calcite and CaO is less than 3%. Consequently, both the chemical composition and mineralogy of the two materials indicate that these materials are suitable for use in calibration. However, as a further verification, several determinations of calcium carbonate content were made in the laboratory. For this purpose the calcimeter Bernard (UNE 103200-1993) has been used. The results obtained vary from 1 to 2% in both materials. According to Boespflug et al. (1995) calcium carbonate contents of less than 5% causes no shift in the CT values.

Regarding the grain size distribution, Boom clay (Rhattas, 1994) presents mainly silt fraction ($2\mu m < \phi < 0.075mm$) and the clay fraction ($\phi < 2\mu m$). Instead the mixture of silica sand and Kunigel bentonite presents a more heterogeneous grain size distribution. Figure 58 shows grain size distribution of these materials and also of Castello soil.
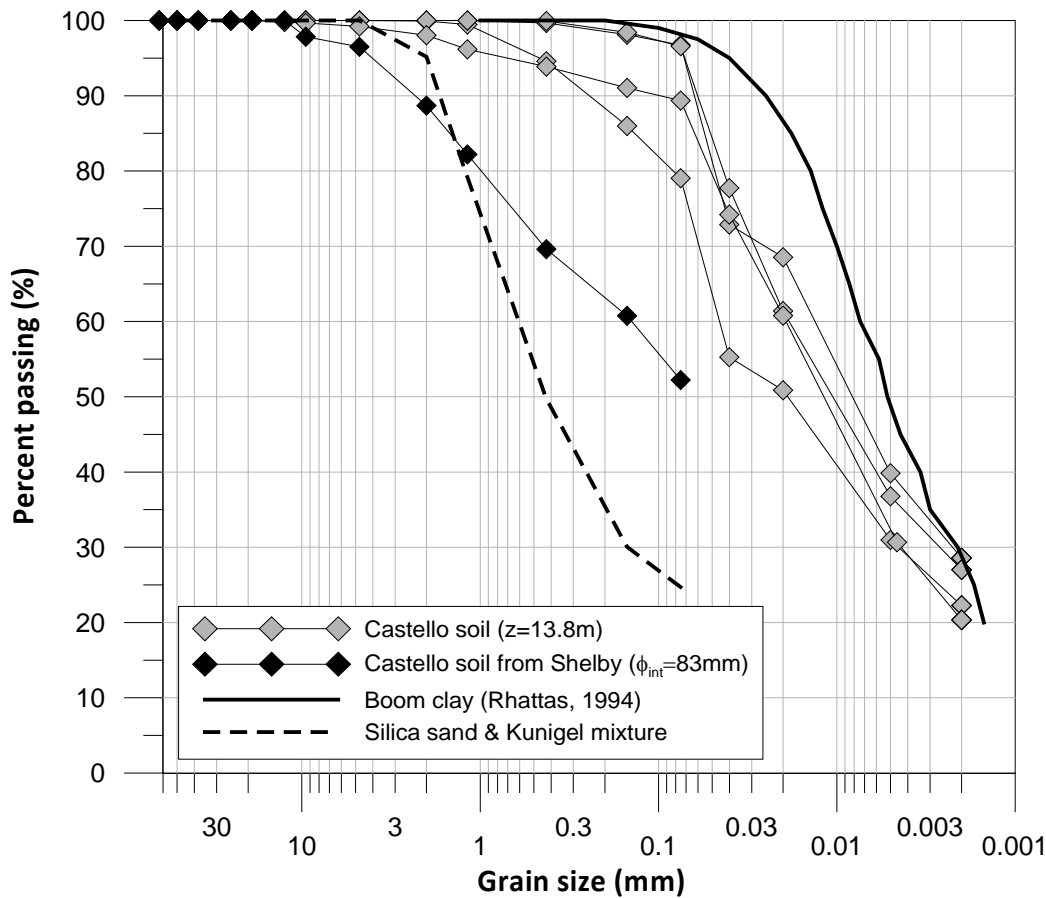
Figure 58. Grain size distribution of calibration materials.

The grain size distribution of Boom clay allows to obtain a CT value most representative of the bulk density because there is no possibility of occurrence of Partial Volume Effect (see Chapter II, Section 2.3.7). In addition, the soil under study presents a grain size distribution similar to Boom Clay.

The grain size distribution of the silica sand and Kunigel mixture allows to study the influence of grain size on CT values and identify partial volume artifacts.

The third material used is calcium carbonate ($CaCO_3$). As mentioned previously, one of the objectives was whether the source of $CaCO_3$ was important. For this, industrial and natural calcium carbonate was used.

To obtain natural calcium carbonate, a lot of shells were collected from the beach (El Prat del Llobregat). Then these shells were cleaned and dried. Finally, shells were crushed until 100% of the material passes through the # 40 sieve (0.425 mm).

6.1.3 TESTING PROGRAM

A total of 24 samples were prepared for calibration studies. Table 9 summarizes their characteristics. All these samples were subject to CT scans were using the same parameters and equipment previously employed for the tube and block samples of Castello.

Table 9. Calibration samples

ID-Sample	Soil type	CaCO$_3$ content	Origin source of CaCO$_3$	ρ wet bulk Mg /cm^3
CAS-1	Castello soil	17 %	own	1.62
CAS-2				1.76
BC-C-1	Boom clay	17 %	natural	1.56
BC-C-2				1.65
BC-C-3				1.75
BC-C-4				1.77
K-C-1	Silica sand+bentonite Kunigel mixture	17 %	natural	1.65
K-C-2				1.84
K-C-3				1.95
BC-1	Boom clay	1-3 %	own	1.42
BC-2				1.59
BC-3				1.69
K-1	Silica sand+bentonite Kunigel mixture	1-3 %	own	1.66
BC-HC-1	Boom clay	22 %	natural	1.42
BC-HC-2				1.72
BC-HC-3				1.72
BC-HC-4				1.86
BC-HIC-1	Boom clay	22 %	industrial	1.56
BC-HIC-2				1.60
BC-HIC-3				1.76
BC-LC-1	Boom clay	8 %	natural	1.27
BC-LC-2				1.59
BC-LC-3				1.57
BC-LC-4				1.69

The composition of the different calibration samples was selected to answer the different objectives set out before. Namely

Obtain the baseline calibration curve

To achieve this goal remoulded samples of Boom clay were mixed with natural calcium carbonate with a proportion (17%) typical of Castello soils at $z = 13.8$ m . These are samples BC-C- in the table. Some samples of remoulded Castello soil (CAS- in the table) were also used for this purpose.

Impact of the calcium carbonate content

To determine the influence of CaCO$_3$ content, remoulded samples of Boom clay with 0%, 8% and 22% added CaCO$_3$ (natural origin) were produced. These are samples BC-, BC-LC- and BC-HC, respectively.

Influence of the source of calcium carbonate

Remoulded samples of Boom Clay with 22% added CaCO$_3$ from industrial origin were produced. These are samples BC-HIC- in the table. In order to be compared with samples BC-HC- where the same amount of natural carbonate was added.

Influence of grain size distribution.

The effect of grain size distribution was explored using a silica sand and Kunigel bentonite mixture. A first sample series (K-C- in the table) of variable bulk density and 17% $CaCO_3$ samples was made. A single sample without $CaCO_3$ was also employed (K- in the table).

Evaluate background CT scanner noise

To determine the own noise of the CT scanner is necessary to use homogeneous materials. Therefore, to achieve this objective water samples of $\phi \sim 80mm$ and a PVC piston were scanned.

Beam hardening artifact check

In order to check if the steel tube samplers cause a beam hardening artifact, Castello soil from one of the tubes (Shelby $\phi_{int} \approx 76mm$) was scanned after extraction from the tube and then, again, scanned after being covered by a steel tube.

6.1.4   SAMPLE FORMATION

The aim was to produce remoulded samples in which the final wet bulk density was known and the CT results would be easily interpretable. This objective imposed some constraints on sample formation:

o   Samples should be obtained through oedometric consolidation because compaction is prone to non-homogeneities (aggregates).
o   Samples should be cylindrical to avoid edge artifacts in the CT scans (see Chapter II, Section 2.3.7).
o   The relationship between pixel size and particle size should be similar to the reference scans. Therefore, the diameter of the samples should be similar to the tube sampler ($\phi \sim 80mm$).
o   The height of the samples had to be sufficient to allow enough slices for a representative statistical analysis. Accordingly the height was determined to be of 4 cm for all samples (disregarding the thickness of the porous stone).
o   The sample container should be of a material that would not induce a beam hardening artifact. Accordingly, PVC tube was used (see Figure 59). That also had the advantage of being non-corrosive to avoid iron migration that would cause an atomic number effect.
o   A large number of porous stones were needed, because they could not be removed once the consolidation was finished. The fact of removing stones could disturb the volume of the sample, and therefore adding an error in the measurement of wet bulk density. Considering this, it was decided to manufacture laboratory porous stones (see Figure 59) using standard silica sand (CEN UNE-EN 196-1:1996) sieved (0.15mm < ϕ < 1.18mm) and glue (Araldite).

The restrictions on the height and diameter of the samples causes unable to use a conventional oedometer cells, and the use of an altered Mayer oedometer to have more gauge (see Figure 60).

Figure 59. Experimental setup, unassembled.

The process for the preparation of samples for subsequent consolidation involves several steps:

1) Producing porous stones (the drying requires 24 hours, and only two molds are available).
2) Prepare the PVC tube. Cut to the required height (varies depending on the sample to consolidate. Drill a serie of holes in the PVC tube base (taking into account the thickness of the porous stone) to allow drainage during consolidation.
3) Crush the air-dried material (Boom clay and the silica sand and Kunigel bentonite mixture) until 100% of the material passes through the #40 sieve (ASTM series). In the case of sand and bentonite mixture, only 50% since the rest of the particles are larger by design.
4) In case of samples in which calcium carbonate from natural origin was added, shells were crushed until 100% of the material passes through the # 40 sieve (0.425 mm).
5) Remould the material adding distilled water to slightly above the liquid limit ($W_{L-Boom\ clay}$ = 70% y $W_{L-Kunigel\ bentonite}$ = 474%).
6) Place the saturated porous stone and a filter paper (to prevent the loss of fine particles) at the lower end of the PVC tube.
7) Pour the remolded material in the PVC tube.
8) Place the upper saturated porous stone along with a filter paper.
9) And finally, placing the sample in a methacrylate container (see Figure 60) and pour distilled water in to keep the sample saturated during consolidation.

Once prepared, the sample is placed on the Mayer oedometer for consolidation (see Figure 60). The consolidation process to achieve the predetermined height (fixed volume) of the sample took from 3 to 12 days, depending on the wet bulk density target.

Figure 60. Experimental setup, assembled.

Following samples preparation, computed tomography tests were conducted on the same scanner used in the reference scans (Siemens Somatom Spirit® scanner), with the support of Dr. Hector Arias.

Three CT scans were carried out. The acquisition parameters used were the same as in the reference scans of the tube samples (see Table 1, Chapter III). The calibration samples were placed on the table of the CT scanner as shown in Figure 61.

Figure 61. Placement of the calibration samples for the CT scan test.

6.1.5   RESULTS

6.1.5.1   Post processing overview

To analyze the CT scans, two programs have been used, GIMIAS and ImageJ. GIMIAS is used as support, because ImageJ, even with the large amount of plugins available has limitations with compressed DICOM images (output format of CT equipment).

The main limitation is that ImageJ opens the stack of slices in a disorderly way. This happens because ImageJ cannot access to the DICOM header, consequently the slices are sorted by the file name. This problem is solved by two operations:

1)   GIMIAS was used to find the slice order.

2)   A script in Matlab was used to rename the slices.

Once that done, image processing was performed entirely with ImageJ program.

A schematic overview of steps used in the analysis of CT scans is:

1)   Locate each calibration sample in CT scans.

2)   Extract from the stack (a set of CT scan slices) the slices made at the locations of the calibration sample.

3)   ImageJ does not allow the analysis of a certain number of slices within a stack, but only of an entire stack or a single slice. A substack with all the slices intersecting the calibration sample is created. Within the substack a ROI (region of interest) closely corresponding to the sample volume is created for further processing (Figure 62).

4)   The main statistics of gray values from the ROI (average, standard deviation, minimum and maximum) are calculated.

5)   Once results are obtained, gray values are transformed to CT values through the following relation:

$$CT\ value = Gray\ value \cdot m + b \qquad\qquad \text{Equation 9}$$

Where *m* is the rescale slope and *b* the rescale intercept.
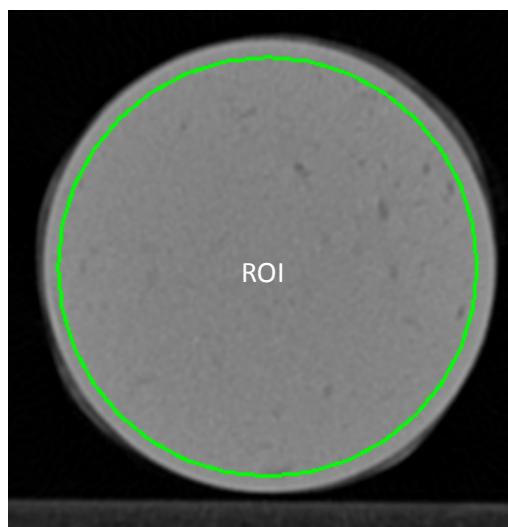
Figure 62. ROI located inside the CT slice of calibration sample BC-HC-1.

Table 10 shows statistical results (average and standard deviation) from all calibration samples. One can see that sandy samples (silica sand and Kunigel mixture) show higher standard deviations. This is probably due to partial volume artifacts. Sample BC-LC-1 also presents high standard deviation.

During the visual inspection of the CT scans, one can see that the sample BC-LC-1 presents slurry (see Figure 63), and therefore it is dismissed from the calibration study.

Table 10. Statistical results from all calibration specimens.

ID-Sample	$\rho_{wet\ bulk}$ Mg /cm^3	Mean CT value (HU)	$\sigma_{CT\ value}$ (HU)
CAS-1	1.62	1031	63
CAS-2	1.76	1107	68
BC-C-1	1.56	1028	58
BC-C-2	1.65	1079	66
BC-C-3	1.75	1105	64
BC-C-4	1.77	1137	68
K-C-1	1.65	876	137
K-C-2	1.84	1096	125
K-C-3	1.95	1230	99
BC-1	1.42	849	51
BC-2	1.59	945	44
BC-3	1.69	1015	46
K-1	1.66	837	137
BC-HC-1	1.42	1056	61
BC-HC-2	1.72	1087	65
BC-HC-3	1.72	1118	68
BC-HC-4	1.86	1236	57
BC-HIC-1	1.56	939	45
BC-HIC-2	1.60	979	69
BC-HIC-3	1.76	1097	60
BC-LC-1	1.27	648	340
BC-LC-2	1.59	960	66
BC-LC-3	1.57	954	67
BC-LC-4	1.69	1003	65
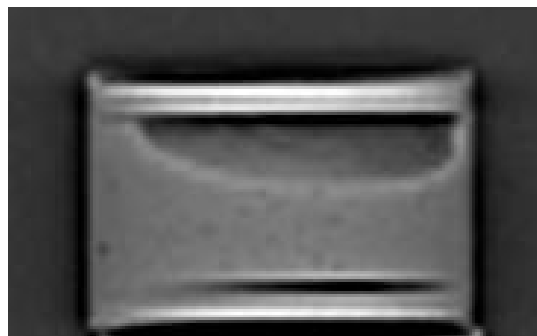
Figure 63. Topogram of BC-LC-1 remoulded sample.

Figure 64 shows the obtained values (average CT value) from all calibration samples. Some general considerations are:

- Samples of Castello soil coincide quite well with those of Boom clay with a high content of calcium carbonate.
- Sandy samples show lower CT values than the rest of soil samples.

Then a more detailed study is made.
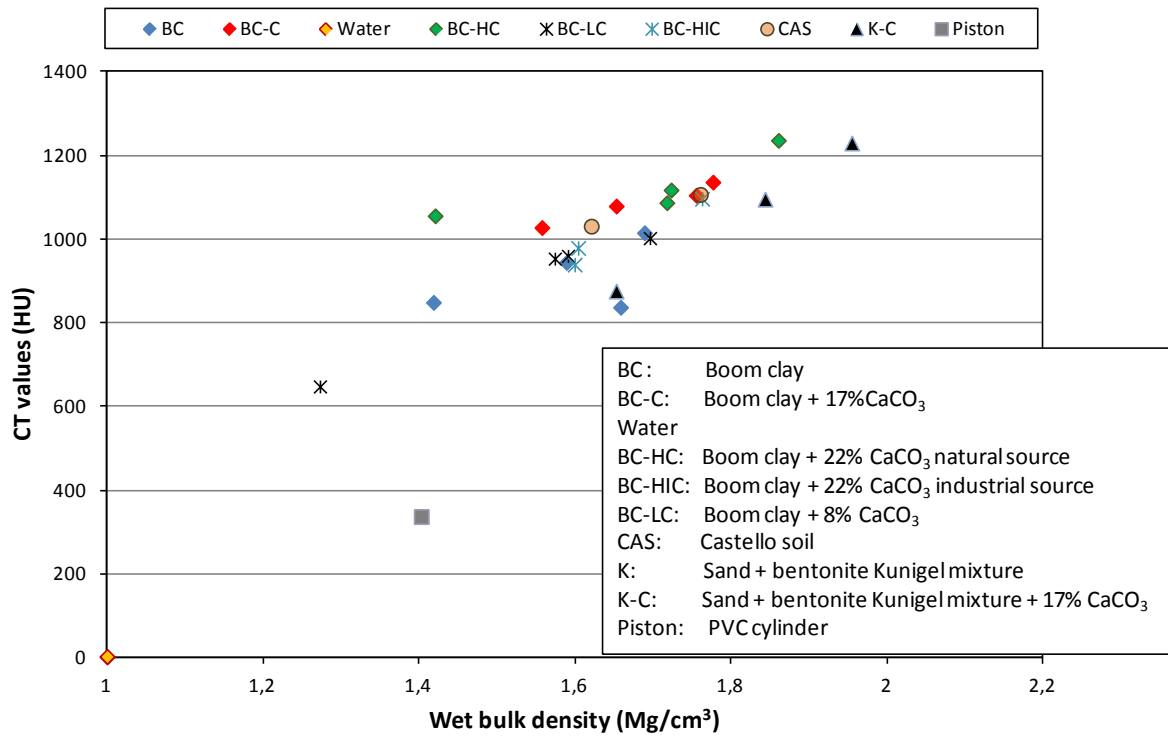
Figure 64. Results of the calibration samples.

6.1.5.2 Effect of carbonates

Figure 65 shows the results of the clay/silty samples (Boom clay and Castelló soil) according calcium carbonate content (%). The trend lines of the samples with 17% and 22% $CaCO_3$ are the same, and are above the ones with less calcium carbonate content. The conclusion is that the cation Ca^{+2} cause a shift in the calibration curve, although the difference between 17% and 22% is not significant. Moreover, no differences are observed between samples with different source of $CaCO_3$.

As for the samples with $CaCO_3$ content of 1-3% and 8%, the trend lines coincide. Consequently it can be concluded that calcium carbonate content equal to or less than 8% does not cause shift in the CT values.
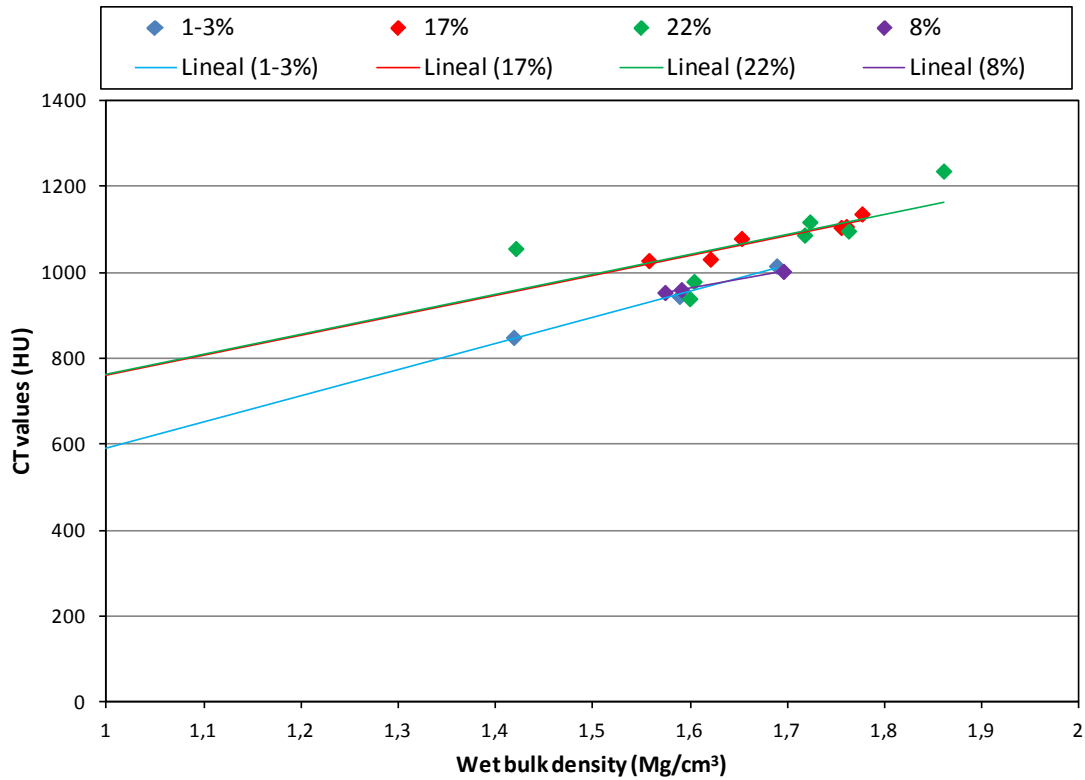
Figure 65. Results as a function of CaCO₃ content.

Table 11 shows regression lines and total cumulative squared error (R²)for both type of samples.

Table 11. Regressions lines and total cumulative squared error. Effect of carbonates.

Type of sample	Regression line	R^2
CaCO₃ content of 2-8%	$CT value = 609.3\rho_{wet\ bulk} - 16.8$	0.99
CaCO₃ content of 17-22%	$CT value = 463.8\rho_{wet\ bulk} + 298.7$	0.90

6.1.5.3   Effect of grain size

In the Figure 66 the results have been plotted taking in account the grain size distribution, meaning that samples of clay / silt (Boom clay and Castelló soil) and samples with a high percentage of sand (sand/Kunigel mixture) are grouped separately. It can be observed that the regression line derived for the sandy samples is below the one deduced from the clay/ silt samples; that is, for the same bulk density the sandy samples appear less attenuating.

The observed difference between the two types of samples is due to chemical composition of the materials. Silica sand of the mixture is composed by SiO_2 and the silts and clays contain iron, aluminum, silicates, and other elements. The elemental composition produces different linear attenuation coefficients between sand, silt, and clay. The attenuation coefficient of the silica sand is lower than the attenuation coefficients of clay and silt, because aluminium, iron and other elements show upper attenuation coefficents as can see in Hubble (1969).

Moreover, it is suspected that sandy samples may have partial volume artifact. Which would means that the real wet bulk density is lower.
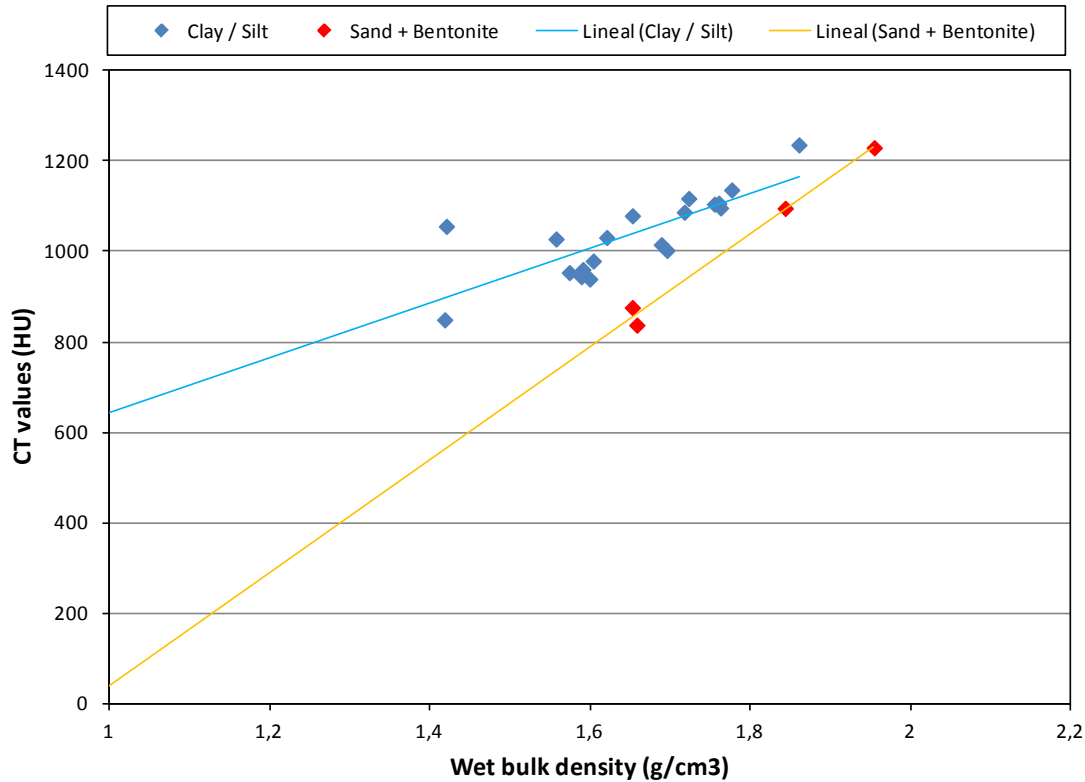
Figure 66. Results as a function of grain size distribution.

Table 12 shows regression lines and total cumulative squared error (R^2) for both types of samples.

Table 12. Regressions lines and total cumulative squared error. Effect of grain size.

Type of sample	Regression line	R^2
Clay/silt samples	$CTvalue = 758.6\rho_{wet\ bulk} - 219.2$	0.75
Sandy samples	$CTvalue = 1250\,\rho_{wet\ bulk} - 1211.4$	0.98

6.1.5.4 Baseline regresion

From what has been shown, the optimal samples to determine a calibration curve for the Castello field samples are the Boom clay samples with $CaCO_3$ content of 17% and the remoulded samples from Castello soil. Because Boom clay samples with $CaCO_3$ content of 22% present more scattering.

To obtain the calibration curve is necessary to use a linear regression from the pair-wise values of the calibration samples (Y: wet bulk density and X: CT values).

$$E(Y/X = x) = \alpha + \beta x$$
<div align="right">Equation 10</div>

Where α and β are constants, known as the regression coefficients, which are the intercept and slope, respectively, of the straight line. This equation represents the regression of Y on X (see Figure 67).

For linear regression, the degree of linearity in the relationship between two random variables may be measured by the statistical correlation, in particular, by the correlation coefficient ($\hat{\rho}$).

$$\hat{\rho} = \frac{1}{n-1} \cdot \frac{\sum_{i=1}^{n} x_i y_i - n\bar{x}\bar{y}}{s_X s_Y}$$

Equation 11

$$-1 \leq \hat{\rho} \leq +1$$

Where n is data pairs size and $\bar{x}$, $\bar{y}$, s_X, s_Y are, respectively, the sample means and sample standard deviations of X and Y.

When the correlation coefficient is high, close to ± 1, one can expect high confidence in being able to predict the value of one variable based on information about the value of the other (control) variable.

The estimated correlation coefficient according to Equation 11 is:

$$\hat{\rho} = 0.95$$

Therefore, for this group of samples there is a strong linear relationship between wet bulk density and CT number as shown in Figure 67.
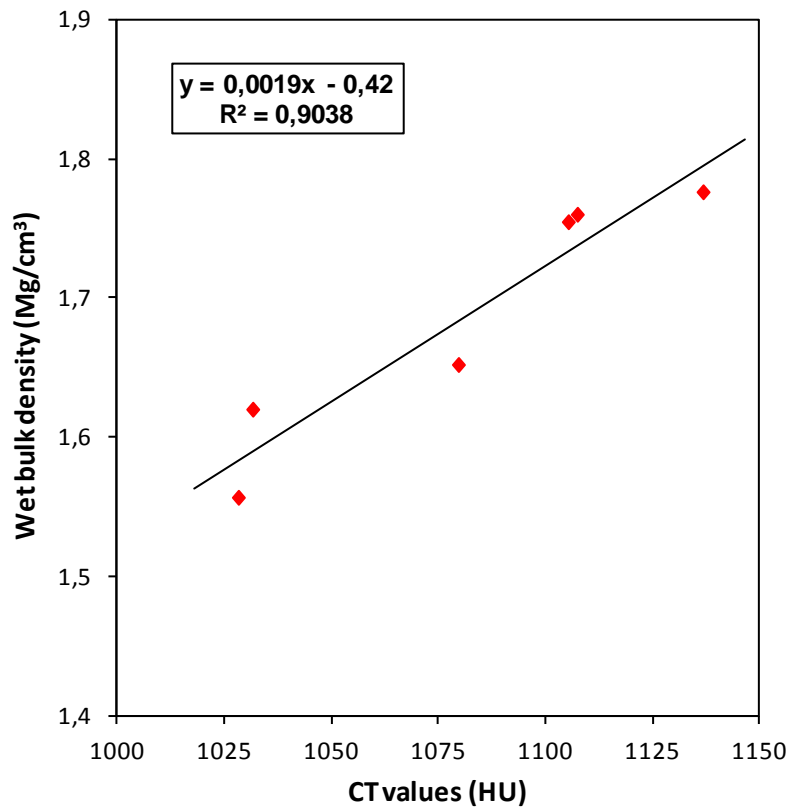
Figure 67. Linear relation between wet bulk density and CT values.

The confidence interval of regression equation would be appropiate to know, which should provide some measure of the range of the true equation.

Since the regression coeficients α and β are estimated from finite samples of size n, they are individually t-distributed with (n-2) degrees-of-freedom; therefore, the mean value $\bar{y}_i = E(Y/X = x_i)$ estimated from the linear regression equation at $X = x_i$ will also have t-distribution with (n-2) d.o.f, and the confidence interval too:

$$\langle \mu_{Y/x_i} \rangle_{1-\delta} = \bar{y}_i \pm t_{\left(1-\frac{\delta}{2}\right),n-2} \cdot s_{Y/x} \sqrt{\frac{1}{n} + \frac{(x_i - \bar{x})^2}{\sum(x_i - \bar{x})^2}} \qquad \text{Equation 12}$$

where $s_{Y/x}$ is the conditional standard deviation of Y and $t_{\left(1-\frac{\delta}{2}\right),n-2}$ is the value of the t-distributed variate at probability of $\left(1 - \frac{\delta}{2}\right)$ with (n-2) d.o.f. (tabulate tables, see Ang & Tang, 2006). Among the confidence intervals of Equation 12 at the selected discrete values of x_i, the interval will be minimum at $x_i = \bar{x}$, the mean value of X. Connecting these discrete points along the regression line should yield the appropriate confidence interval of the regression equation.

To determine the 95% confidence interval for the regression equation of wet bulk density on CT number, several values of CT numbers must be selected. Graphically, the linear regression line and the 95% confidence intervals are shown in Figure 68.
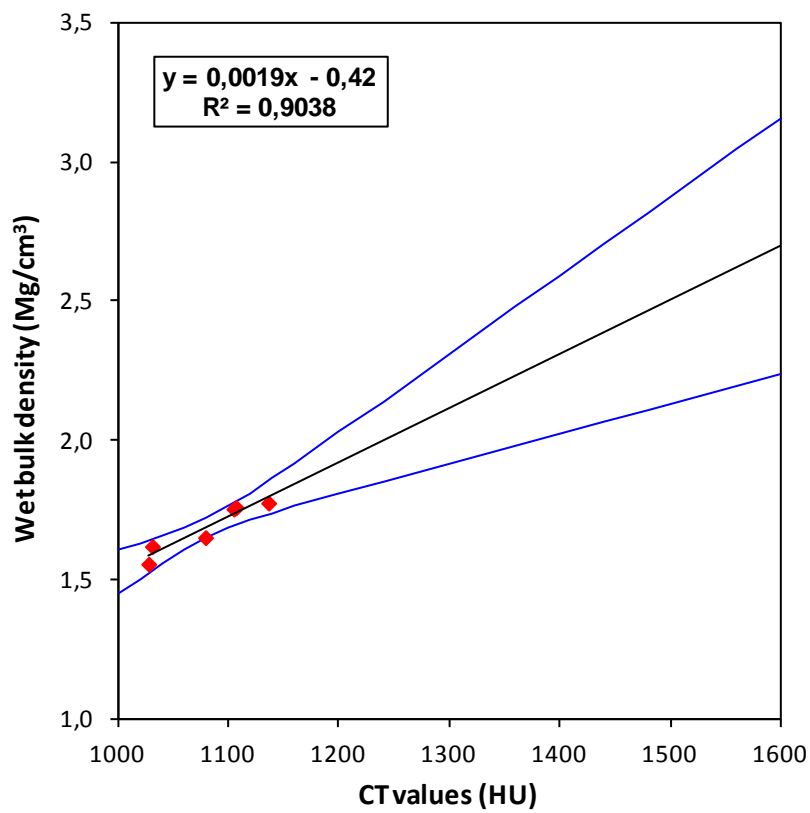
Figure 68. Calibration curve and confidence intervals

6.2   APPLICATION TO THE FIELD SAMPLES

This section summarizes the used methodology for the analysis of the CT scan images that had been previously obtained on the field samples, and the results obtained.

6.2.1   POSTPROCESSING OVERVIEW

A schematic overview of steps used in the analysis of CT scans is:

1) Locate the oedometer and triaxial specimens in the sampler CT scans (see Figure 46 and Figure 50, Chapter IV).

2) Extract from the stack (a set of CT scan slices) the slices made at the locations of the specimen.

3) ImageJ does not allow the analysis of a certain number of slices within a stack, but only of an entire stack or a single slice. A substack with all the slices intersecting the specimen is created. Within the substack a ROI (region of interest) closely corresponding to the specimen volume is created for further processing (Figure 69 and Figure 70).

4) Check for artifacts, such as noise, partial volume effect, edge artifact, ring artifact or beam hardening artifact. If present, remove them.

5) The overall histogram of the gray values from the ROI is obtained.

6) The main statistics of gray values from the ROI (average, standard deviation, minimum and maximum) are calculated and ispected to search for anomalies.

7) Once results are obtained, gray values are transformed to CT values through the Equation 9.

8) Finally the regression line obtained in the calibration is used to obtain the wet bulk density.
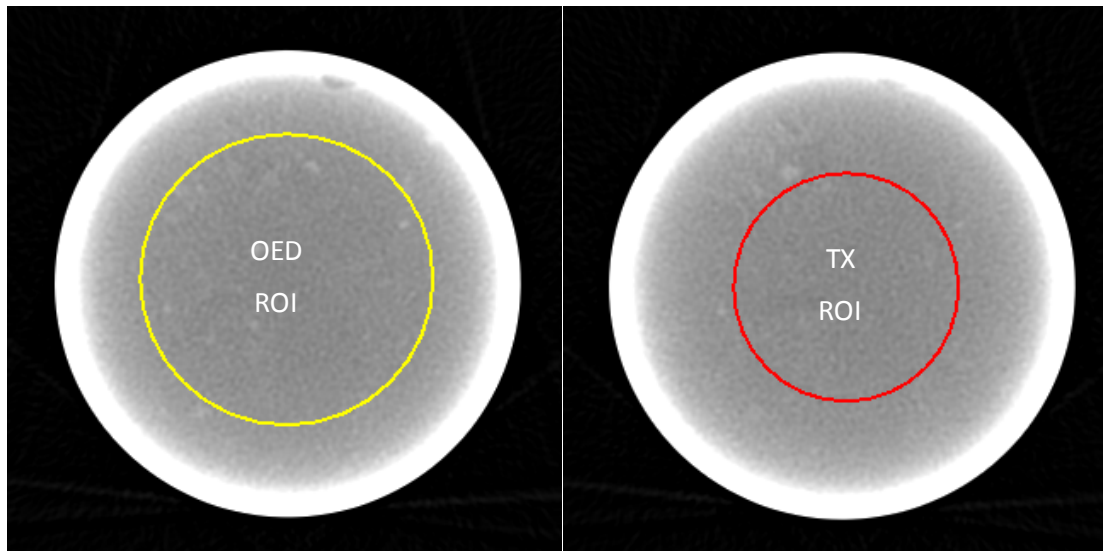
Figure 69. Representative ROI for oedometric and triaxial specimens in CT scans of tube samplers.
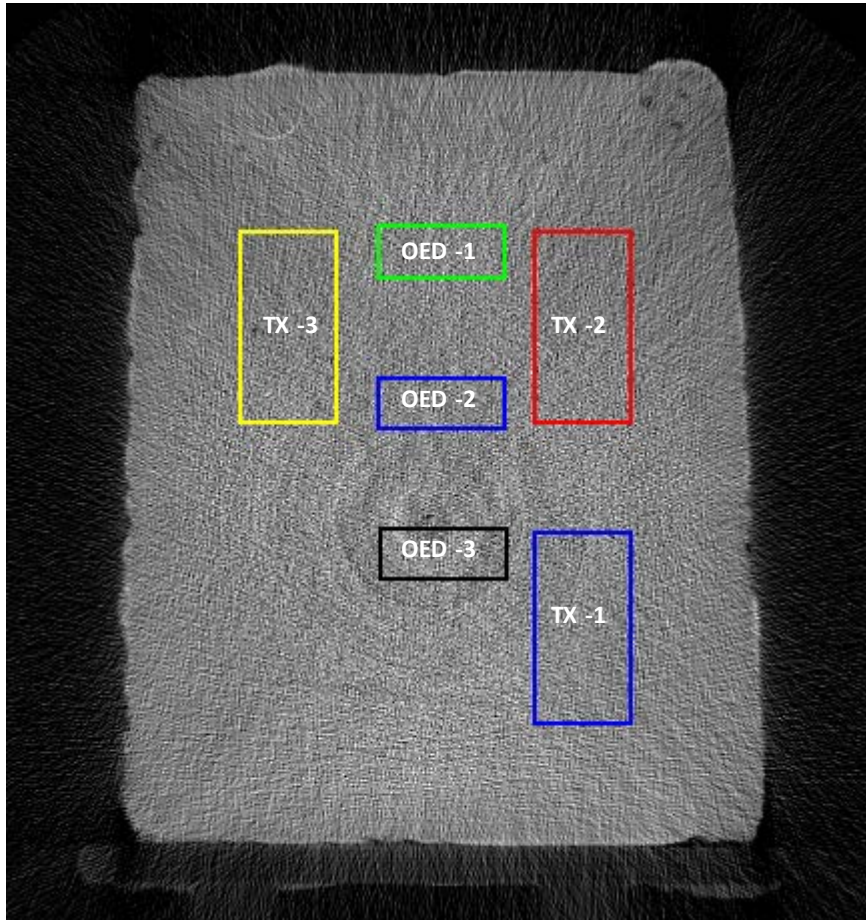
Figure 70. Representative ROI for oedometric and triaxial specimens in CT scan of a Block sample.

6.2.2 ARTIFACT TREATMENT

As mentioned in the methodology, one of the most important steps in postprocessing CAT images is checking for artifacts and correcting them. The artifacts that were suspected included, for the CT scan of the Sherbrooke block sample:

1) High background noise

2) A ring artifact

3) Edge artifacts

And for the tube samples

4) beam hardening artifact (cupping) in all tube samples

5) partial volume effect in the small Shelby sampler ($\phi_{int} \approx 83mm$) since the soil had a significant content of gravel.

6.2.2.1 Noise

As stated in Section 4.2.3 (Chapter IV), the major sources of noise include quantum noise, electronic noise and computational noise. In this study, only quantum noise and computational noise (machine noise) can exist.

A specific calibration test was perfomed to estimate the scanner's density resolution (i.e., computational noise). Following the recommendation of McCullough et al. (1976), CT scans of distilled water samples (usually called phantoms) were performed to compute its standard deviation. Since distilled water is a homogeneous substance, the standard deviation of grey values in this test is equivalent to the density resolution of the scanner. Standard deviations were determined using an ROI located inside the CT image of the core (see Figure 71).

The density resolution thus obtained is 0.016 Mg cm^{-3}.
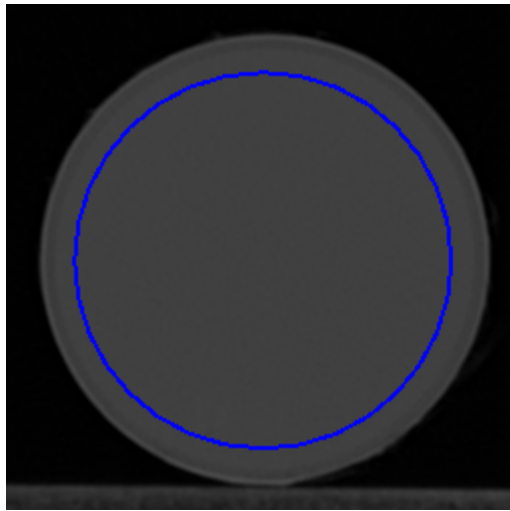
Figure 71. ROI located inside the CT slice of distilled water phantom.

The sherbrooke CT scan images show a lot of noise (quantum noise). Figure 72 shows a slice from sherbrooke CT scan where values of the window width and window level were adjusted to highlight the image noise.
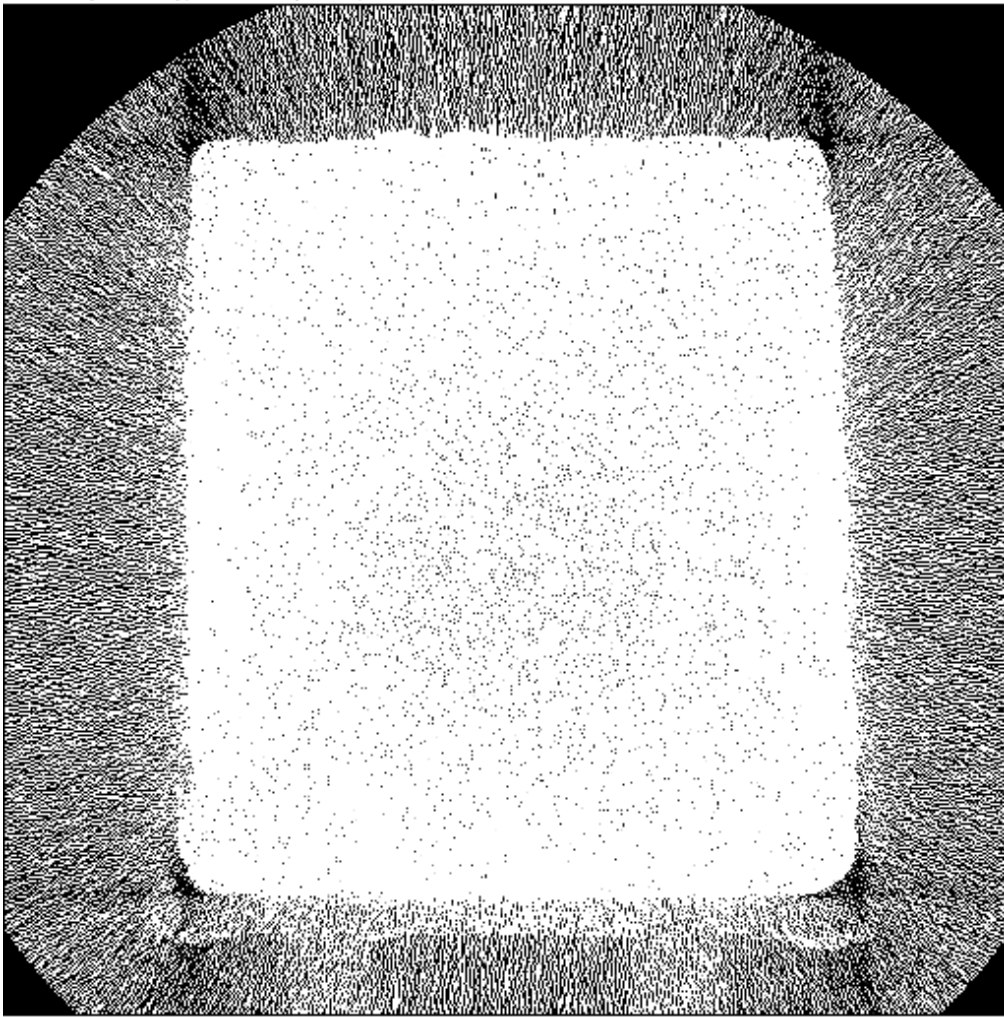
Figure 72. Slice of the Sherbrooke CT scan. Window width equal to 115 and window level equal to 58.

The relation between radiation dose and image noise depends largely on the size of the scanned object. Brooks & Di Chiro (1976) formulate the relationship between radiation and the image quality:

$$D \infty \frac{B}{\sigma^2 \cdot a^2 \cdot b \cdot h}$$

Equation 13

with $B = e^{-\mu \cdot d}$

Where,

D = patient dose

B = attenuation factor of the object (material dependent)

d = diameter of the object

σ = standard deviation of CT numbers (quantum noise)

a = increment

b = sample width

h = slice thickness

Menke (2005) simplified that formula to describe the relationship between dose, noise and size of the object:

$$CTDI_W \cdot \sigma^2 \infty \, e^{(\mu-D)}$$
<div align="right">Equation 14</div>

Where $CTDI_w$ represents the dose, σ is the noise that is equal to the standard deviation of CT values, e is the exponential, μ is the attenuation coefficient for a specific tube voltage, and D is the diameter of the scanned object.

The CT scans of tube and block samples do not differ in any of the scan parameters which influence dose and image quality. They used the same slice thickness (or very similar) and tube voltage (directly related to the dose), the only difference then is the size of the scanned object. The block size is much larger than the tube, consequently, according to the formula of Brooks & Di Chiro (1976) the noise (standard deviation) is considerably higher in the first one.

Within the Sherbrooke CT scan, it was found that the test specimens were located in the area that shows more noise. Oedometer specimens were most affected because they are located in the center of the CT scan (see Figure 73).
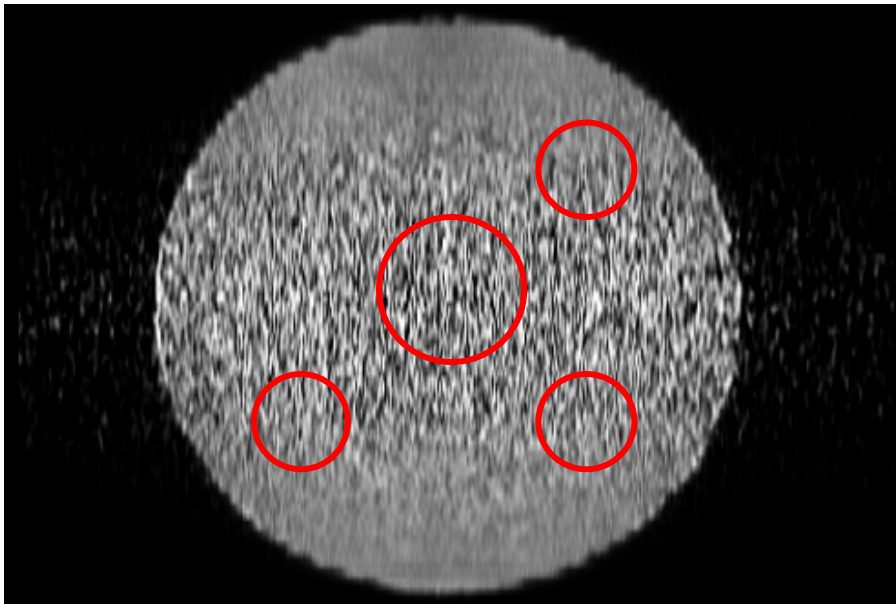
Figure 73. Plant location of the sherbrooke specimens.

To reduce this noise we have followed a multi-step outlier elimination procedure.

One difficulty with treatments of outliers is that there is no unanimously accepted theoretical framework for the treatment of outliers.

Regardless of the decision to remove the outliers, it is necessary to be able to detect its presence. The method of the mean plus or minus three standard deviation is based on the characteristics of a normal distribution for which 99.87% of the data appear within this range (Howell, 1998). Therefore, the decision that consists in removing the values that occur only in 0.13% of all cases does not seem too conservative. Other authors (e.g., Miller, 1991) suggest being less demanding, and use 2.5 or even 2 standard deviations around the mean. This choice obviously depends on the situation and on the perspective defended by the researcher.

Unfortunately, three problems can be identified when using the mean as the central tendency indicator (Miller, 1991). Firstly, it assumes that the distribution is normal (outliers included). Secondly, the mean and standard deviation are strongly impacted by outliers. Thirdly, as stated by Cousineau and Chartier (2010), this method is very unlikely to detect outliers in small

samples. Accordingly, this indicator is fundamentally problematic: It is supposed to guide our outlier detection but, at the same time, the indicator itself is altered by the presence of outlying values.

The median is, like the mean, a measure of central tendency but offers the advantage of being very insensitive to the presence of outliers. For example, when a single observation has an infinite value, the mean of all observations becomes infinite; by contrast, the median value remains unchanged. Therefore, the median is a better indicator. However, as for the mean and standard deviation, it is necessary to define a level of decision: This remains the unavoidable subjective aspect of the decision.

Miller (1991) proposes the values of 3 (very conservative), 2.5 (moderately conservative) or even 2 (poorly conservative). However, in this work, the decision criterion is chosen on basis of physical meaning of values under study and of the results distributions of others samples free from noise.

Phoon & Kulhawy (1999) propose that inherent soil variability can be described concisely by the coefficient of variation (COV) and scale of fluctuation. The typical COVs for the total unit weight (γ) and dry unit weight (γd) are less than 10%. No trends in the COV can be observed as the mean varies from about 13 to 20 kN/m^3. On the other hand, the scale of fluctuation in this case is not relevant because the samples are all of the same depth.

The CT ray values of tube samples that were visibly free from noise were examined to obtain another bound. The average gray value of all samples is 2298.2 and the standard deviation is 155.36, then:

$$COV = \frac{\sigma_X}{\overline{X}} = \frac{155.36}{2298.2} = 0.07$$

It was comforting that this value was smaller that the general one quoted by Phoon & Kulhawy.

Figure 74 shows the histograms of all specimens free from noise. The approximate minimum and maximum gray values recorded are 1800 and 3100. Therefore, gray values lower or higher than 1800 and 3100, respectively, are considered outliers. Thus the decision criterion becomes:

$$M - \delta \leq Xi \leq M + \delta$$

$$M - \delta = 1800 \text{ gray value}$$

$$M + \delta = 3100 \text{ gray value}$$

Where Xi is the distribution free from outliers, M is the median, (M$\pm\delta$) are the minimum and maximum gray values and δ is the threshold. The median value is different in each sample, thus the threshold value also changes to remove outliers lower or higher than minimum and maximum values.
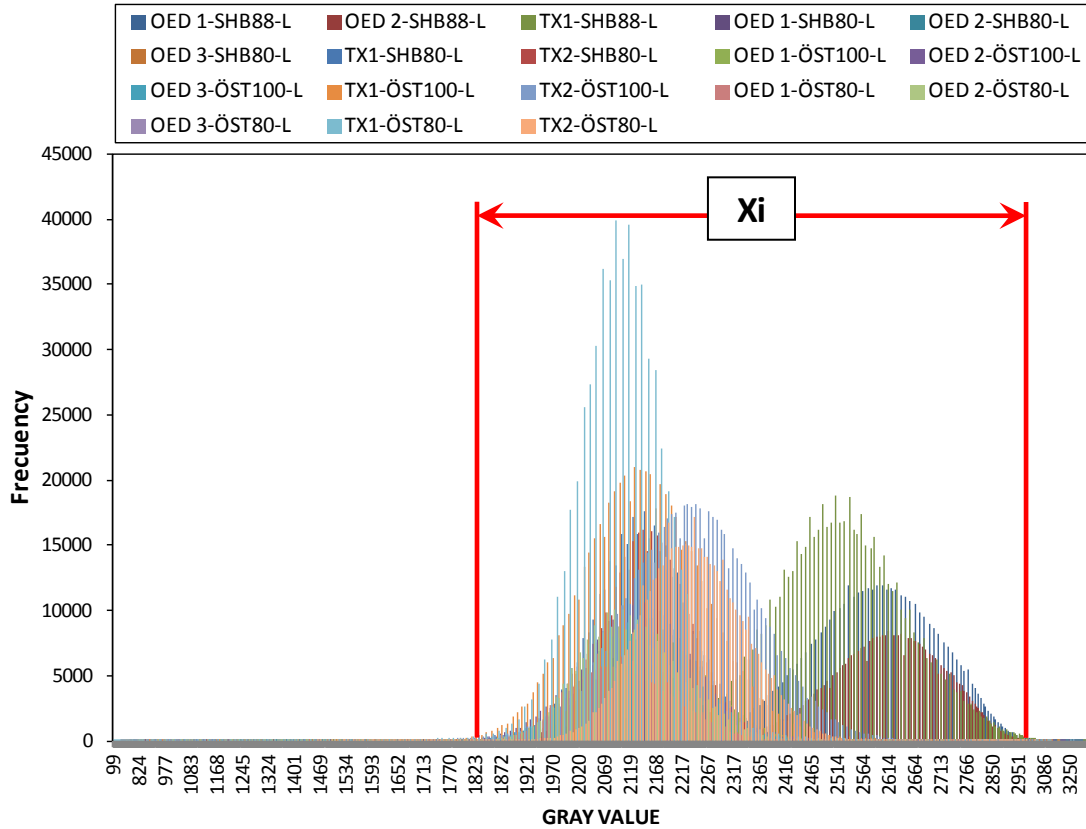
Figure 74. Histograms of gray value for specimens free from noise.

Outlier removal is applied using a predefined filter command of ImageJ. Specifically the Rank-median filter. This filter replaces each pixel outlier value with a median of neighboring pixel values. To apply this filter some parameters must be specified:

- Radius: Determines the neighboring area (in pixels) used for calculating the median.
- Threshold: Determines by how much the pixel must deviate from the median to get replaced.
- Which Outliers: Determines whether pixels brighter or darker than the surrounding (the median) should be replaced.

In our application we have followed several rules

- In the first steps, a large radius was used to filter by a representative median value of the image (the noise is not homogeneous but random).
- In the intermediate and final steps, a smaller radius is to avoid excessive homogenization
- The threshold is decreased gradually (requires more filtering steps) because a threshold too restrictive in the beginning causes a significant change in the median. By using a median unrepresentative in the next step leads to inadequate filtering and an erroneous average value.
- The choice of removing bright or dark values is based on the values observed in the initial histogram. A large percentage of noise is dark outliers.
- The iteration ends when the minimum and maximum values are 1800 and 3100 respectively.

An example of this filtering procedure is now presented; similar results for all samples are collected in an Appendix I.

♦ **OED1-SHK6-L**

The parameters of the filter used are summarized in Table 13.

Table 13. Filtering process of OED1-SHK6-L specimen.

ID step	Radius	Thershold	Which Outliers
Step 1	20	900	Dark
Step 2	20	900	Bright
Step 3	10	800	Bright
Step 4	3	800	Dark
Step 5	3	750	Dark
Step 6	3	700	Dark
Step 7	3	675	Dark
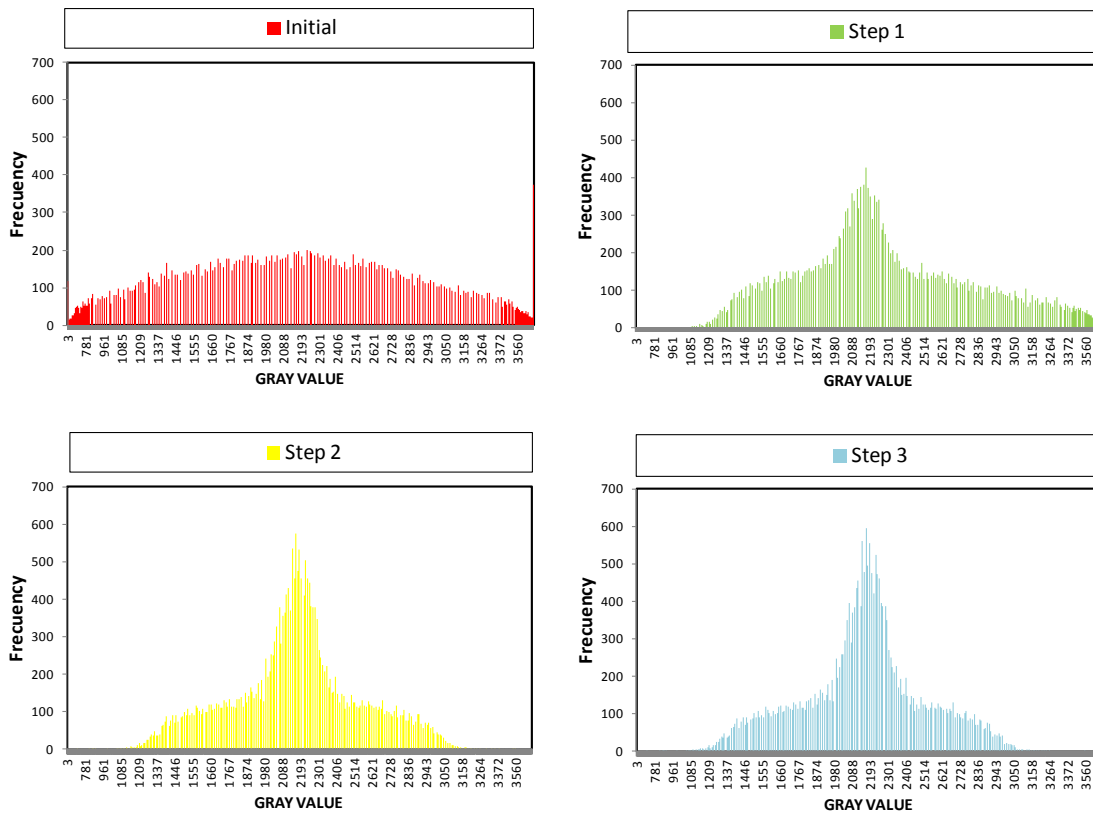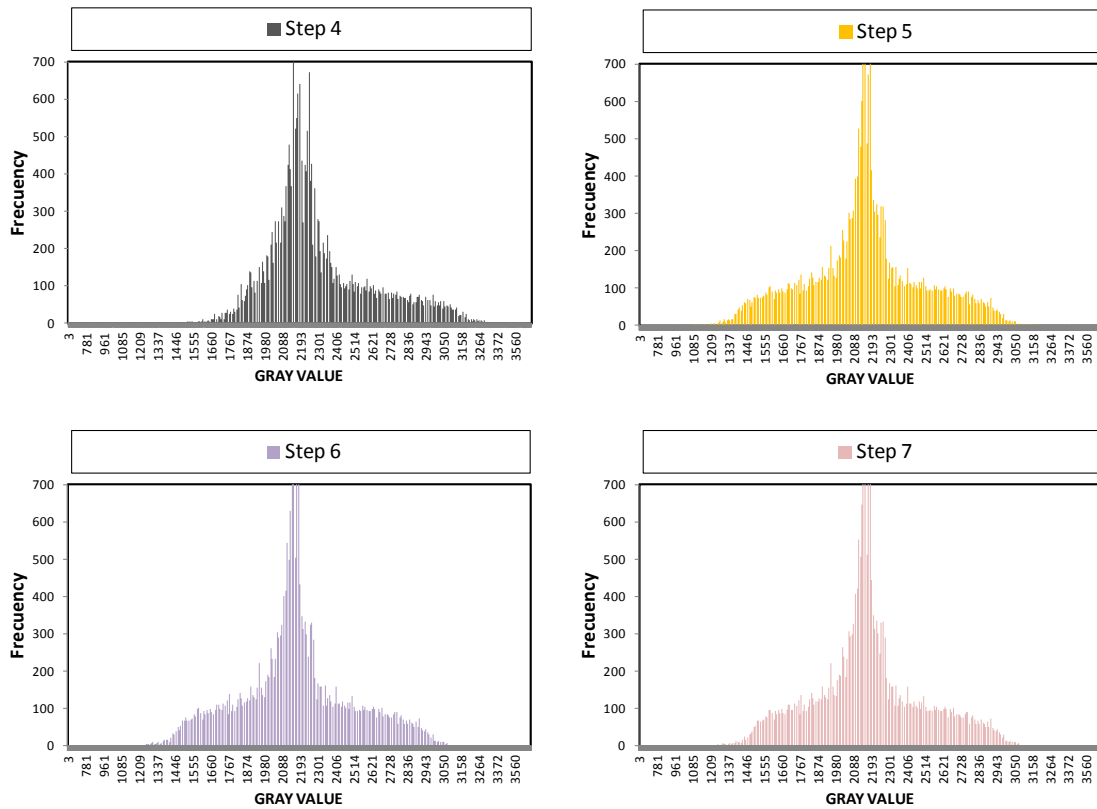
Figure 75. Filtering results of OED1-SHK6-L specimen.

6.2.2.2 Ring artifact

Ring artifact was visible in the CT scan of Sherbrooke (see Figure 76). Unfortunately it is impossible to separately remove this artifact due to the large amount of background noise of the image. This noise prevents using specific methods, such as those involving sinogram treatment. Although the noise and ring artifact are not separately removed, the filters used to remove outliers values also remove dark pixels from the rings.
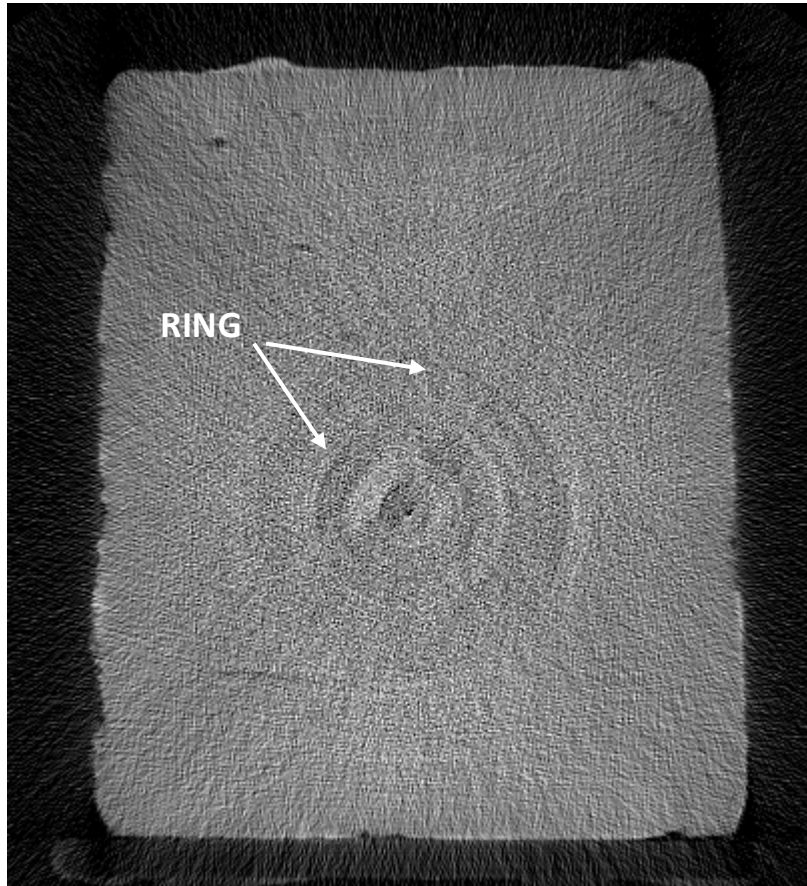
Figure 76. Ring artifact detected on Sherbrooke CT scan.

6.2.2.3 Edge gradient artifact

This artifact appears in the CT scans of objects with edges close to zones with high contrast of attenuation coefficients. This artifact appears as a lucent streak extending a short distance from edges.

Figure 77 shows a slice from sherbrooke CT scan with edge gradient artifact. Since test specimens were not located in the affected areas no treatment was performed.
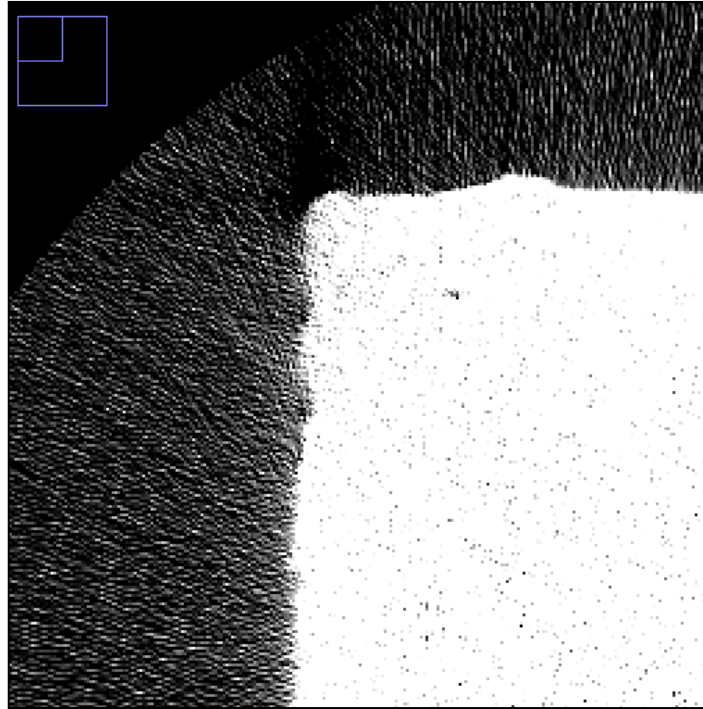
Figure 77. Edge gradient artifact detected on Sherbrooke CT scan (zoom in left side).

6.2.2.4 Beam hardening artifact

To check if a beam hardening artifact was present in the CT scans of tube samples, a segment of tube sample was cut and then re-scanned with and without tube.

Figure 78 shows the gray values profile of the same sample, but in different situations. The profile with ID "Sample" corresponds to the sample when extracted from the tube; the ID-profile "Sample-steel tube original" is the profile of the sample into the sampler; finally, the profile with ID "Sample-steel tube post-extraction" is the profile of the extracted sample covered again with steel tube. Based on the analysis of these profiles:

1) The sample is not disturbed during extraction process, because the profiles of the sample with steel tube match before and after
2) There is no beam hardening artifact. Although the profiles show a cupping shape, gray values are not underestimated compared to the extracted sample profile. Instead, one can see an upward shift of the gray values, therefore, there is no darkening.

The steel tube of the sampler acts as a filter, since a filter pre-hardens the X-ray beam. The number of photons at the lower energy levels decreases, resulting in an upward shift in the mean energy of the spectrum. When the mean energy of the spectrum increases, the intensity (gray value) also increases according to Beer's law. One can see that the shift decreases as the beam penetrates into the sample, resulting in a cupping shape, hence the confusion with the beam hardening artifact.

No method to correct this "artifact" in the post-processing of the images has been found in the literature.

The triaxial and oedometer specimens are located in the center of the sample, where the induced gray shift is practically linear. With the aim of quantify this shift, the difference between the average of the gray values of the extracted sample and the sample with steel tube is obtained. ROI of 50mm and 38mm were defined; even though it is practically linear, the shift in the ROI of 38mm is lower. This corrections are later applied to oedometer (50mm) and

triaxial specimens (38 mm) taken from the tubes. Table 14 shows the values used in the correction.
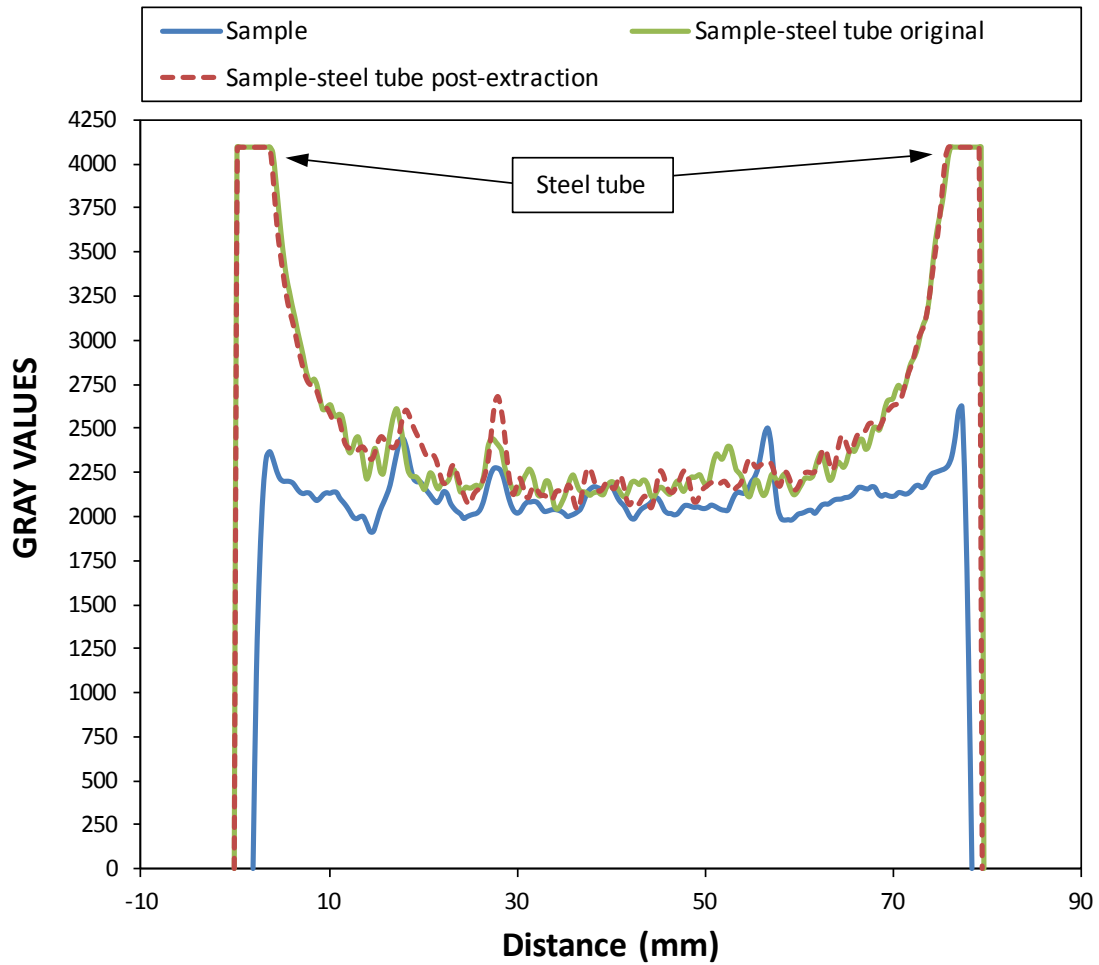
Figure 78. Gray values(intensities) profiles of a sample section with and without steel tube.

Table 14. Values used in the filter "artifact" correction.

ROI diameter (mm)	Correction values
50	118
38	100

6.2.2.5 Partial volume effect

Due to its grain size distribution, it was suspected that specimens retrieved with the small Shelby tube (ϕ_{int} = 83mm) may have suffered from a partial volume artifact.

Otani et al. (2002) studied the influence of grain size on the CT values and therefore in the estimated density (see Figure 19, Section 2.3.7, Chapter II). They found that a partial volume artifact resulted in higher CT values. Figure 79 shows the normalized Otani's graph.

The graphical relation of Otani et al. (2002) is modified before application to our case because voxel dimensions are different. To remove the influence of voxel volume, the grain size axis has been normalized with voxel volume.

To assign a volume to soil grain particle shape is assumed spherical. Since the size of clay is not considered in the study of Otani et al. (2002), the above assumption is adequate.

To represent the specimens from Shelby (ϕ_{int} = 83mm) in the normalized graph, the largest grain size of the soil in the Shelby (ϕ_{int} = 83mm) was used. The grain size used is 2mm.
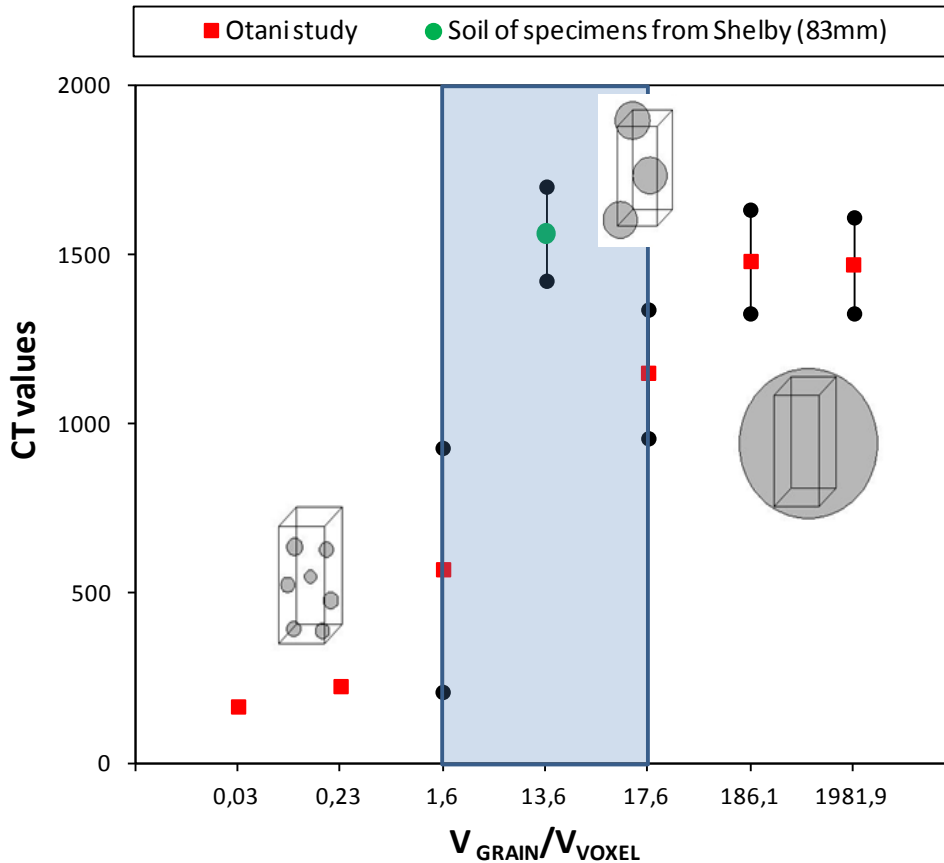
Figure 79. Relationship between CT values and grain volume normalized by voxel volume.

The analysis shows that V_{GRAIN}/V_{VOXEL} ratio of the specimens retrieved from Shelby (ϕ_{int} = 83mm) lies in a zone susceptible to a partial volume artifact. Therefore their wet bulk densities might have been overestimated, and the CT values might reflect more the mineral (grain) density than that of the soil. The effect will not be as drastic as in the study of Otani, since the material filling the space between the larger grains was air (very low CT value) for Otani, whereas it is clay and water in our study (CT values closer to that of the bulk mineral).

Apart from that another factor contributing to the larger CT values observed in our specimens is that the gravels are not likely to be purely quartzitic. The source area of the Muga river is located in Pirineo, therefore the gravels and sand include minerals like hornblende, apatite and epidote (see Sainz-Amor & Julià, 1999). These minerals contain aluminum, magnesium, calcium and iron, which are elements with higher attenuation coefficient than quartz (and hence larger CT values).

6.2.3 ANALYSIS OF CT SCANS FROM FIELD SAMPLES

The analysis of the CT scans from field samples is carried out in several stages. First, histograms of CT values from each specimen are obtained, and compared for the same type of sampler, helped by the visual inspection of some substacks (slices). Second, representative statistics of all the gray values from each specimen are obtained, transformed to CT values from which wet

bulk densities are inferred. Such density values are then compared to previously obtained laboratory data.

The detailed analysis of CT value variability (histograms, etc) is restricted to the specimens obtained from tube samplers. As explained above, CT values from specimens retrieved from the block sample were treated to remove artifacts, and therefore only their mean values are deemed reliable.

6.2.3.1 Histograms of CT values for tube specimens

In order to make a proper comparison, the X-axis scale (CT values) is the same for all histograms.

All histograms of CT values for all specimens are represented in the Figure 80. In what follows they will be studied separately.
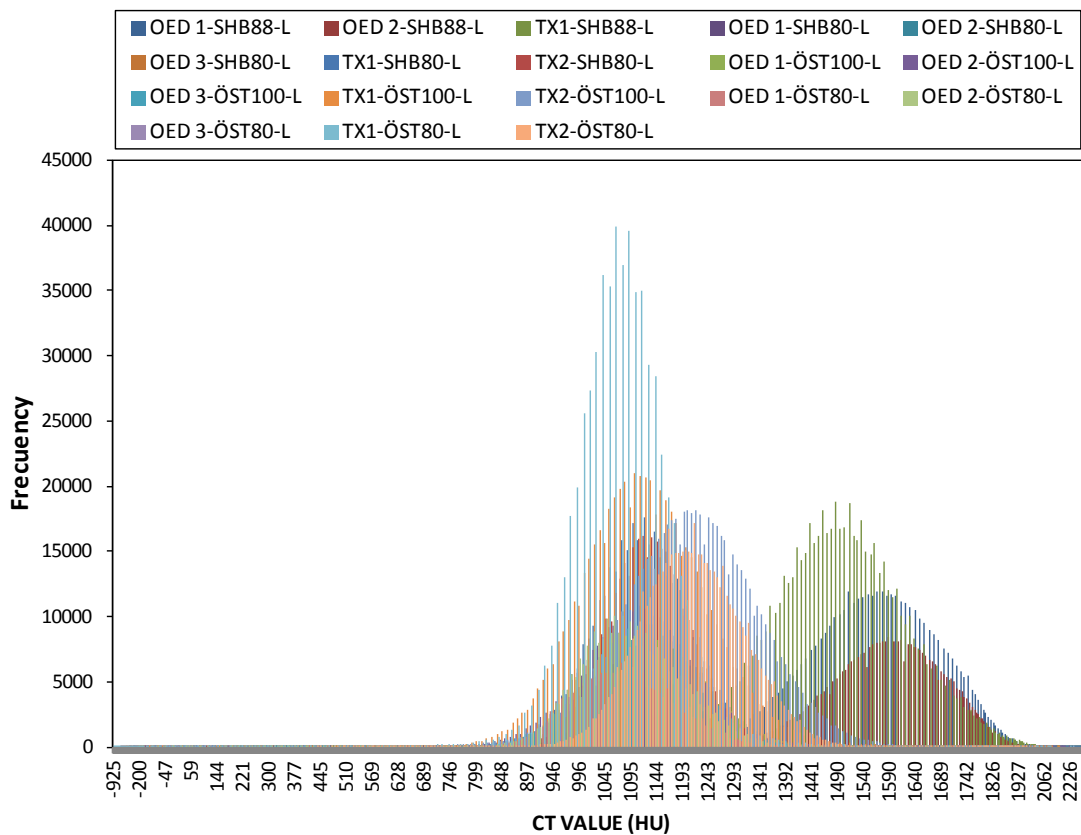
Figure 80. Histograms of all specimens.

♦ **Shelby ($\phi_{int} \approx 83mm$)**

Figure 81 shows histograms of CT values for specimens from Shelby ($\phi_{int} \approx 83mm$). The soil retrieved in this sampler is different from the other samples. The gravel content is larger according to the results of the grain size distribution (see Figure 58). Also, their behavior on both triaxial and oedometers tests is far from that observed in the rest of specimens. Figure 82 shows the presence of gravels.
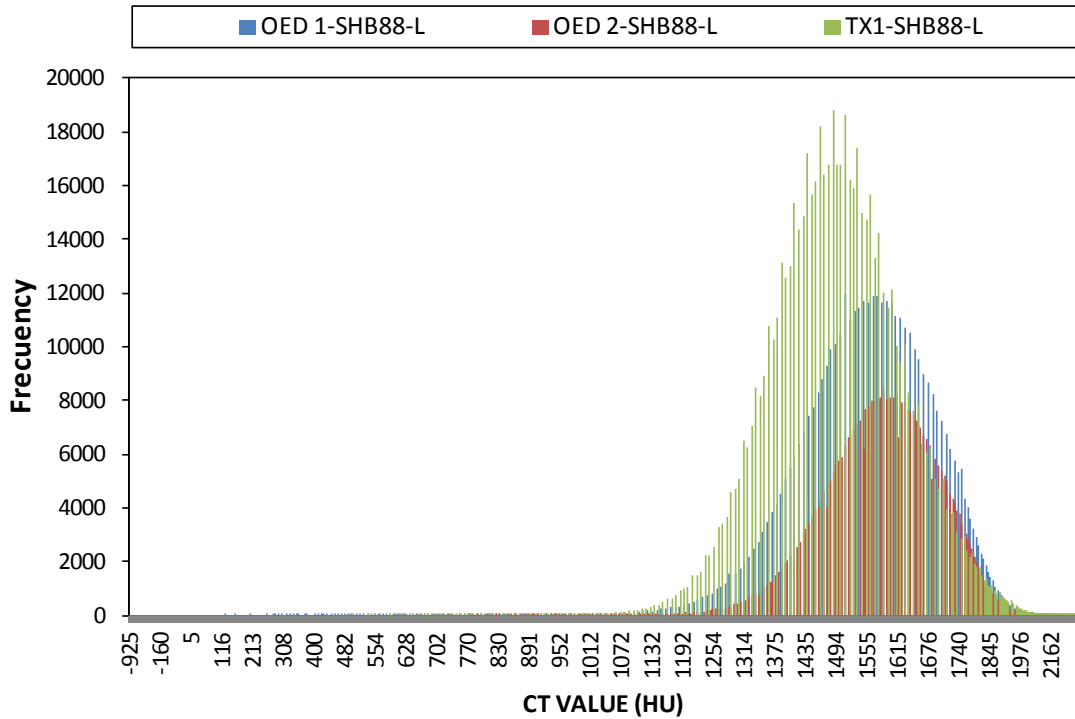
Figure 81. Histograms of CT values for Specimens from Shelby (ϕ_{int}≈83mm).
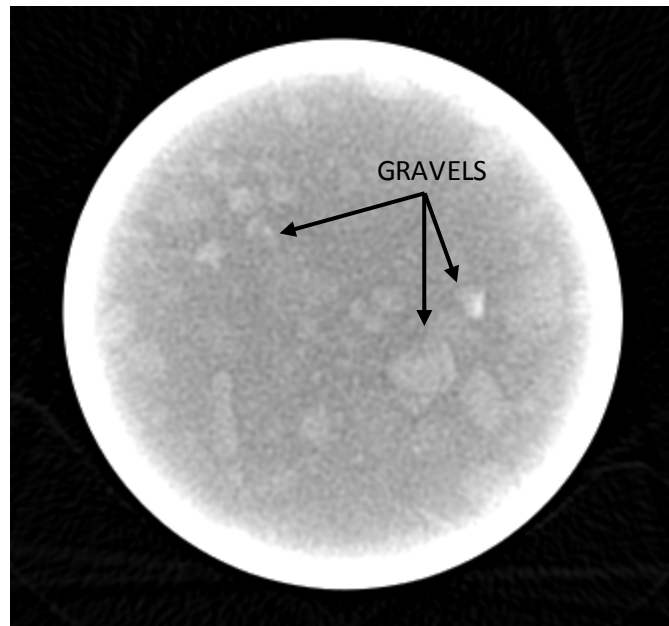
Figure 82. Slice of OED 1-SH88-L specimen.

♦ **Shelby (ϕ_{int}≈76mm)**

Figure 83 shows that the histograms of all specimens are very similar. The most common value is the CT value of 1120 HU (2142 gray value). Quite low values have been recorded, up to -175 HU (see Figure 84), which are located in the cavities of bivalves. These values are lower than the CT value of water (0 HU) and upper than the air CT value (-1000 HU). These values may be the result of averaging between the water molecules and air. In fact, during specimen preparation for testing the bivalves cavities appeared partially filled with water.
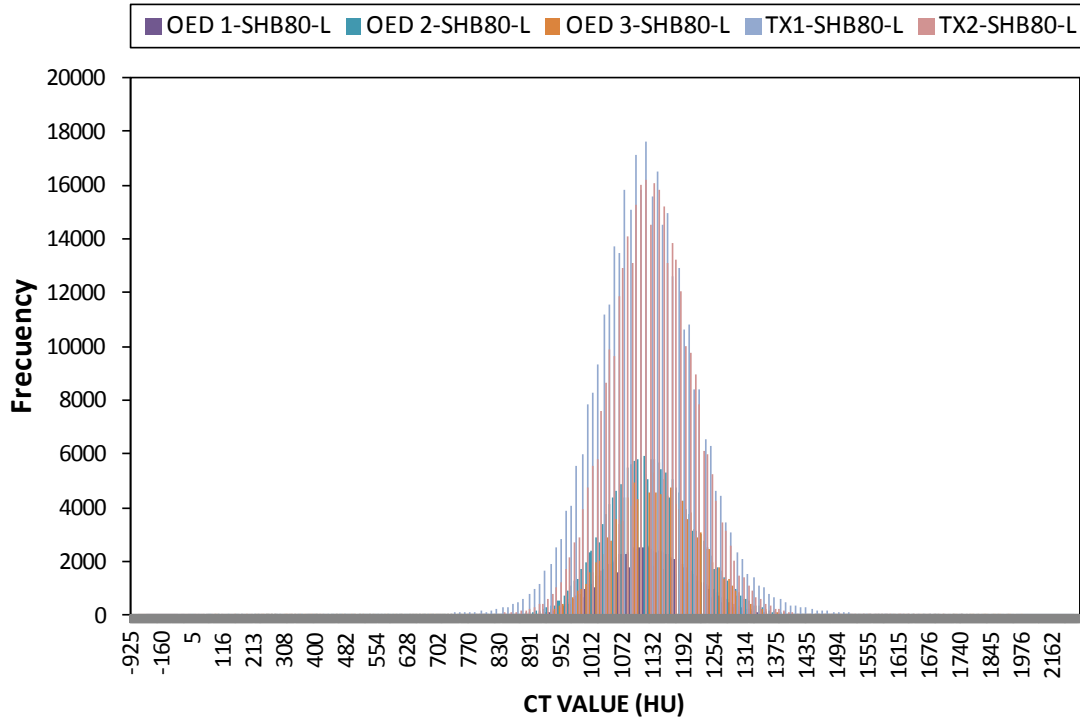
Figure 83. Histograms of CT values for Specimens from Shelby ($\phi_{int} \approx 76mm$).
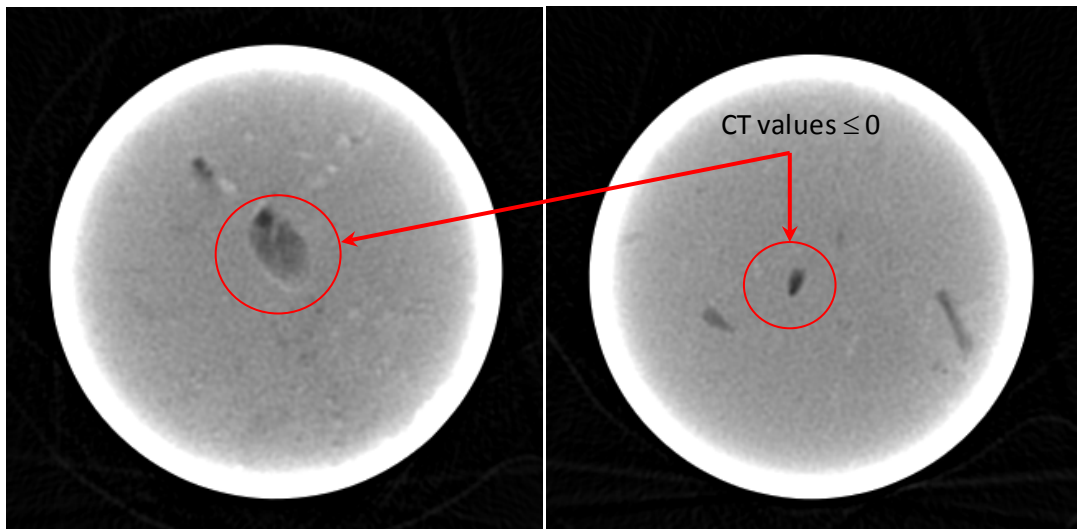
Figure 84. Left: Slice of TX 1-SH80-L; Right: Slice of TX 2-SH80-L.

♦ **Österberg ($\phi_{int} \approx 95mm$)**

Figure 85 shows histograms of each specimen. Except one (TX2-ÖST100-L), the rest are very similar. The histogram of the specimen TX2-ÖST100-L is shifted to the right, indicating a denser material. Its most common value is 1200 HU (2142 gray value). The most common value of the rest of the specimens is the CT value of 1092-1128 HU (2116 -2152 gray value).

During visual inspection of slices from TX2-L-ÖST100, no anomalies that could explain this shift were detected. In the remaining samples, some small anomalies that increase standard deviation (see Figure 86), such as bivalves (calcium carbonate) and partially water filled fractures, were detected.
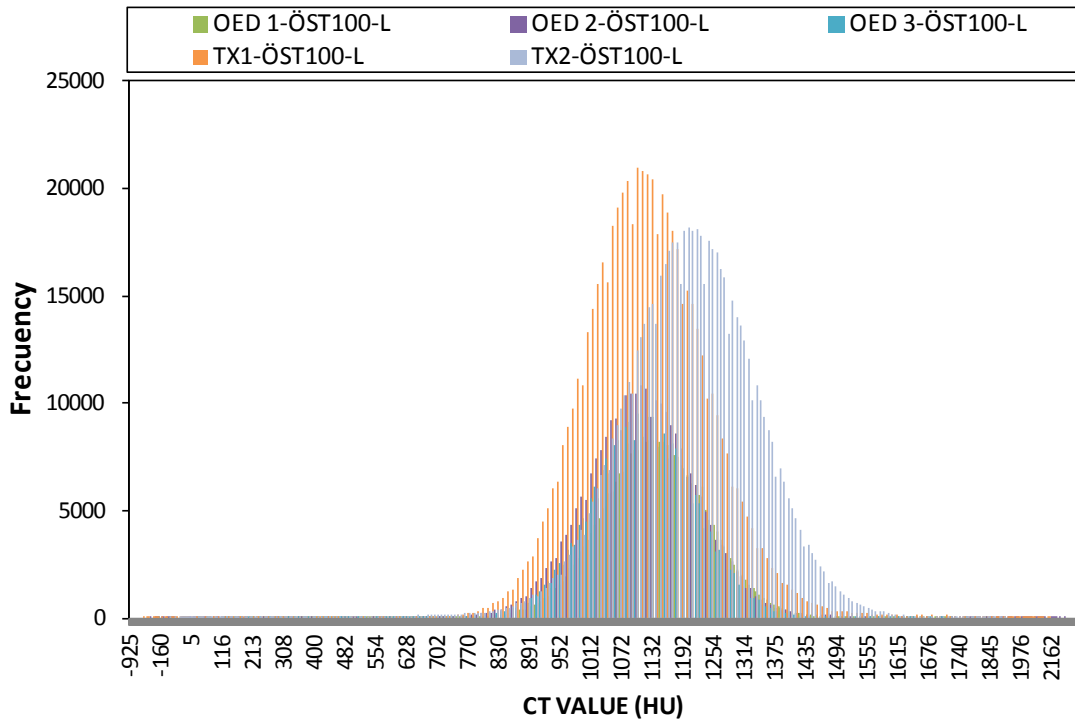
Figure 85. Histograms of CT values for Specimens from Österberg ($\phi_{int}\approx95mm$).
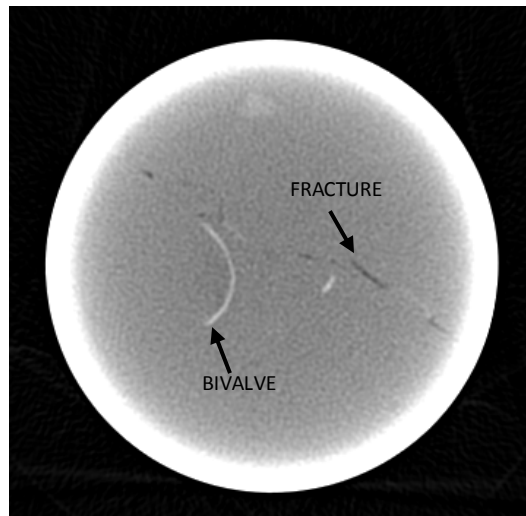
Figure 86. Slice of OED 2- ÖST100-L.

♦   **Österberg ($\phi_{int}\approx76mm$)**

In Figure 87 the histograms for all specimens are represented. Except one (TX2-ÖST80-L), the rest are very similar. The histogram of the specimen TX2-ÖST80-L is slightly shifted to the right, indicating a denser material. Its most common value is 1206 HU (2230 gray value). The most common value of the rest of the specimens is the CT value of 1081-1096 HU (2105 -2120 gray value).

During visual inspection, fractures on the entire length of the tube sample were detected (see Figure 88), sometimes filled with water (CT value of 0) and sometimes with air (CT value of - 1000). In the slices of TX2-L-ÖST80 no anomalies that obviously explain its higher CT values were detected. In contrast, in the rest of specimens, occasional fragments of bivalves and gravels or fragments of bivalves (the CT values are quite similar) were detected.
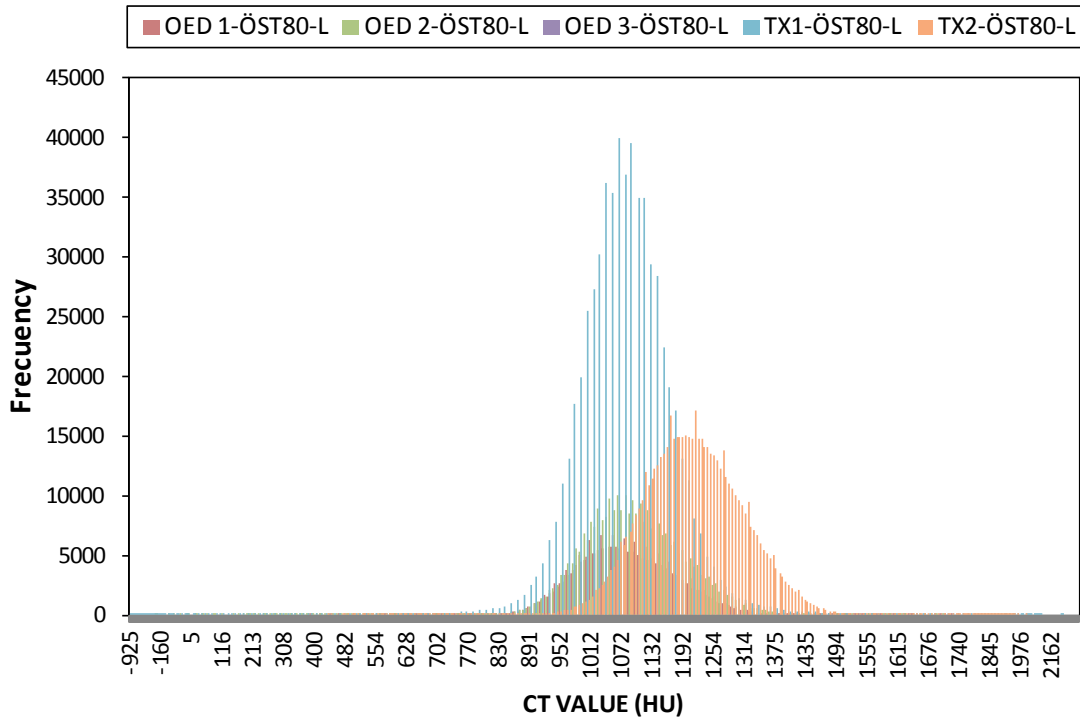
Figure 87. Histograms of CT values for Specimens from Österberg ($\phi_{int}{\approx}76mm$).
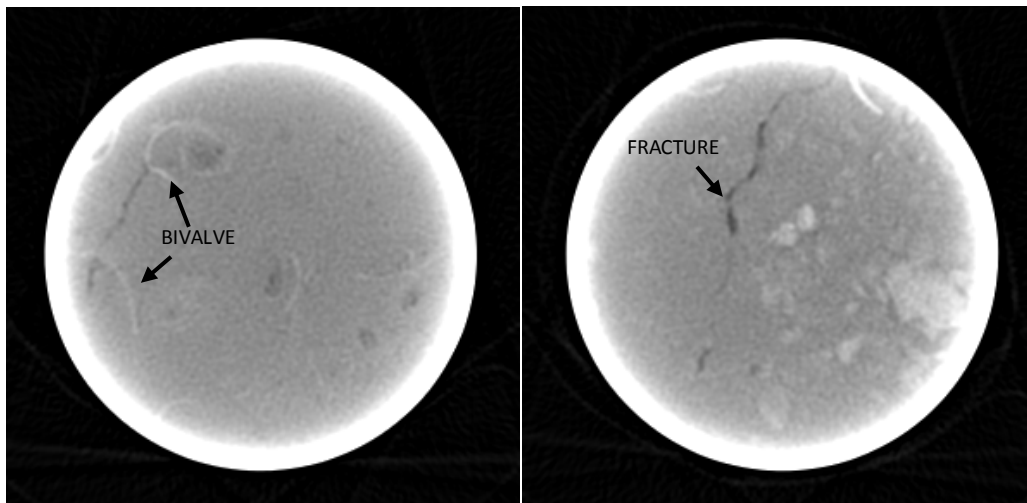
Figure 88. Left: Slice of OED 3-ÖST80-L; Right: Slice of TX 1-ÖST80-L.

6.2.3.2   Wet bulk density values

The average CT value is the result of the average of the values of all voxels in specified region (ROI). The program determines the average and the standard deviation ($\sigma_{CT\,value}$) in the ROI of each slice, and finally calculates the average of all slices.

A Triaxial ROI had about 105909 voxels and an oedometer ROI about 181853 voxels.

Once these mean values are obtained, the wet bulk density is determined from the calibration curve. Table 15 summarizes the statistical results from all specimens.

Table 15. Statistical results from all specimens.

ID Sampler	ID Specimen	Mean of CT value (HU)	$\sigma_{CT\,value}$ (HU)
Shelby (ϕint=83mm)	TX1-SHB88-L	1513.0	142.0
	OED1-SHB88-L	1574.7	144.1
	OED2-SHB88-L	1600.5	125.0
Shelby (ϕint=76mm)	TX1-SHB80-L	1122.3	111.1
	TX2-SHB80-L	1131.5	88.2
	OED1-SHB80-L	1127.2	88.6
	OED2-SHB80-L	1129.8	88.9
	OED3-SHB80-L	1142.8	88.1
Österberg (ϕint=95mm)	TX1-ÖST100-L	1125.3	117.8
	OED1-ÖST100-L	1137.8	109.3
	OED2-ÖST100-L	1116.5	122.8
	OED3-ÖST100-L	1115.5	108.7
Österberg (ϕint=76mm)	TX1-ÖST80-L	1076.9	98.3
	TX2-ÖST80-L	1205.6	83.2
	OED1-ÖST80-L	1084.5	99.5
	OED2-ÖST80-L	1098.0	104.5
	OED3-ÖST80-L	1115.8	107.7
Sherbrooke	TX1-MA-SHK6-L	1226.1	255.8
	TX2-MB-SHK6-L	1157.4	264.0
	TX3-MC-SHK6-L	1188.1	304.1
	OED1-SHK6-L	1151.1	324.8
	OED 2-SHK6-L	1160.7	318.4
	OED 3-SHK6-L	1221.8	280.2

Table 16 shows the wet bulk density obtained from the analysis of CT scans and laboratory data, and their ratio. Figure 89 shows the values of wet bulk density ratio. In brought terms, results of both methods are very similar. As expected, the $\rho_{wet\,bulk}$ CT of the Shelby samples (ϕint=83mm) is greater than the $\rho_{wet\,bulk}$ LAB. This is due to the partial volumen artifact described before. Specimens from the Österberg sample (ϕint=76mm) shows large variability in this ratio than the rest; specimens from the Sherbrooke sample very little.

Table 16. Wet bulk density from CT scan and Laboratory data.

ID Sampler	ID Specimen	$\rho_{wet\,bulk}$ CT (Mg/cm^3)	$\rho_{wet\,bulk}$ LAB (Mg/cm^3)	$\rho_{wet\,bulk}$ CT/$\rho_{wet\,bulk}$ LAB (-)
Shelby (ϕint=83mm)	TX1-SHB88-L	2.53	2.05	1.23
	OED1-SHB88-L	2.65	2.12	1.25
	OED2-SHB88-L	2.70	2.11	1.28
Shelby (ϕint=76mm)	TX1-SHB80-L	1.77	1.78	0.99
	TX2-SHB80-L	1.78	1.82	0.98

ID Sampler	ID Specimen	$\rho_{\text{wet bulk}}$ CT (Mg/cm^3)	$\rho_{\text{wet bulk}}$ LAB (Mg/cm^3)	$\rho_{\text{wet bulk}}$ CT/$\rho_{\text{wet bulk}}$ LAB (-)
	OED1-SHB80-L	1.78	1.79	0.99
	OED2-SHB80-L	1.78	1.77	1.01
	OED3-SHB80-L	1.81	1.75	1.03
Österberg (ϕint=95mm)	TX1-ÖST100-L	1.77	1.74	1.02
	OED1-ÖST100-L	1.80	1.75	1.03
	OED2-ÖST100-L	1.76	1.74	1.01
	OED3-ÖST100-L	1.75	1.76	0.99
Österberg (ϕint=76mm)	TX1-ÖST80-L	1.68	1.87	0.90
	TX2-ÖST80-L	1.93	1.76	1.10
	OED1-ÖST80-L	1.69	1.79	0.94
	OED2-ÖST80-L	1.72	1.72	1.00
	OED3-ÖST80-L	1.75	1.71	1.02
Sherbrooke	TX1-MA-SHK6-L	1.97	1.98	0.99
	TX2-MB-SHK6-L	1.84	1.85	0.99
	TX3-MC-SHK6-L	1.90	1.93	0.98
	OED1-SHK6-L	1.82	1.82	1.00
	OED 2-SHK6-L	1.84	1.87	0.98
	OED 3-SHK6-L	1.96	1.95	1.01
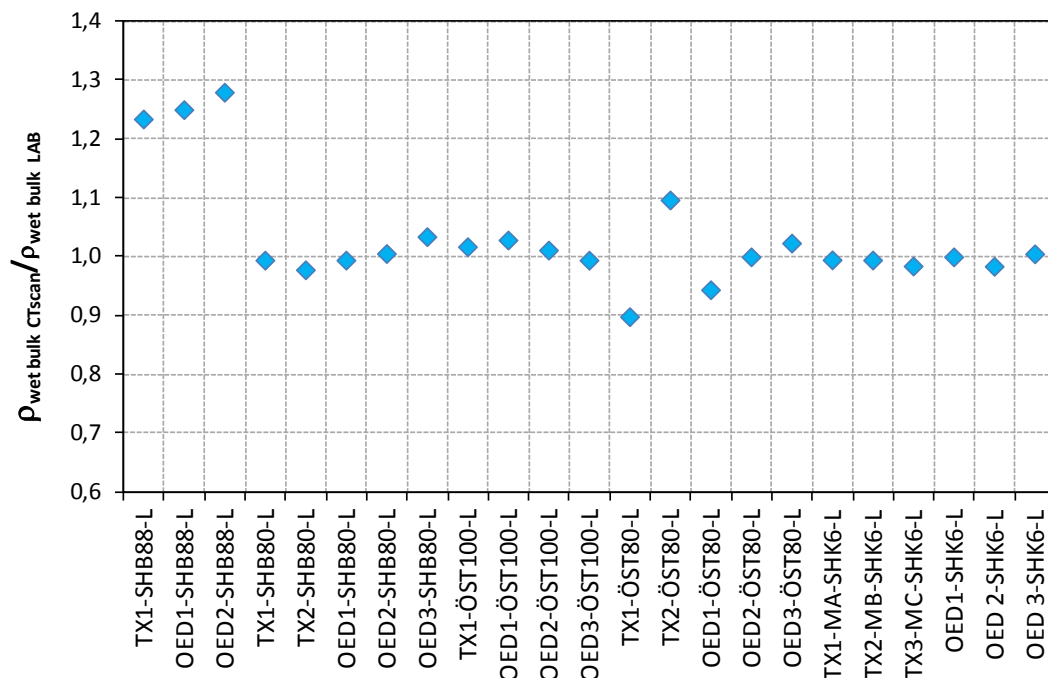
Figure 89. Wet bulk density ratio.

In Figure 90, the wet bulk density measured in the laboratory is shown paired with the mean CT value of the corresponding specimen, on top of the CT calibration line and the 95% confidence intervals. It seems that the laboratory results from most 76 mm Osterberg

specimens are significantly different from what the CT predicts. The most likely cause for the difference is some error in the laboratory determinations for these specimens, because the other data firmly support the correlation.
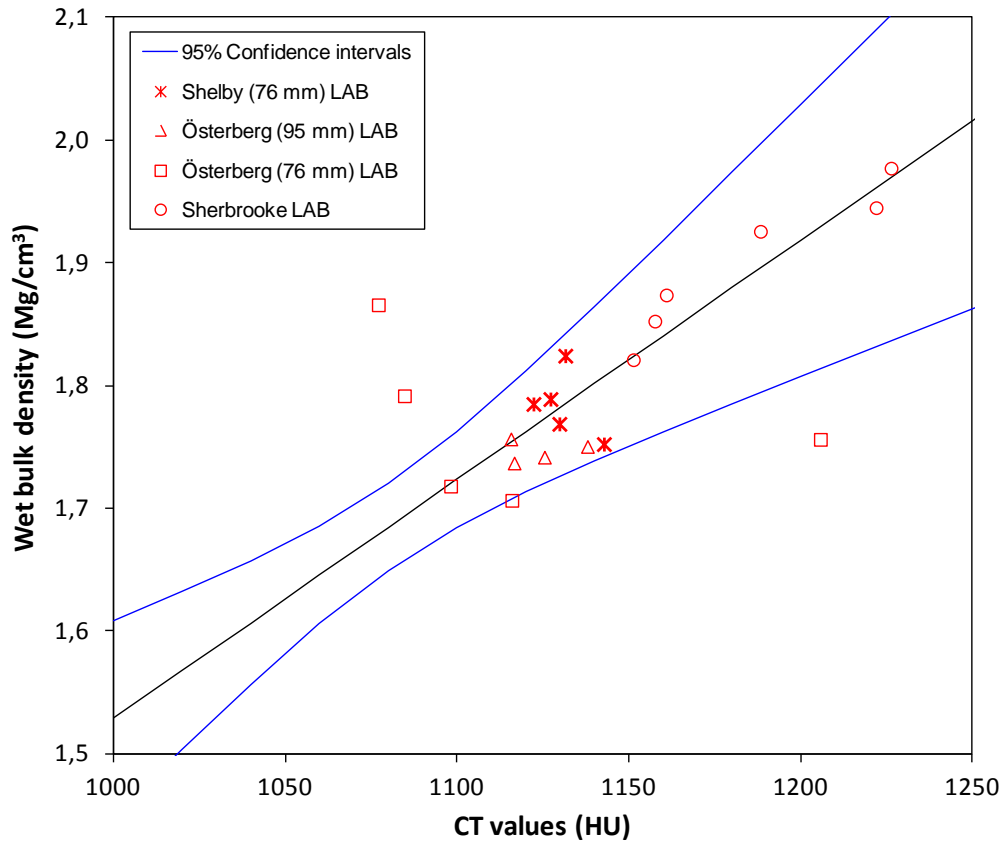
Figure 90. Wet bulk density from CT scans and laboratory data.

6.2.3.3   Block and tube density profiles.

The block sample is considered as that one more closely related to the material 'in situ', because the sampling method is less disruptive. Therefore the density values measured in the block should be used as reference for the rest.

Although the Sherbrooke specimens had very similar density values from CT and laboratory data, both indicate a significant heterogeneity. As the CT scan of the block sample shows a lot of noise, the wet bulk density profile along the sample cannot be obtained. However the mean values of the specimens of the upper (TX2-MB-SHK6-L, TX3-MC-SHK6-L, OED1-SHK6-L and OED 2-SHK6-L) and the lower (TX1-MA-SHK6-L and OED 3-SHK6-L) piece are computed in order to obtain a representative profile. The mean values are in the Table 17.

Table 17. Representative wet bulk density of block sample.

Piece	Mean $\rho_{\text{wet bulk}}$ CT (Mg/cm^3)
Upper	1.85
Lower	1.96

La Figure 91 shows the representative wet bulk density profile in the block sample (sherbrooke).
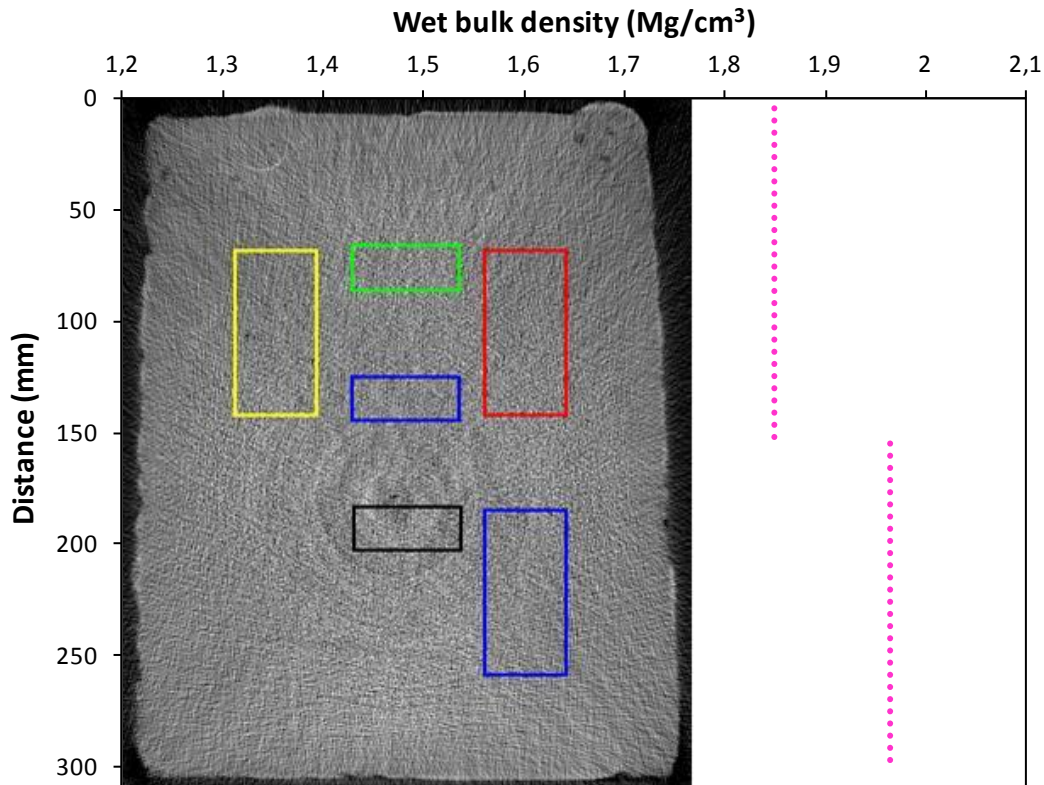
Figure 91. Wet bulk density profile of the block sample.

Density profiles along the length of the different tube samplers were obtained. Figure 93 and Figure 93 show the wet bulk density profiles obtained by means of a circular ROI (ϕ = 50mm) coaxial with the tube sampler. Also shown wet bulk densities from laboratory data and the representative profile from block sample.

The ROI diameter was chosen to maximize the data while making sure that no gray value altered by the steel tube was included. Figure 94 and Figure 95 show the 3D surface plot of the same slice of ROI with diameters of 70mm and 50mm, respectively. The effect of the steel boundary on the larger sized ROI section is evident.

The recovery of Shelby sampler (ϕ_{int} = 83mm) was about 50%, and the soil is different from the rest of the samples; the profile is relatively homogeneous but the larger values are not related to the Sherbrooke sample.

Regarding the rest of profiles following features are observed:

- All the tube samples indicate smaller densities that the reference profile in the overlapping area.
- There is generally better agreement in the upper part of the tubes
- The profile of the Shelby (ϕ_{int} = 76mm) is more homogeneous that of the Österberg samplers, which both show a large increase in soil density close to the bottom
- Some irregularities in the tube density profiles are clearly associated with local heterogeneities: e.g. a level of gravels close to TX1 in both Österberg tubes shows as a peak in CT density. Also the lower density in the small (ϕ_{int} = 76mm) Österberg can be ralted to fractures within the sample. This heterogeneities are shown in Figure 96 and Figure 97.
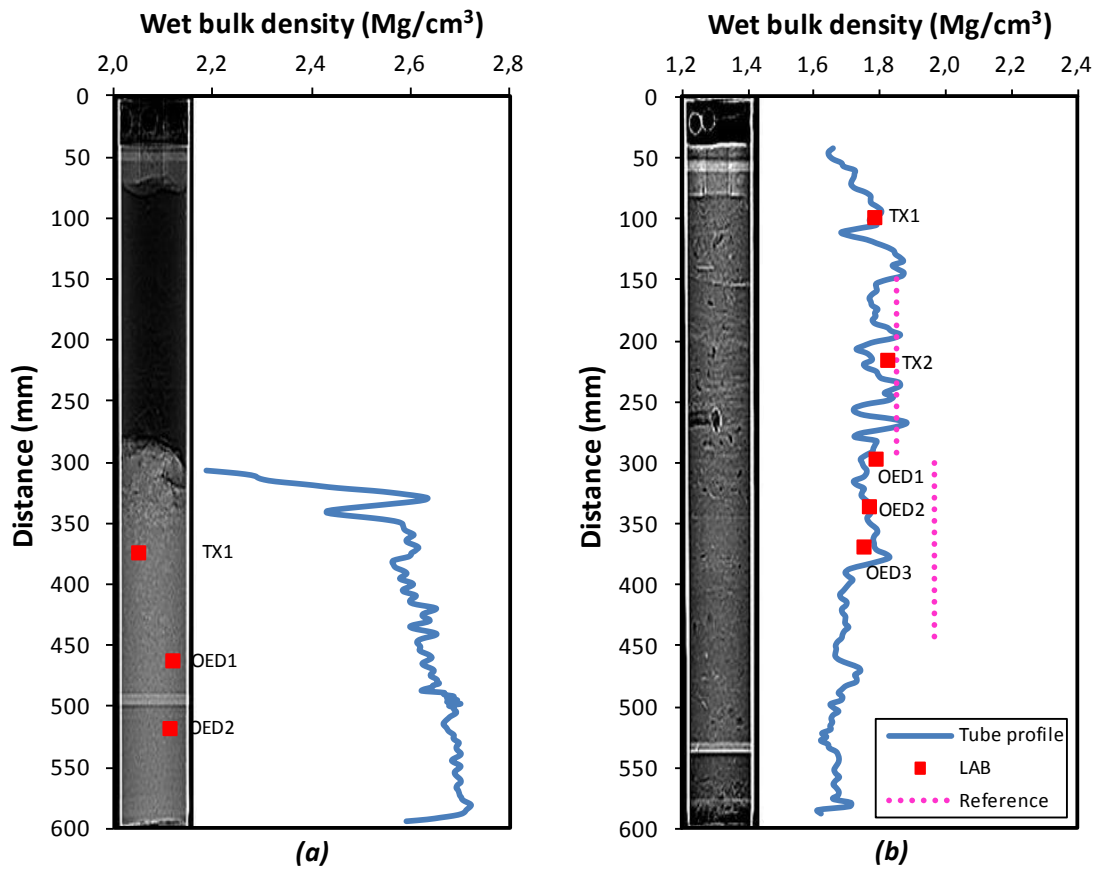
Figure 92. Wet bulk density profiles. (a) Shelby (ϕint=83mm); (b) Shelby (ϕint=76mm).
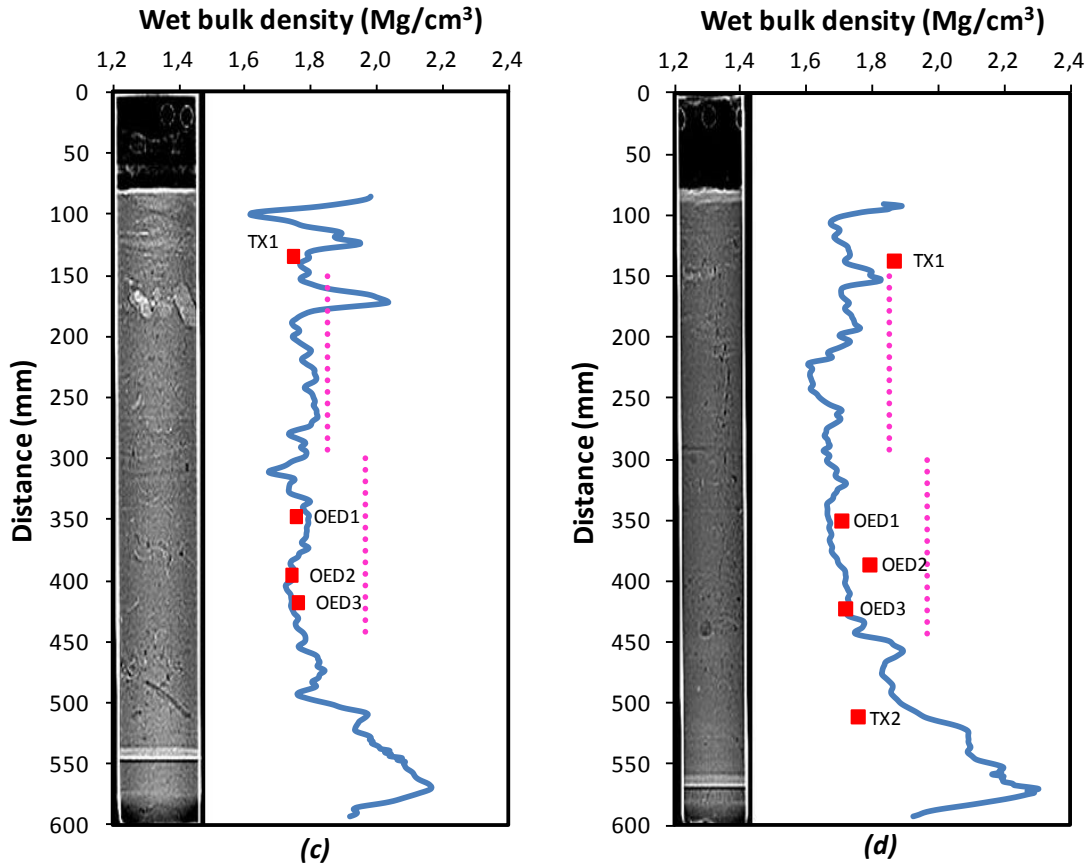
Figure 93. Wet bulk density profiles. (c) Österberg (ϕint=95mm); (d) Österberg (ϕint=76mm).
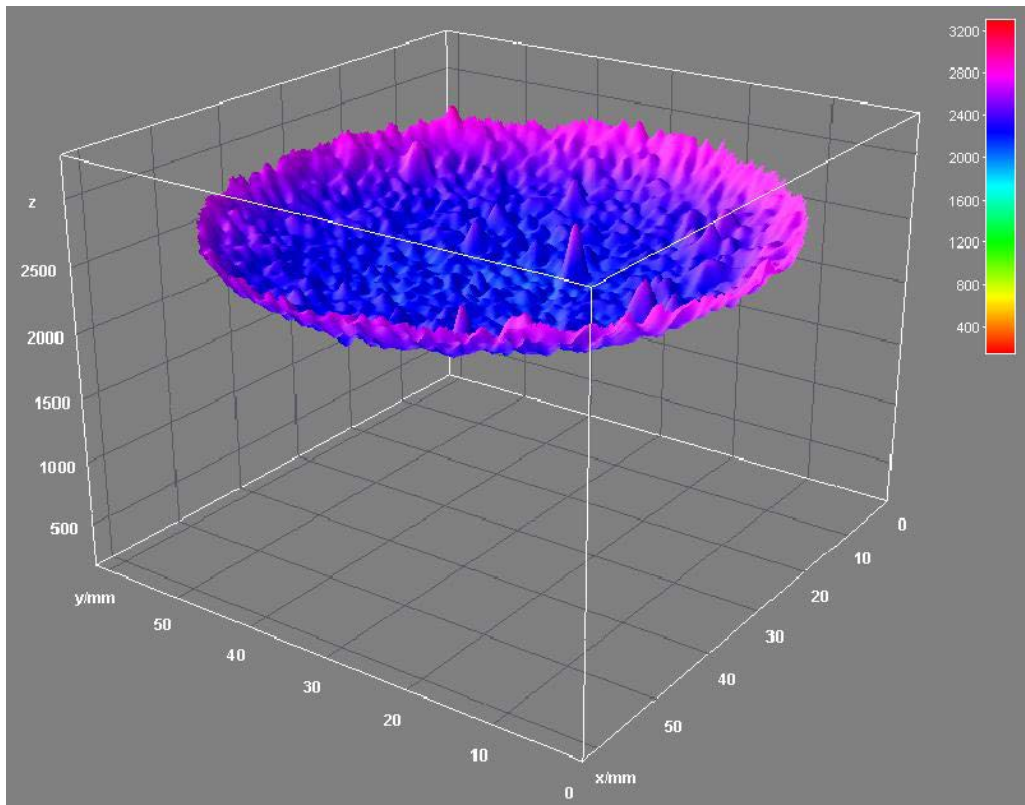
Figure 94. 3D surface plot of circular ROI with diameter of 70mm.
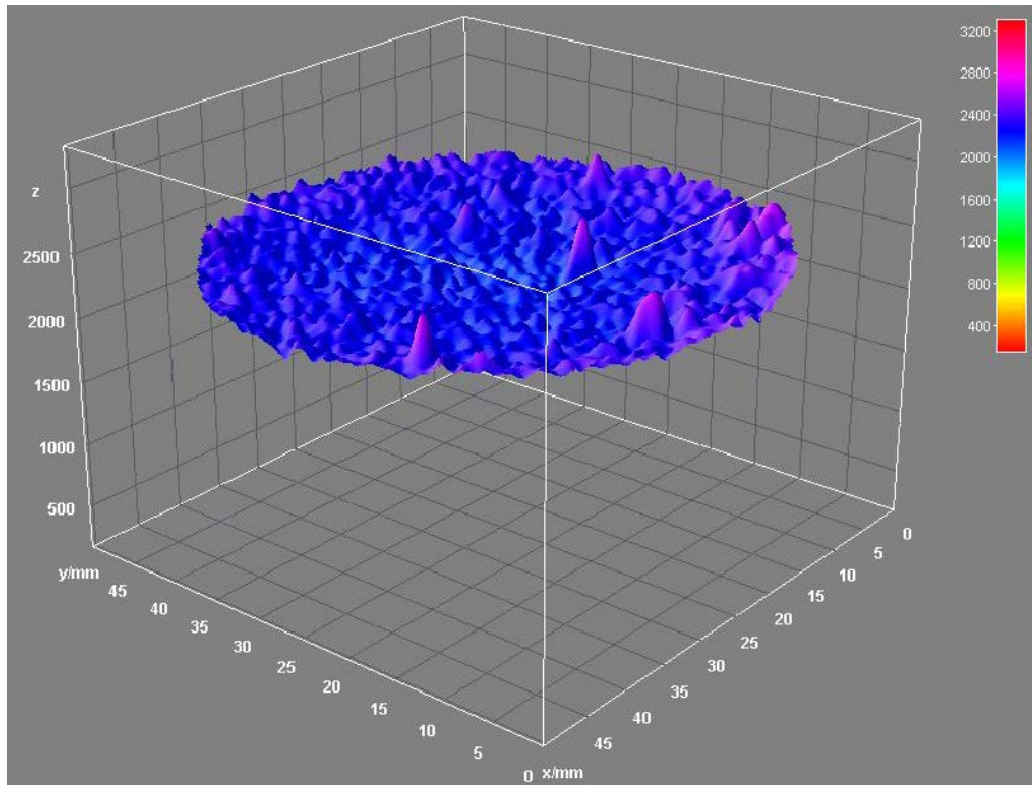
Figure 95. 3D surface plot of circular ROI with diameter of 50mm.

SLICE 1
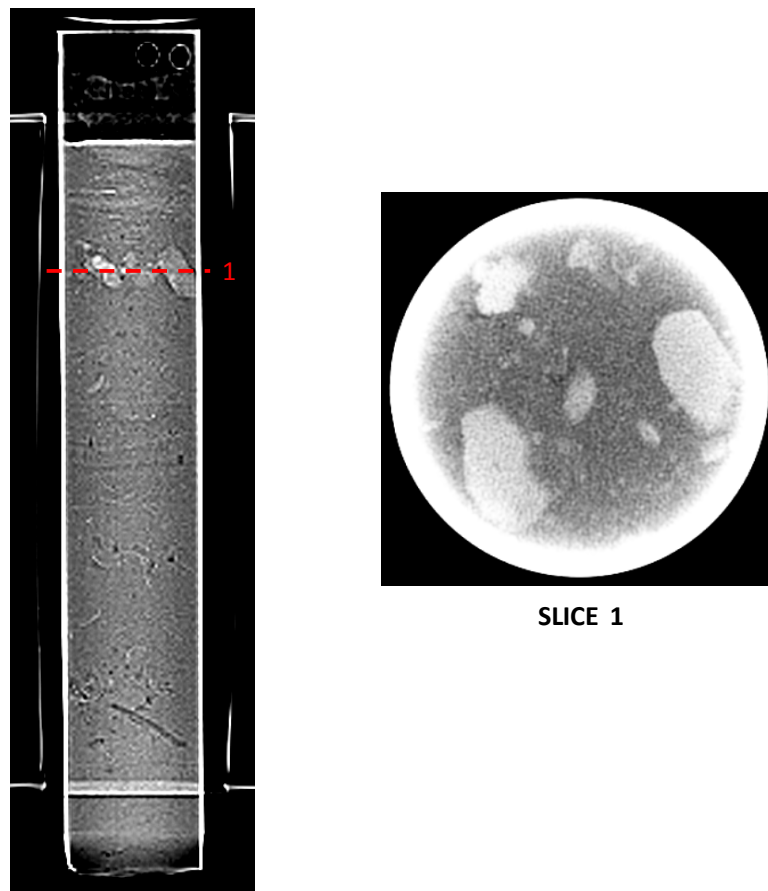
Figure 96. Heterogeneity in the Österberg (ϕ_{int} = 76mm).
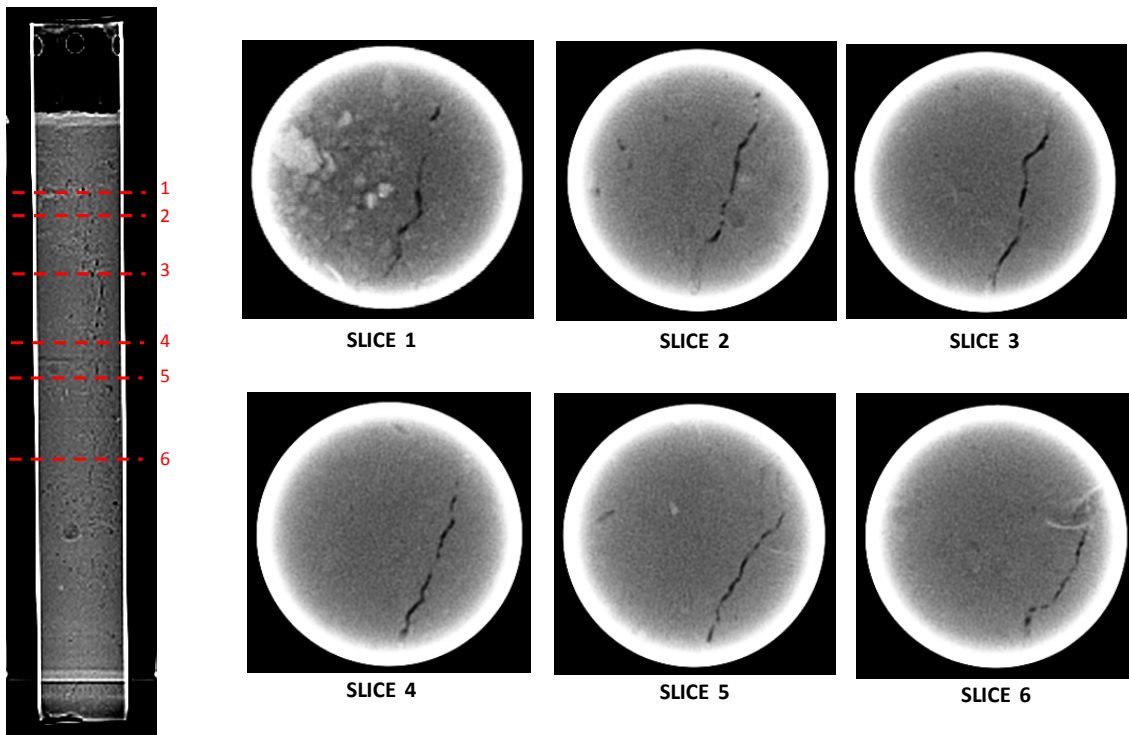
Figure 97. Heterogeneities in the Österberg (ϕ_{int} = 76mm)

Chapter VII. SAMPLE DISTURBANCE ASSESSMENT

Soil sample disturbance can occur during drilling, during sampling, during transportation and storage, or during preparation for testing. Any sample of soil being taken from the ground, transferred to the laboratory, and prepared for testing will be subject to disturbance. According to Clayton et al. (2005) The mechanisms associated with this disturbance can be classified as follows:

(i)   Changes in stress conditions.
(ii)   Imposed deformation.
(iii)   Changes in water content.
(iv)   Chemical changes.

Changes in stress conditions take the form of the reduction of the total horizontal and vertical stresses from their *in situ* value, to zero, on the laboratory bench. Mechanical deformations are shear distortions applied to the soil sample, for example by tube sampling. Changes in water content can occur as an overall swelling or consolidation of the soil sample, or a redistribution of moisture in response to pore- pressure gradients. Chemical changes may occur in the pore water or the soil, and may result from contact with drilling fluid or with sampling tubes.

These mechanisms can occur at different stages during the process of geotechnical investigation, and while some occur very quickly, others take considerable time. Some types of disturbance are unavoidable, but many can be minimized or even eliminated if the mechanisms of disturbance are understood and common sense is used to optimize the processes involved. The importance of a particular type of disturbance will depend not only upon the sampling processes being used, but also upon the type of soil being sampled. However, the unifying factors are that sampling disturbance affects the effective stress state of a soil sample, and in addition (and more seriously) can also affect its structural bonding.

Table 18 gives a list of the main causes of disturbance at various stages of a site investigation.

Table 18. Principal causes of soil disturbance. Extracted from Clayton et al. (2005)

Before sampling	During sampling	After sampling
Stress relief	Stress relief	Stress relief
Swelling	Remoulding	Migration of water within the sample
Compaction	Displacement	Loss of moisture
Displacement	Shattering	Freezing
Base heave	Stones at the cutting shoe	Overheating
Piping	Mixing or segregation	Vibration
Caving	Failure to recover	Chemical changes
		Disturbance during extrusion

7.1 OBSERVED VOID RATIO CHANGES

In the present work, different values of the void ratio have been obtained for all testing specimens at different stages during the sampling process. These values are indicative of the hydraulic and mechanic processes that take place since sampling started until the reconsolidation back to in situ stresses.

In CT scan analysis, the wet bulk density ($\rho_{wet\ bulk}$) values for each specimen have been obtained. Assuming that the soil is saturated, the void ratio is obtained from:

$$e = \frac{\gamma_s - \rho_{wet\ bulk}}{\rho_{wet\ bulk} - \gamma_w}$$

Equation 15

Where γs is the specific weight of solid particles and γw is the specific weight of water.

The CT void ratio obtained for block and tube specimens is not representative of the same situation, as block and tube samples are not in the same state and have not suffered the same sampling process. Regardless of the possible effects of different storage procedures the most obvious differences are (a) total stress-relief in tube samples is not complete, as there is still a radial stress related to the steel tube confining (b) block sampling avoids tube induced shear distortions.

Because total stress relief is partly compensated by surface suction, shear distortion is considered a relatively major cause of disturbance in fine soils such as this. Therefore the void ratio of the block samples is considered closer to that of the soil "in situ" and defined as the reference value (e_{00}). The average void ratio of all specimens from the block sample (0.92) is considered the reference value for tube specimens.

Table 19 summarizes the values of void ratio obtained from CT scans analysis (e_{00} and e_{01}), measured at specimen retrieval (e_{02}), measured at the end of saturation stage (e_{03}) and finally that measured when the specimen recovered the in situ effective stress level (e_{04}).

Triaxial equipment of the Geotechnical laboratory of UPC does not have an external LVDT, thus the void ratio at the end of the saturation stage could not be measured. For these specimens, it is assume: the void ratio measured at the end of the saturation is equal to void ratio measured during specimen retrieval.

Table 19. Void ratio values from differents states.

Type of Sampler	ID specimen	e_{00}	e_{01}	e_{02}	e_{03}	e_{04}
Sherbrooke	TX1-MA-SHK6-L	0.73	-	0.72	0.72	0.67
	TX2-MB-SHK6-L	1.01	-	0.94	0.92	0.87
	TX3-MC-SHK6-L	0.88	-	0.83	0.82	0.78
	EDO1-SHK6-L	1.00	-	0.97	0.97	0.89
	EDO2-SHK6-L	0.98	-	0.88	0.87	0.82
	EDO3-SHK6-L	0.74	-	0.75	0.74	0.70
Shelby (ϕ_{int}=76mm)	TX1-SHB80-L	*0.92*	1.13	1.11	*1.11*	0.96
	TX2-SHB80-L	*0.92*	1.08	1.01	*1.01*	0.87
	EDO1-SHB80-L	*0.92*	1.10	1.07	1.07	1.00
	EDO2-SHB80-L	*0.92*	1.09	1.09	1.09	1.03
	EDO3-SHB80-L	*0.92*	1.02	1.14	1.14	1.08

Type of Sampler	ID specimen	e_{00}	e_{01}	e_{02}	e_{03}	e_{04}
Österberg (ϕ_{int} =95mm)	TX1-ÖST100-L	*0.92*	1.11	1.20	*1.20*	1.05
	EDO1-ÖST100-L	*0.92*	1.04	1.17	1.16	1.07
	EDO2-ÖST100-L	*0.92*	1.16	1.22	1.22	1.16
	EDO3-ÖST100-L	*0.92*	1.16	1.20	1.19	1.12
Österberg (ϕ_{int} =76mm)	TX1-ÖST80-L	*0.92*	1.43	0.92	*0.92*	0.84
	TX2-ÖST80-L	*0.92*	0.75	1.15	*1.15*	1.01
	EDO1-ÖST80-L	*0.92*	1.35	1.11	1.10	1.01
	EDO2-ÖST80-L	*0.92*	1.27	1.25	1.25	1.16
	EDO3-ÖST80-L	*0.92*	1.16	1.28	1.27	1.19

Where,

e_{00} : Reference void ratio

e_{01} : Void ratio obtained from CT scans.

e_{02} : Void ratio measured at specimen retrieval.

e_{03} : Void ratio measured at the end of saturation stage.

e_{04} : Void ratio measured at the in situ stress during consolidation stage.

Table 20 shows various void ratio variations. Each of them represents a sample state change, namely

- Δe_{02} : Void ratio variation from reference value to specimen retrieval.
- Δe_{03} : Void ratio variation from reference value to end of saturation stage.
- Δe_{14} : Void ratio variation from CT scan to in situ stresses.
- Δe_{24} : Void ratio variation from specimen retrieval to in situ stresses.
- Δe_{34} : Void ratio variation from end of saturation stage to in situ stresses.

Independently of the mechanical causes one interesting observation is that the variation of void ratio noted before starting testing at the lab is frequently larger than that due to reconsolidation to in situ stresses.

Table 20. Void ratio variation

Type of Sampler	ID specimen	Δe_{02}	Δe_{03}	Δe_{14}	Δe_{24}	Δe_{34}
Sherbrooke	TX1-MA-SHK6-L	0.02	0.02	0.06	0.04	0.04
	TX2-MB-SHK6-L	0.07	0.09	0.15	0.07	0.06
	TX3-MC-SHK6-L	0.05	0.05	0.10	0.05	0.04
	EDO1-SHK6-L	0.04	0.04	0.11	0.07	0.07
	EDO2-SHK6-L	0.11	0.11	0.17	0.06	0.06
	EDO3-SHK6-L	-0.01	-0.003	0.04	0.05	0.05
Shelby (ϕ_{int}=76mm)	TX1-SHB80-L	-0.19	-0.19	0.17	0.15	0.15
	TX2-SHB80-L	-0.09	-0.09	0.20	0.13	0.13
	EDO1-SHB80-L	-0.15	-0.15	0.10	0.07	0.07
	EDO2-SHB80-L	-0.17	-0.17	0.06	0.06	0.06
	EDO3-SHB80-L	-0.22	-0.22	-0.06	0.06	0.06

Type of Sampler	ID specimen	Δe_{02}	Δe_{03}	Δe_{14}	Δe_{24}	Δe_{34}
Österberg (ϕ_{int} =95mm)	TX1-ÖST100-L	-0.28	-0.28	0.06	0.14	0.14
	EDO1-ÖST100-L	-0.25	-0.24	-0.02	0.10	0.10
	EDO2-ÖST100-L	-0.30	-0.30	0.00	0.07	0.06
	EDO3-ÖST100-L	-0.28	-0.27	0.04	0.08	0.07
Österberg (ϕ_{int} =76mm)	TX1-ÖST80-L	0.002	0.002	0.59	0.08	0.08
	TX2-ÖST80-L	-0.23	-0.23	-0.25	0.14	0.14
	EDO1-ÖST80-L	-0.19	-0.18	0.34	0.10	0.09
	EDO2-ÖST80-L	-0.33	-0.33	0.11	0.09	0.09
	EDO3-ÖST80-L	-0.36	-0.35	-0.03	0.09	0.08

7.2 SAMPLE DISTURBANCE CRITERIA

Many techniques are available for the assessment of sample quality. These include measurements of initial suction in the sample, comparison of shear wave velocity measured on the specimen with that obtained in situ and the assessment of the stress/strain curves and parameters measured in oedometer or triaxial tests. In this study only the last technique is evaluated, because this is the best established.

7.2.1 ANDRESEN & KOLSTAD (1979)

Andresen & Kolstad (1979) evaluated the quality of Norwegian soft clay samples obtained with NGI 54-mm piston sampler. They argued that the volumetric strain, ε_{v0}, induced when consolidating a sample back to the best estimate of in situ stresses was a useful indicator of sample quality. They presumed that for a high quality sample ε_{v0} should be close to zero. Table 21 shows the sample disturbance criterion proposed by Andresen & Kolstad (1979).

Table 21. Sample disturbance criterion proposed by Andresen & Kolstad (1979).

ε_{v0}	Test specimen quality
< 1%	Very good to excellent
1 -2 %	Good
2 – 4 %	Fair
4 -10 %	Poor
> 10 %	Very poor

7.2.2 LUNNE ET AL.(1997)

Lunne et al (1997) evaluated the sample disturbance effects in soft low plasticity Norwegian clay. For this, they conducted laboratory testing (CAUC triaxial and CRS oedometer tests) in specimens retrieved with different samplers, like Sherbrooke block sampler and standard piston sampler. Laboratory results clearly showed the superior quality of the block samples compared to the piston samples. Moreover, they identified the soil parameters that were most affected by sample disturbance.

Lunne et al. (1997) discussed the influence of sample disturbance on laboratory measurements in detail and proposed their criterion on basis of Okamura's criteria (1971). Okamura (1971) listed some quantitative requirements for parameters to be used in evaluating sampling disturbance. Such parameters must be:

i. Easy to determine for perfectly undisturbed conditions.

ii. Regularly variable with disturbance, regardless of the depth of extraction, the stress system experienced, and the soil type.
iii. Sensitive to change due to disturbance.
iv. Easily and accurately measured.

Even though a number of the measurements like Su, ε_f, p_c' and M, are influenced by sample disturbance, it is not possible to satisfy (i). Consequently, Lunne et al. (1997) proposed a tentative criterion for quantifying sample disturbance in terms of the parameter $\Delta e/e_0$, where Δe is the change in pore volume when reconsolidating back to in situ stresses. They considered that measurements of $\Delta e/e_0$ was the most practical for quantification of sample disturbance, because satisfy Okumara's criteria, including (i). For a perfect specimen $\Delta e/e_0$ should be close to zero, and ε_{v0} too..

Table 22 gives the sample disturbance criterion proposed by Lunne et al. (1997).

Table 22. Sample disturbance criterion proposed by Lunne et al. (1997).

OCR	$\Delta e/e_0$			
	Very good to excellent	Good to fair	Poor	Very poor
$1-2$	< 0.04	$0.04 - 0.07$	$0.07 - 0.14$	> 0.14
2 - 4	< 0.03	$0.03 - 0.05$	$0.05 - 0.10$	> 0.10

The criterion in Table 22 may be expressed in terms of volumetric strain (ε_{v0}) using:

$$\varepsilon_{V0} = \frac{\Delta e}{e_0} \cdot \frac{e_0}{1 + e_0}$$

Equation 16

The sample disturbance criterion proposed above is mainly based on tests on marine clays with plasticity index in the range 10-55%, water content 30-90%, OCR=$1-4$ and depths $0-30m$ below ground level.

7.2.3 COMPARISON

Lunne et al. (1997) argued that $\Delta e/e_0$ is a better parameter to use than ε_{v0} because it is reasonable to assume that a certain change in pore volume will be increasingly detrimental to the particle skeleton as the initial pore volume decrease. That might be the case, but it is perhaps simpler to appreciate directly the different results obtained by both criteria.

In order to compare both criteria, the relation $\Delta e/e_0$ and ε_{v0} for different values of Δe is shown in Figure 98. The Andresen & Kolstad criteria is not valid for soils with lower compressibility ranges, since this criteria considers these soils as excellent to good quality. On the other hand, the Lunne et al (1997) criteria discriminates better the cases of reduced compressibility.
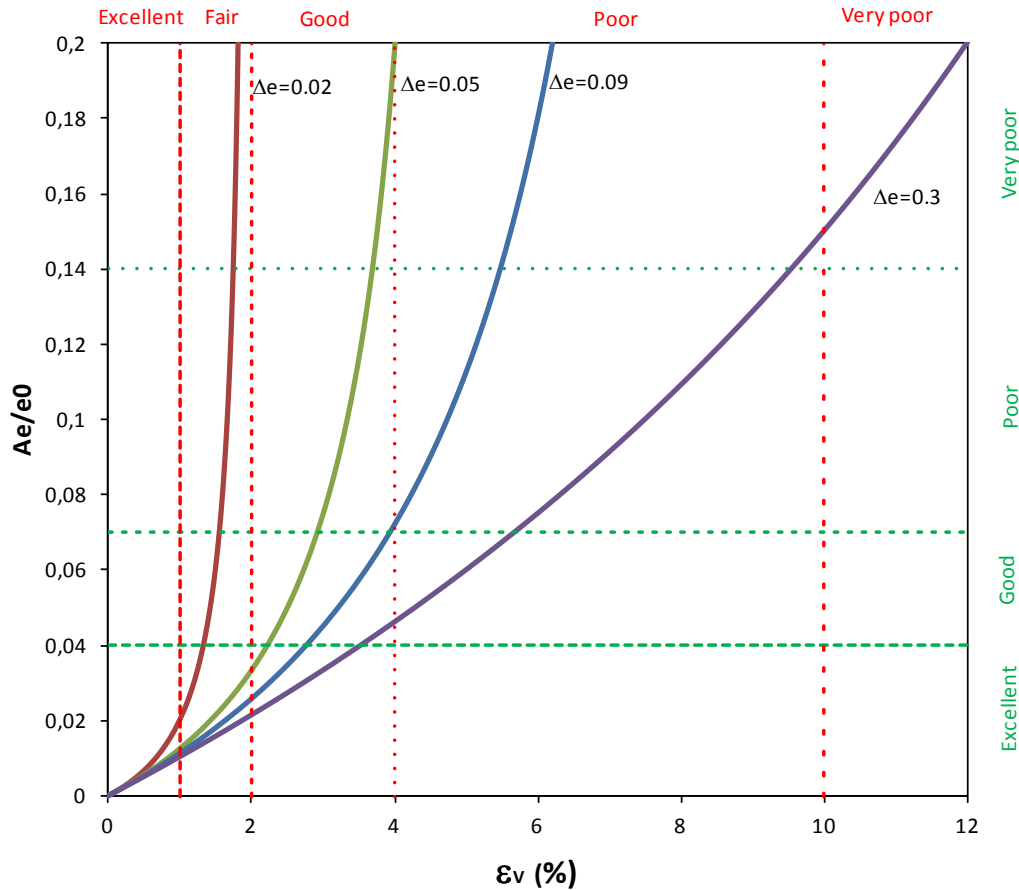
Figure 98. Comparison of the quality criteria.

7.3 APPLICATION TO THE CASTELLO SAMPLES

The soil of this study shows plasticity index in the range 15-22%, water content 26-48%, OCR=1.5 and depth of 13.8m below ground level. Consequently, Castello soil properties are inside the range of soils studied by Lunne et al. (1997).

Nevertheless, the purpose of this section is to evaluate if the sample disturbance criterion of Lunne et al. (1997) is valid / appropriate for Castello soil specimens. To do this, the results of the laboratory testing of Soft Soil Project (CRS oedometer and CAUC triaxial tests) are used. This evaluation had been attempted before for the sample quality project but the results have now been identified as erroneous.

Using the Lunne et al. (1997) criterion and the results obtained from CAUC triaxial and CRS oedometer tests, the quality of each specimen is evaluated, except specimens from Shelby (ϕ_{int}=83mm). Table 23 shows the results obtained from evaluation. All specimens fail in the two central categories being classified as either "good" or "poor". Most Sherbrooke samples classify as good, most Osterberg as poor, specimens from the Shelby tube lie in between.

Table 23. Qualiy classification according to Lunne et al (1997) criterion.

Type of Sampler	ID Specimen	$\Delta e_{34}/e_{03}$	Quality
Sherbrooke	TX1-MA-SHK6-L	0.062	Good
	TX2-MB-SHK6-L	0.060	Good
	TX3-MC-SHK6-L	0.053	Good
	EDO1-SHK6-L	0.074	Poor
	EDO2-SHK6-L	0.066	Good
	EDO3-SHK6-L	0.062	Good
Shelby (ϕ_{int} =76mm)	TX1-SHB80-L	0.134	Poor
	TX2-SHB80-L	0.133	Poor
	EDO1-SHB80-L	0.067	Good
	EDO2-SHB80-L	0.053	Good
	EDO3-SHB80-L	0.050	Good
Österberg (ϕ_{int} =95mm)	TX1-ÖST100-L	0.120	Poor
	EDO1-ÖST100-L	0.084	Poor
	EDO2-ÖST100-L	0.051	Good
	EDO3-ÖST100-L	0.060	Good
Österberg (ϕ_{int} =76mm)	TX1-ÖST80-L	0.086	Poor
	TX2-ÖST80-L	0.126	Poor
	EDO1-ÖST80-L	0.084	Poor
	EDO2-ÖST80-L	0.072	Poor
	EDO3-ÖST80-L	0.064	Good

In order to check if the obtained classifications for the specimens are correct, the mechanical parameters (e.g. Su, ε_f, p_c', M and ε_{v0}) that should reflect sample disturbance are now studied.

In the soils studied by Lunne et al. (1997) and in other applications of this criterion, it is assumed that better quality of a soil specimen should reflect: higher undrained shear strength, smaller axial strain at failure, higher preconsolidation stress, higher confined modulus and smaller volumetric strain.

To evaluate the validity of the classification, the Su, ε_f, p_c', M and ε_{v0} values from each specimen are plotted reflecting their assigned quality. If the quality is good a green dot is used and if the quality is poor a red cross is used.

7.3.1 UNDRAINED SHEAR STRENGTH

Figure 99 shows the undrained shear strenght (Su) values obtained from CAUC triaxial tests, classified using Lunne et al. (1997) criterion.
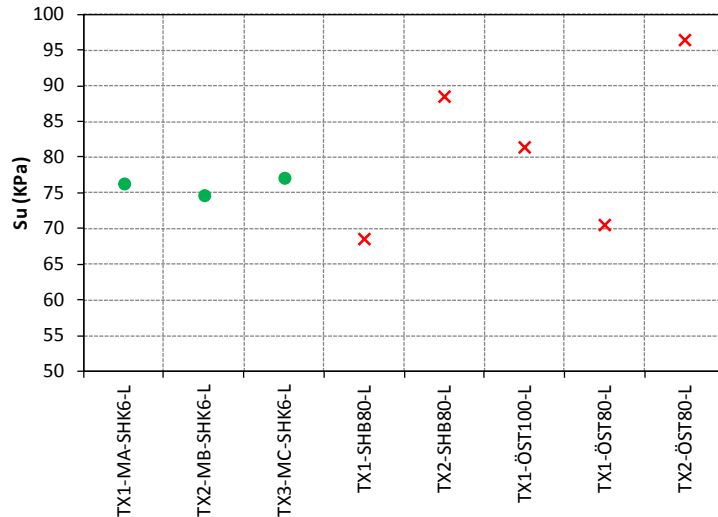
Figure 99. Undrained shear strength from CAUC triaxial tests.

Undrained shear strength values obtained from CAUC triaxial tests conducted in tube samples are greater than those obtained from the Sherbrooke block sample because strain rate during undrained shear stage is higher. According to Sheaham et al. (1996), higher strain rate leads to smaller induced excess pore-water pressure at failure, and therefore higher undrained shear strength.

Figure 100 shows the evolution of the shear stress and excess pore-water pressure with the axial strain from each specimen. One can see that in fact, the excess pore-water pressure in tube specimens is smaller than block specimens.
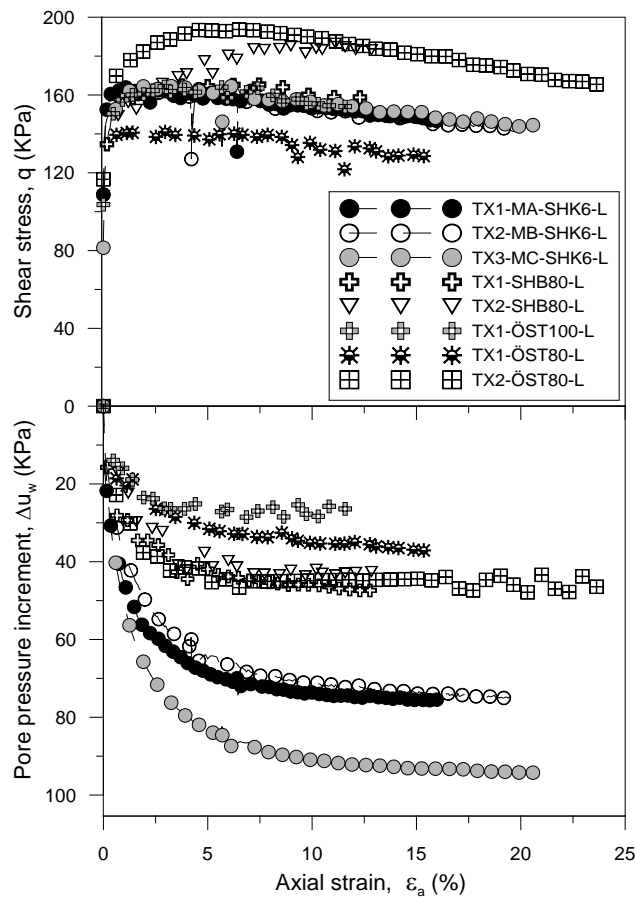
Figure 100. Evolution of the shear stress and excess pore pressure with the axial strain, CAUC triaxial tests.

According to Sheaham et al. (1996) for a strain rate region from 0.5-50%/h, the strength increase for a clay with OCR=1-2 is about 14,75% ± 2.0 SD. Taking into account that strain rate in CAUC triaxial tests conducted in block specimens is 0.2%/hour and 60%/hour in those tests conducted on tube specimens, the undrained shear strength values from tube specimens must be corrected reducing their values by 14,75% ± 2.0 SD. Figure 101 shows the corrected undrained shear strength (Su) values.
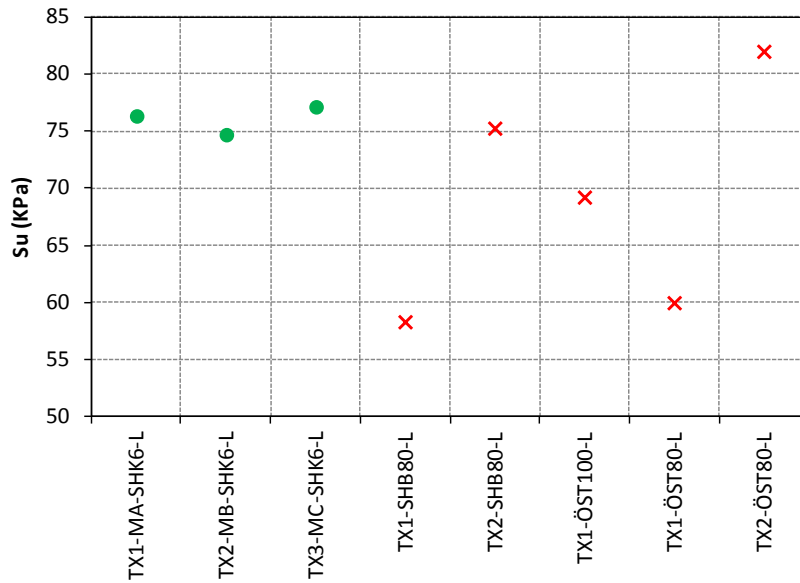
Figure 101. Corrected undrained shear strength values.

7.3.2 AXIAL STRAIN AT FAILURE

Figure 102 shows the axial strain at failure values obtained from CAUC triaxial tests, classified using Lunne et al. (1997) criterion.

Sheaham et al. (1996) estimate that strain rate does not influence ε_f values.

Since block specimens (good quality) show the smallest ε_f values, the classification is considered successful.
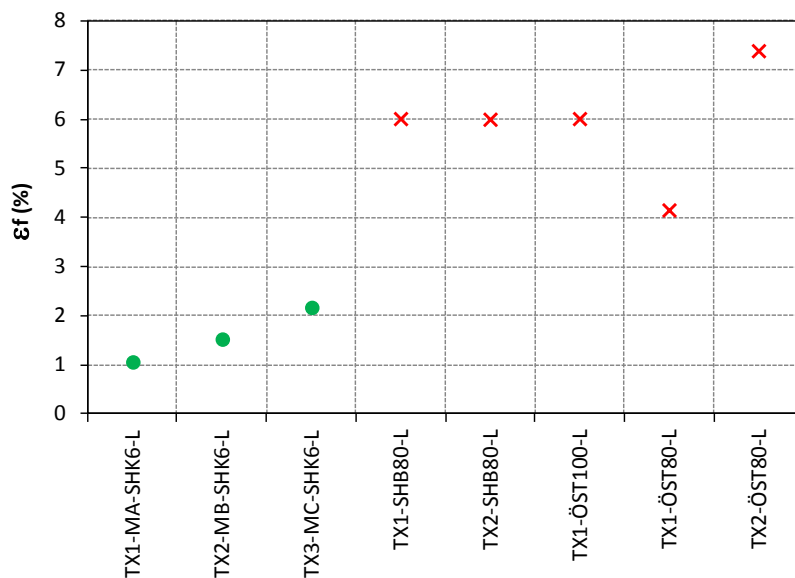
Figure 102. Axial strain at falilure from CAUC triaxial tests.

7.3.3   PRECONSOLIDATION STRESS

Figure 103 shows the preconsolidation stress values obtained from CRS oedometer tests using the Casagrande method, for all the specimens classified using Lunne et al. (1997) criterion.

Considering that higher preconsolidation stress value is associated with smaller sample disturbance. The classification generally reflects the real quality of the specimens.
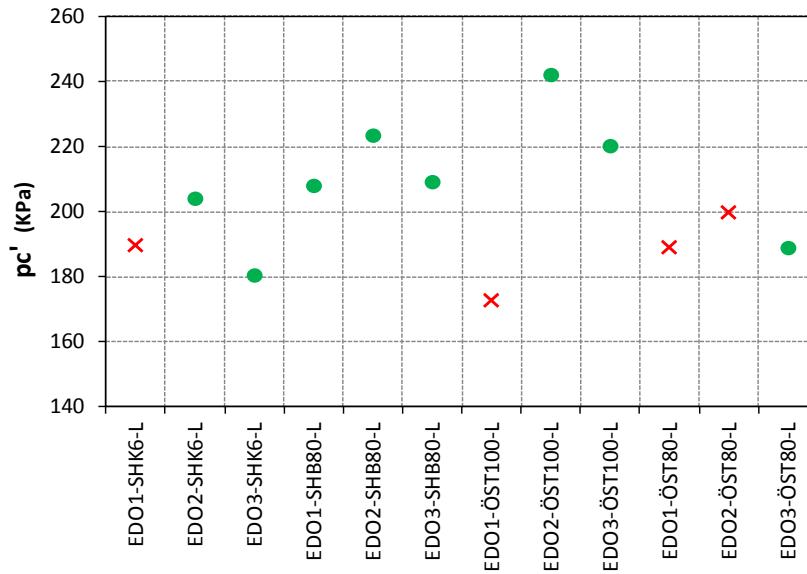
Figure 103. Preconsolidation stress from CRS oedometer tests.

7.3.4   CONFINED MODULUS AT IN SITU STRESS LEVEL

Figure 104 shows the confined modulus values at in situ stress level obtained from CRS oedometer tests, classified using Lunne et al. (1997) criterion.

Theorically, more sample disturbance implies smaller confined modulus, therefore the classifications is again broadly correct.
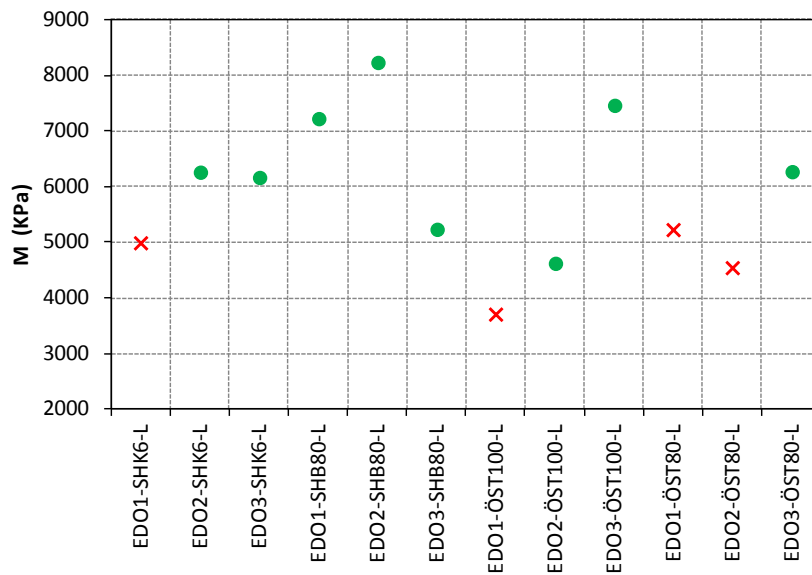
Figure 104. Confined modulus at in situ stress from CRS oedometer tests.

7.3.5 VOLUMETRIC STRAIN

Figure 105 shows the volumetric strain values during reconsolidation to in situ stresses obtained from CAUC triaxial and CRS oedometer tests, classified using Lunne et al. (1997) criterion.

Considering that higher volumetric strain is, higher sample disturbance; and reference values are those obtained from block specimens. Thus, the classification is again considered successful.
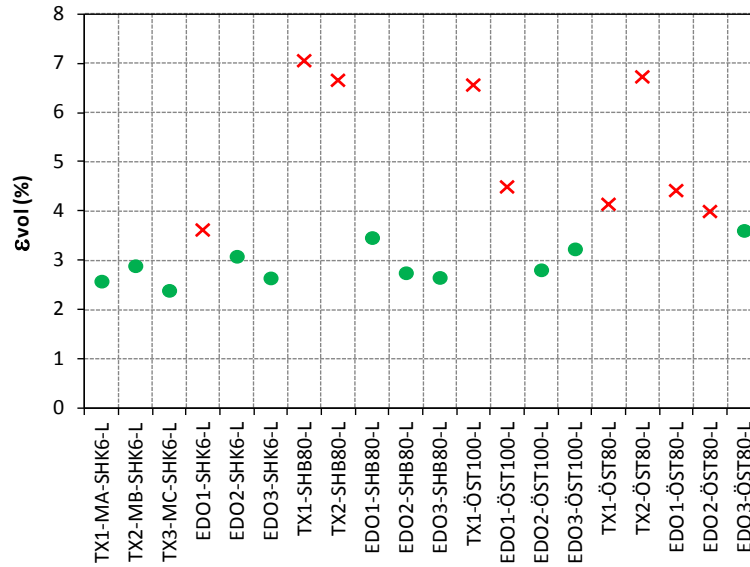
Figure 105. Volumetric strain from CAUC triaxial and CRS oedometer tests.

Chapter VIII. CONCLUSIONS

8.1 SUMMARY

The main results obtained in this thesis can be summarized as follows

- Even though there are more sophisticated computed tomography equipments specially tailored for geotechnical research, it has been shown that even a CT equipment designed for medical exploration can be usefully employed for geotechnical purposes.

- The main parameters of CT operation and image post-processing that control the quality of the results have been identified.

- The causes of the main artifacts present in the original images have been identified. Previous knowledge of which artifacts might appear will be useful in future uses, because is simpler to use CT settings to lessen artifact occurrence during the scanning process than to correct them in post-processing.

- A method to remove the main artifacts appearing has been applied successfully to the sample images acquired during the Soft Soil Project.

- A calibration of the CT number with bulk density of soil samples has been established. The calibration was tailored to take into account the specific composition (carbonate content) of the samples from Castello whose CT images we wanted to analyze. The values of wet bulk density thus deduced from CT and those from laboratory data were in very good agreement for the reference block sample.

- In CAT scans performed during calibration the effects of the grain size distribution, the carbonate content and the carbonate source were identified in the results. From those results it follows that re-calibration would be convenient to interpret CT from soils with different chemical composition or grain size distribution from those here explored.

- CAT density profiles of whole tube samples have been obtained. An approximate profile has also been obtained for the block sample –where the CT results were noisier. The density profiles of the tube samples reflect a slight trend to reduced density except close to the bottom of piston Österberg samplers, where density is increased.

- A sample quality assessment for all the specimens in the Soft Soil Project has been done, verifying the coherence of the classification obtained against laboratory tests. This confirms the applicability of the Lunne criteria of sample quality well away from the original geotechnical setting for which they were originally proposed.

- The CT scan images and the sample quality assessment results indicate that, for the Castello soil, there is no advantage in using Österberg piston-type samplers instead of simpler pushed Shelby tubes.

8.2 FUTURE WORKS

Further work, following on that described in this thesis can be

- To complete the analysis related to the effects of grain size distribution on the CT scans results.

- To analyze accurately with help from CT images the macro-morphology of the tube samples (fracturation) and its effects on the values of certain wet bulk density.

- To study the processes that might have caused the tube sample alterations identified in the CT scans.

- To study the performance of other criteria of sample quality, for instance those based on shear wave velocity or suction.

- To establish if there is any single clear indicator in CT scan images that is well correlated with sample category assessment.

REFERENCES

Alramahi Bashar A. (2004). *Assessment of shearing phenomenon and porosity of porous media using microfocus computed tomography*. Master thesis of B.Sc. Birzeit University, Ramallah, Palestine, pp. 2-16.

Amersham Health (2004): *Encyclopaedia of Medical Imaging by NICER (Medycyclopedia)* online version, http://www.amershamhealth.com/medcyclopaedia/

Amos C.L., Sutherland T.F., Radzijewski B. & Doucette M. (1996). *A rapid technique to determine bulk density of finegrained sediments by X-ray computed tomography*. J. Sediment. Res. 66, pp. 1023-1024.

Andersen A. & Kolstad P. (1979). *The NGI 54mm sampler for undisturbed sampling of clays and representative sampling of coarser materials*. Proceedings of International Symposium of Soil Sampling, Singapure. pp 13 -21

Ang A. & Tang W. (2006). *Probability concepts in engineering*. pp. 306 - 323

Arnold J.R., Testa J.P.J., Friedman P.J. & Kambic G.X. (1982). *Computed tomographic analysis of meteorite inclusions*. Science 219, pp. 383–384.

Arroyo M., Pineda J. & Sau N. (2012*). Ensayos de laboratorio sobre materiales de la zona de Castelló de Empúries*. Report for Igeotest, Ref UPC 010412.

Ashi J. (1997). *Computed tomographic scan image analysis of sediments*. Proceedings of the Ocean Drilling Program, Scientific Results, Vol. 156, pp. 151-159.

Auzerais F.M., Dunsmuir J., Ferréoal B.B., Martys N., Olsona J., Ramakrishna T.S., Rothman D.H. & Schwartz L.M. (1996). *Transport in sandstone: a study based on three dimensional microtomography*. Geophysical Research Letters 23, pp. 705-708.

Aylmore L.A.G. (1993). *Use of computer assisted tomography in studying water movement around plant roots*. Adv. Agron. 49, pp. 1–54.

Bach & Plaza J. (1987). *Sedimentación holocena en el litoral emergido de "l'Alt Empordà" (NE de Catalunya)*. Acta Geológica Hispánica, t. 21-22 (1986-1987), pp. 195-203.

Barrett H. & Swindell W. (1981). *Radiological Imaging; The Theory of Image Formation, Detection, and Processing*. Academic Press, New York.

Barret J.F. & Keat N. (2004). *Artifacts in CT: Recognition and Avoidance*. RadioGraphics 2004; 24: 1679–1691.

Bésuelle P., Viggiani G., Lenoir N., Desrues J. & Bornert M. (2006). *X-ray Micro CT for Studying Strain Localization in Clay Rocks under Triaxial Compression.* In: Advances in X-ray tomography for Geomaterials, 2nd International Workshop on X-Ray CT for Geomaterials, GeoX 2006, Grenoble & Aussois, 4-7 october, 2006, Org. J. Desrues, G. Viggiani, P. BésuelleÊ J. Desrues, G. Viggiani, P. Bésuelle Ed., ISTE, pp. 35-52.

Boespflug X., Ross N., Long B. & Dumais J.F. (1994). *Tomodenitométrie axiale: rélation entre l'intensité tomographique et la densité de la matiere*. Can. J. Earth Sci. 31, 426-434, in French.

Boespflug X., Long B. & Occhietti S. (1995). *Cat-scan in marine stratigraphy: a quantitative approach*. Mar. Geol. 122, pp. 281-301.

Boin M. & Haibel A. (2006). *Compensation of ring artefacts in synchrotron tomographic images*. Optics Express 14 12071-5.

Bonner B.P., Roberts J.J., Schneberk D.J., Marsh A., Ruddle C. & Updike E. (1995). *X-ray tomography of preserved samples from the Geysers scientific corehole*. Department of Energy DOE Report UCRL-JC-119573.

Bossi R.H., Friddel K.D. & Lowery A.R. (1990): *Computed Tomography. Non-Destructive Testing of Fiber-Reinforced Plastic Composites*, New York, Elsevier Applied Science.

Brooks R.A. & Di Chirico G. (1976). *Principles of computed assisted tomography (CAT) in radiography and radioisotopic imaging*. Phys. Med. Biol. 21, pp. 689-752.

Caers J., Swennen R. & Vervoort A. (1997). *Petrography and X-ray computerized tomography applied as an integral part of a rock mechanics investigation of discontinuities*. Tran. Ins. Min. Metallur. Sect. B-Appl. Earth Sci. 106, B38-B45.

Capowiez Y., Sammartino S. & Michel E. (2010). *Using X-ray tomography to quantify earthworm bioturbation non-destructively in repacked soil cores*. Geoderma 162 (2011) pp. 124-131.

Carlson W.D. & Denison C. (1992). *Mechanisms of porphyroblast crystallization: Results from high-resolution computed tomography*. Science, 257, pp. 1236-1239.

Cesareo R., Teixeira de Assis J. & Crestana S. (1994). *Attenuation coefficients and tomographic measurements for soil in the energy range 10-300 keV*. Appl. Rad. Isot. 45, pp. 613–630.

CISTIB (Center for Computational Image and Simulation Technologies in Biomedicine). *GIMIAS User Manual.*

Clayton C.R.I., Matthews M.C. & Simons N.E. (1995). *Site investigation*. Chapter 6. Sampling and sample disturbance. 2n edition.

Cnudde V., Masschaele B., Dierick M., Vlassenbroek J., Van Hoorebeke L. & Jacobs, P. (2006). *Recent progress in X-ray CT as a geosciences tool*. Applied Geochemistry, 21, pp. 826-832.

Coles M.E., Muegge E.L, Spanne P. & Jones K.W. (1995). *Computed microtomography of reservoir core samples*. US Department of Energy DOE report BNL-60656.

Colleta B., Letouzey J., Pinedo R., Ballard J. & Balé M. (1991). *Computerized X-ray tomography analysis of sandbox models: examples of thin-skinned thrust systems*. Geology 19, pp. 1063-1067.

Cordoliani Y.S., Hazebroucq V., Sarrazin J.L., Leveque C., Vincent B., Jouan E. (2008). *Helical Computed Tomography: Patient Exposure and Appropriate Use*. Journal de Radiologie 80, pp. 903-911.

Cortellazzo G., Simonini P., Della Vedova B., Ramigni M. & Bellis G.B. (1995). *Soil properties by computed tomography and needle probe*. Proc. 11th ECSMFE, Copenhagen, Danish Geotechnical Society, Copenhagen.

Coshell L., McIver R.G. & Chang R. (1994). *X-ray computed tomography of Australian oil shales: non destructive visualization and density determination*. Fuel 73, pp. 1317-1321.

Coshell L., McIver R.G. & Chang R. (1994). *X-ray computed tomography of Australian oil shales: non destructive visualization and density determination*. Fuel 73, pp. 1317-1321.

Cousineau & Chartier (2010). *Outliers detection and treatment: A review*. International Journal of Psychological Research, Vol. 3(1), pp. 58–67.

Crémer J-F., Long B., Desrosiers G., Montety L.D. & Locat J. (2002). *Application de la scanographie à l'étude de la densité des sédiments et à la caractérisation des structures sédimentaires : exemple des sédiments déposés dans la rivière Saguenay (Québec, Canada) après la crue de juillet 1996.* Can. Geotech. J. 39: pp. 440-450 (2002).

REFERENCES

Cruvinel P.E., Cesareo R., Crestana S. & Mascarenhas S. (1989). *X-ray and gamma-ray computerized monotomograph scanner for soil science and biomedical applications*. Centro per l'Ingegneria Biomedicala, Rapport no. 89.02.

Dalrymple N.C., Prasad S.R., Freckleton M.W., Chintapalli K.N. (2005). *Informatics in Radiology: Introduction to the Language of Three-Dimensional Imaging with Multidetector CT*. Radiographics 25, pp. 1409-1428.

Davis G. R. & Elliott J. C. (1997). *X-ray microtomography scanner using time-delay integration for elimination of ring artefacts in the reconstructed image*. Nucl. Instrum. Meth. Phys. 394 157-62.

De Craen M., Delleuze D., Volckaert G., Sneyers A. & Put M. (2000). *The Boom Clay as natural analogue*. SCK·CEN report, R-3444, Mol, Belgium.

Decleer J., Viaene W. & Vandenberghe N. (1983). *Relationships between chemical, physical and mineralogical characteristics of the rupelian Boom Clay, Belgium*. Clay Minerals Vol. 18, pp. 1-10.

Desrues J, Chambon R., Mokni M. & Mazerolle F. (1996). *Void ratio evolution inside shear bands in triaxial sand specimens studied by computed tomography*. Géotechnique 46(3): pp. 529-546.

Deterding J.M., Sutterfield F.D. & Burchfield T.E. (1993). *National Institute for Petroleum and Energy Research NIPER: final report*, October 1, 1983–December 31, 1993. Department of Energy, DOE report NIEPR-685.

Díaz J.I. & Ercilla G.(1993). *Holocene depositional history of the Fluvià – Muga prodelta, northwestern mediterranean Sea*. Marine geology, 111 (1), pp. 83-92.

Doran S. J. (2001). *A CCD-based optical CT scanner for high-resolution 3D imaging of radiation dose distributions: equipment specifications, optical simulations and preliminary results*. Phys. Med. Biol. 46 3191-213.

Duchesne M.J., Moore F., Long B.F. & Labrie J. (2009). *A rapid method for converting medical Computed Tomography scanner topogram attenuation scale to Hounsfield Unit scale and to obtain relative density values*. Engineering Geology 103, pp. 100-105.

Duliu O.G. & Tufan M. (1996). *Computer Axial Tomography investigation of sedimentary cores: a prospective study*. Rom. Rep. Phys. 46, pp. 437–440.

Duliu O.G., Tufan M. & Szobotka S. (1997). *Computer axial tomography investigation of polymetallic nodules*. Mar. Geol. 138, pp. 303-311.

Duliu O.G. (1999). *Computer axial tomography in geosciences: an overview*. Earth-Science Reviews 48, pp. 265–281.

European Commission. (May 1999). *European Guidelines on quality criteria for computed tomography (EUR 16262EN)*. Luxembourg: Office for Official Publications of the European Communities.

Ferguson A.H. & Gardner W.H. (1962). *Water content measurements in soil columns by gamma-ray absorption*. Soil Sci. Soc. Am. Proc. 5, pp. 390-398.

Ferreira T. & Rasband W. (2012). *ImageJ User Guide IJ 1.46r.* http://rsbweb.nih.gov/ij/docs/user-guide.pdf

Flannery B.P., Deckman H.W., Roberge W.G. & D'Amico K.L. (1987). *Three-dimensional X-ray microtomography*. Science 237, pp. 1439–1444.

Fransham P.B. & Jelen J. (1987). *Displacement of heavy oil visualized by CAT Scan*. J. Can. Petrol. Technol. 26, pp. 42-47.

Garg A., Kovscek A.R., Nikravesh, Castanier L.M. & Patzek T.W. (1996). *CT scan and neural network technology for construction of detailed distribution of residual oil saturation during waterflooding*. Proceedings of the Western Region Society of Petroleum Engineers Annual Meeting held in Anchorage, Alaska, pp. 1-10.

Goldstein L., Prasher S.O. & Ghoshal S. (2007). *Three-dimensional visualization and quantification of non-aqueous phase liquid volumes in natural porous media using a medical X-ray computed tomography scanner*. Journal of Contaminant Hydrology 93, pp. 96-110.

Grevers M.C.J., De Jong E. & Arnaud R.J. (1989). *The characterization of soil macroporosity with CT scanning*. Can. J. Soil Sci. 69, pp. 629–637.

Griffault L., Merceron T., Mossmann J.R., Neerdael B., De Cannière P., Beaucaire C., Daumas S., Bianchi A. & Christen R. (1996). *Acquisition et régulation de la chimie des eaux en milieu argileux pour le projet de stockage de déchets radioactifs en formation géologique*. Projet "Archimède argile". European Commission Nuclear Science and Technology. Final report EUR 17454 FR.

Hainsworth J.M. & Aylmore L.A.G. (1983). *The use of computer-assisted tomography to determine spatial distribution of soil water content*. Australian Journal of Soil Research, 21, pp. 435-443.

Hainsworth J.M. & Aylmore L.A.G. (1986). *Water extraction by a single plant root*. Soil Sci. Soc. Am. J. 50: pp. 841–848.

Hainsworth J. M. & Aylmore L. A. G. (1989). *Non-uniform soil water extraction by plant roots*. Plant and Soil 113, pp. 121–124.

Hasan M. K., Sadi F. & Lee S. Y. (2010). *Removal of ring artifacts in micro-ct imaging using iterative morphological filter.* Signal, Image and Video Processing DOI 10.1007/s11760-010-0170-z.

Haubitz B., Prokop M., Dohring W., Ostrom J.H. & Wellnhofer P. (1988). *Computed tomography of Archaeopteryx*. Paleobiology 14 (2), pp. 206-213.

Herman G.T. (1980). *Image reconstruction from projections*. The Fundamentals of Computerized Tomography. Academic Press, New York.

Hicks P.J., Deans H.A. & Narayanan K.R. (1992). *Distribution of residual oil in heterogeneous carbonate cores using X-ray CT*. SPE Form. Eval. 7, pp. 235-240.

Hirano T., Funaki M., Nagata T., Taghchi I. & Hamada H. (1990). *Observation of Allende and Antarctic meteorites by monochromatic X-ray based on synchrotron radiation*. Proceedings of the NIPR Symposium on Antarctic Meteorites 3, pp. 270-281.

Hiriyannaiah H. P. (1997). *X-ray Computed tomography for medical imaging*. IEEE Sig. Proc. Mag. pp. 42–59.

Holler P. & Kögler F.C. (1990). *Computer tomography: a nondestructive, high resolution technique for the investigation of sedimentary structures*. Mar. Geol. 91, pp. 263–266.

Hounsfield G.N. (1972). *A method of and apparatus for examination of a body by radiation such as X- or gamma-radiation*. British Patent No 1.283.915, London.

Hounsfield G.N. (1973). *Computerized transverse axial scanning (tomography)*. Part I. Description of system. Br. J. Radiol. 46 (552), pp. 1016-1022.

Howell, 1998. *Statistical methods in human sciences*. New York: Wadsworth.

REFERENCES

Hubble (1969). *Photon cross sections, Attenuation Coefficients and Energy Absorption Coefficients from 10 keV to 100 GeV*. National Standard Reference Data System, Vol 29.

International Electrotechnical Commission. (1994). *Evaluation and routine testing in medical imagingdepartments. Part 2-6: Constancy tests – X-ray equipment for computed tomography*. IEC, 1223-2-6. Geneva.

Jeandey C., Casagrande J.M., Briguet A., Ntoutoume T. & Guillot G. (1991). *Comparative imaging of liquids in rocks by NMR and differential X-ray computed tomography*. Material Resource Society Symposiums Proceedings 217, pp. 175–180.

Jenneson P. M. (2003). *An x-ray microtomography system optimized for the low-dose study of living organisms.* Appl. Rad. Isotopes 58 177-81.

Johansen G.A., Frøystein F., Hjertaker B.T. & Olsen Ø. (1996). *A dual sensor flow imaging tomographic system*. Meas. Sci. Technol. 7, pp. 297-307.

Johns, R.A., Steude, J.S., Castanier, L.M. & Roberts, P.V. (1993). *Nondestructive measurements of fracture aperture in crystalline rock cores using X-ray computed tomography*. Journal of Geophysical Research 98 (B2), 1889–1900.

Joschko M., Graff O., Muller P.C., Kotzke K., Lindner P., Pretschner D.P. & Larink O. (1991). *A non-destructive method for the morphological assessment of earthworm burrow system in three dimensions by X-ray computed tomography*. Biol. Fertil. Soils 11, pp. 88–92.

Joschko M., Müller P.C., Kotzke K., Dohring W. & Larink O. (1993). *Earthworm burrow system development assessed by means of X-ray computed tomography*. Geoderma 56, pp. 209–221.

Kantzas A., Marantettte D.F. & Jha K.N. (1992). *Computer-assisted tomography: from qualitative visualization to quantitative core analysis*. J. Can. Pet. Technol. 31 (9), pp. 48-56.

Kawamura T. (1990). *Nondestructive, three dimensional density measurements of ice core samples by X-ray computed tomography*. J. Geophys. Res., 95: 12407-12412.

Kenter J.A.M. (1989). *Applications of computerized tomography in sedimentology*. Mar. Geotechnol. 8 (3), pp. 201-211.

Ketcham R.A. & Carlson W.D. (2001). *Acquisition, optimization and interpretation of X-ray computed tomographic imagery: applications to the geosciences*. Computers & Geosciences 27, pp. 381-400.

Ketcham R.A. & Iturrino G.J. (2005). *Nondestructive high-resolution visualization and measurement of anisotropic effective porosity in complex lithologies using high-resolution X-ray computed tomography*. Journal of Hydrology, 302, pp. 92-106.

Ketcham R. A. (2006). *New algorithms for ring artifact removal.*Proc. SPIE 6318 63180O.

Kinney J. (1989). *X-ray microtomography on beamline X at SSRL.* Rev. Sci. Instrum. 60 2471-4.

Kinney, J.H., Breuning, T.M., Starr, T.L., Haupt, D., Nichols, M.C., Stock, S.R., Butts, M.D. & Saroyan, R.A. (1993). *X-ray tomographic study of chemical vapor infiltration processing of ceramic deposits*. Science 260, pp. 782–789.

Kister J., Cagnasso A. & Pis J.J. (1993). *Global characterization of oxidized coal by scanning X-ray technique*. In: Michalian, K.H. (Ed.), Proceedings 7th Int. Conf. Coal Sci., Devon, Canada, pp. 132-135.

Knoll G.F. (1989). *Radiation Detection and Measurement*. Wiley, New York.

Kropas-Hughes C. & Neel S. (2000). Basics of Computed Tomography Website of The American Society for Nondestructive Testing (ASNT). http://www.asnt.org/publications/materialseval/basics/may00basics/may00basics.htm

Kyriakou Y., Prell D. & Kalender W. A. (2009). *Ring artifact correction for high-resolution micro CT*. Phys. Med. Biol. 54 N385-91.

Lingtao Mao, Peng Shi, Hui Tu, Liqian An, Yang Ju & Nai Hao (2012). *Porosity Analysis Based on CT Images of Coal under Uniaxial Loading*. Advances in Computed Tomography, 2012, 1, pp. 5-10.

Lefebvre G. & Poulin C. (1979). *A new method of sampling in sensitive clay*. Can. Geotech. J., Vol 16, pp. 226-233.

Long B.F. & Ross N. (1991). *Études océanographiques physiques et biologiques: analyses complémentaires*. Rapp. INRS-Océanol. Proj. SEBJ 1LP-892-1-02.

Lunne T., Berre T. & Strandvik S. (1997). *Sample disturbance effects in soft low plasticity Norwegian clay*. Proc. Symp. Recent Developments in Soil and Pavement Mechanics, Rio de Janeiro, Balkema, pp. 81-92.

Maldonado A. (1972). *El delta del Ebro: estudio sedimentológico y estratigráfico*. Bol. Estrat. Univ. Barna. I vol, extr., 475 p.

Markowicz A.A. (1993). *X-ray physics*. In: Van Grieken, R.E., Markowicz, A.A. (Eds.), Handbook of X-ray Spectrometry. Marcel Dekker, New York, pp. 1-28.

Marques M.A. (1975). *Las formaciones cuaternarias del delta del Llobregat*. Acta Geológica Hispánica, 10(1): pp. 21-28.

Maylotte D.H., Spiro C.L., Cosaky P.C. & Lamby E.J. (1986). *X-ray computed tomography of coal*. Department of Energy, DOE Report MC 19210-2357.

Mazumder S., Wolf K.-H.A.A., Elewaut K. & Ephraim R. (2006). *Application of X-ray computed tomography for analyzing cleat spacing and cleat aperture in coal samples*. International Journal of Coal Geology 68 (2006) pp. 205-222.

McCullough E.C. (1975). *Photon attenuation in computed tomography*. Medical Physics 2: pp. 307-320.

McCullough E.C., Payne J.T., Baker H.L., Hattery R.R., Sheedy P.F., Stephens D.H. & Gedgadus E. (1976). *Performance evaluation and quality assurance of computed tomography scanners, with illustrations from the EMI, ACTA, and Delta scanners*. Radiology 120: pp. 173-188.

McNitt-Gray M.F. & Geffen D. (2006). *Tradeoffs in CT Image Quality and Dose*. Medical Physics, volume 33, issue 6, pp. 2154-2162.

Menke J. (2005). *Comparison of different body size parameters for individual dose adaptation in body CT of adults*. Radiology, Vol. 236, pp. 565-571.

Miller J. (1991). *Reaction time analysis with outlier exclusion: Bias varies with sample size*. The Quarterly Journal of Experimental Psychology, 43(4), pp. 907–912,

Mohammad E., Soo Yeol Lee & Md. Kamrul Hasan (2010). *Removal of ring artifacts in CT imaging through detection and correction of stripes in the sinogram*. Phys. Med. Biol. 55 (2010) pp. 6911-6930.

Montemagno C.D. & Pyrak-Nolte L. (1999). *Fracture network versus single fractures: measurements of fracture geometry with X-ray tomography*. Phys. Chem. Earth, in press.

Moreau E., Sardini P., Sahel A., Badri A., Touchard G. & Velde B. (1997). *Fissure network in clay soil-3D reconstruction and morphological analysis to quantify the flows*. Acta Stereol. 16, pp. 55-60.

Münch B., Trtik P., Marone F. & Stampanoni M. (2009). *Stripe and ring artifact removal with combined wavelet Fourier filtering*. Optics Express 17 8567-91.

REFERENCES

Mukunoki T., Otani J., Obara Y. & Kaneko K. (2003). *Artifacts of X-ray CT data in the analysis of geomaterial properties*. Proceedings of the International Workshop on X-ray CT for Geomaterials, Kumamoto, Japan, 6-7 November 2003.

Muzi L., Lyons A.P., Pouliquen E. (2004). *Use of X-ray computed tomography for the estimation of parameters relevant to the modeling of acoustic scattering from the seafloor*. Nuclear Instruments and Methods in Physics Research B 213 (2004) pp. 491-497.

Nakashima Y. (2004). *Nuclear Magnetic Resonance Properties of Water-Rich Gels of Kunigel-V1 bentonite*. Journal of Nuclear Science and Technology, Vol.41, No. 10, pp. 981-992.

Nakashima Y. & Kamiya S. (2007). *Mathematica Programs for the Analysis of Three-Dimensional Pore Connectivity and Anisotropic Tortuosity of Porous Rocks using X-ray Computed Tomography Image Data*. Journal of Nuclear Science and Technology, Vol. 44, No. 9, pp. 1233-1247.

Nave C. R. (2010). http://hyperphysics.phy-astr.gsu.edu/hbase/hframe.html. (Last accessed November 2010).

Okumara T. (1971). *The variation of mechanical properties of clay samples depending on its degree of disturbance*. Proc. Spec. Session on quality in Soil Sampling, 4th Asian Conference, ISSMFE, Bangkok, July 1971, pp. 73-81.

Orsi T.H., Edwards C.M. & Anderson A.L. (1994). *X-ray computed tomography: a nondestructive method for quantitative analysis of sediment cores*. J. Sediment. Res., A64: pp. 690-693.

Orsi T.H. & Anderson A.L. (1999). *Bulk density calibration for X-ray tomographic analyses of marine sediments.* Geo-Marine Letters (1999) 19: pp. 270-274.

Österberg (1973). *An improved hydraulic piston sampler*. Proc. 8th Int. Conf. Soil Mech. And Foundation Eng., Moscow, Volume 1.2, pp. 317-321.

Otani J.,Mukunoki T. & Kikuchi Y. (2002). *Visualization for engineering property of in-situ light weight soils with air foams*. Soils & Foundations the Japanese Geotechnical Society, 42 (3): pp. 93-105.

Otani J. (2004). *State of the art report on geotechnical X-ray research at Kumamoto University*. X-ray CT for Geomaterials; Soil, Concrete, Rocks. Proceedings of the International Workshop on X-ray CT for Geomaterials, GeoX2003, Kumamoto, Japan, Balkema Pub, pp. 43-77.

Otani J., Watanabe Y. & Chevalier B. (2010). *Introduction of X-ray CT application in geotechnical engineering - theory and practice.* IOP Conference Series: Materials Science and Engineering 10.

Permana A.K. (2012). *3-D Imaging of Cleat and Micro-cleat Characteristics, South Walker Creek Coals, Bowen Basin, Australia: Microfocus X-ray Computed Tomography Analysis*. Indonesian Journal of Geology, Vol. 7 No. 1 March 2012: pp. 1-9.

Peters E.J. & Afzall N. (1992). *Characterization of heterogeneities in permeable media with computer X-ray technique*. J. Petrol. Sci. Eng. 7, pp. 283-296.

Petrovici A.M., Siebert J.E. & Riecke P.E. (1982). *Soil bulk density analysis in three dimensions by computer tomographic scanning*. Soil Science Society. Am. J. 46, pp. 445-450.

Peyton, R.L., Haeffner, B.A., Anderson, S.H. & Gantzer, C.J. (1992). *Applying X-ray CT to measure macropore diameters in undisturbed soil cores*. Geoderma 53, pp. 329–340.

Phogat V.K. & Aylmore L.A.G. (1989). *Evaluation of soil structure by using computer assisted tomography*. Aust. J. Soil Res. 27, pp. 313–323.

Phogat V.K. & Aylmore L.A.G. (1996). *Computation of hydraulic conductivity of porous materials using computer-assisted tomography.* Australian Journal of Soil Research 34, pp. 671-678.

Phoon K. & Kulhawy F.H. (1999). *Characterization of geotechnical variability.* Canadian Geotechnical Journal, 36, pp. 612-624.

Prell D., Kyriakou Y. & Kalender W. A. (2009). *Comparison of ring artifact correction methods for flat-detector CT*. Phys. Med. Biol. 54 3881-95.

Prevost J.(1976). *Undrained Stress-Stran-Time behaviour of clays*. Journal of the Geotechnical Engineering Division. pp. 1245-1259.

Pullan, B.R., Ritchings, R.T. & Isherwood, I. (1981). *Accuracy and meaning of computed tomography attenuation values*. In: Newton, T.H., Potts, D.G. (Eds.), Technical Aspects of Computed Tomography. Mosby, St. Louis, pp. 3904–3917.

Pyrak-Nolte L.J., Montemagno C.D., Yang G., Cook G.W. & Myer L.R. (1995). *Three-dimensional tomographic vizualization of natural fracture networks and graph theory analysis of the transport properties*. In: Fujii, T. (Ed.), Proc. 8th Interanat. Congress on Rock Mechanics, ISRM, Balkema, Rotterdam, pp. 855-859.

Pyrak-Nolte L.J., Montemagno C.D. & Nolte D.D. (1997). *Volumetric image of aperture distribution in connected fracture networks*. Geophys. Res. Lett. 24, pp. 2343-2351.

Queisser A. (1988). *Nondestructive investigation of natural sandstone by computer tomography*. Bautenschutz Bausainierung 11, 54–60, in German.

Rhattas A. (1994). Tranfer de masse dans les argiles à faible porosité: analyse théorique et résultats expérimetaux. Thèse doctoral, Orléans.

Raven C. (1998). *Numerical removal of ring artifacts in microtomography*. Rev. Sci. Instrum. 69 2978-80.

Raynauld S., Fabre D., Mazerolle F., Geraud Y. & Latière H. (1989). *Analysis of the internal structure of rocks and characterization of mechanical deformation by non-destructive method: X-ray tomodensitometry*. Tectonophysics 159, pp. 149-159.

Remeysen K. & Swennen R. (2008). *Application of microfocus computed tomography in carbonate reservoir characterization: possibilities and limitations*. Marine and Petroleum Geology 25, pp. 486–499.

Robertson E.P., Bala G.A. & Thomas C.P. (1994). *Laboratory methods for enhanced oil recovery core floods*. Department of Energy, DOE Report IDr01570-T171.

Romans L. E. *CT Image Quality.* http://www.cewebsource.com/

Sadi F., Lee S. Y. & Hasan M. K. (2010). *Removal of ring artifacts in computed tomographic imaging using iterative center weighted median filter*. Comput. Biol. Med. 40 109-18.

Sainz-Amor E. & Julià R. (1999). *Using heavy mineral assemblages for palaeoenvironmental interpretation in alluvial coastal plains: The Empordà case study (NE Iberian Peninsula)*. Acta Hispanica, Vol. 31, No. 4, pp. 55-65.

Schaoping F., Werner F. & Brossman J. (1994). *Computed tomography application in studding biogenetic structures in sedimentary cores*. Palaios 9, pp. 116-119.

Sheahan T. C. & Germaine J.T. (1996). Rate-dependent undrained shear behavior of saturated clay. Journal of Geotechnical Engineering, vol. 122, Issue 2.

Shepp, L.A. & Logan, B.F. (1974). *Reconstructing interior head tissue from X-ray transmissions*. IEEE Transactions on Nuclear Science NS-21, pp. 228-236.

REFERENCES

SIEMENS Medical Solutions. *Computed Tomography. Its History and Technology*. Pp. 12-31.

SIEMENS Medical Solutions. *SOMATOM Spirit Application Guide*.

Siemens Somatom HiQ System introduction (1991). TDF 11, C1-016.041.10. Berichte Meditzinische Technik. Siemens.

Silver M.D. (1994). *Target self-attenuation extension to the Desorby and Boyer thick-target bremsstrahlung spectrum*. Medical Physics 21 (4), pp. 577-579.

Simons F.J., Verhelst F. & Swenen R. (1997). *Quantitative characterisation of coal by means of microfocal X-ray computed tomography (CMT) and colour image analysis (CIA)*. Int. J. Coal Geol. 34, pp. 69-88.

Soane B.D. (1967). *Dual energy gamma-ray transmission for coincident measurement of water content and dry bulk density of soil*. Nature 214, pp. 1273-1274.

Soh W. (1997). *Computed tomography scan analysis of site 941 cores, western mass-trasnport deposit, Amazon fan*. Proceedings of the Ocean Drilling Program, Scientific Results, Vol. 155. Flood, R.D., Piper, D.J.W., Klaus, A., and Peterson, L.C. (Eds.).

Stonestrom J., Alvarez R. & macovski A. (1981). *A framework for special artifact corrections in X-ray CT.* IEEE Trans Biomed Eng BME-28(2): pp. 128-141.

Strumas N., Antonyshyn O., Yaffe M.J., Mawdsley G. & Cooper P. (1995). *Computed Tomography Artifacts: An Experimental Investigation of Causative Factors*. 49th Annual Meeting of the Canadian Society of Plastic Surgeons, Saskatoon, Saskatchewan, June 1995.

Swennen R., Poot B. & Marchal G. (1991). *Computerized tomography as a tool in reservoir characterization*. Zbl. Geol. Palaönt., Teil I 8, pp. 1105-1124.

Tanaka A., Nakano T. & Ikehara K. (2011). *X-ray computerized tomography analysis and density estimation using a sediment core from the Challenger Mound area in the Porcupine Seabight, off Western Ireland*. Earth Planets Space, 63, pp. 103-110.

Tang X., Ning R., Yu R. & Conover D. (2001). *Cone beam volume CT image artifacts caused by defective cells in x-ray flat panel imagers and the artifact removal using a wavelet-analysis-based algorithm*. Med. Phys. 28 812-25.

Ter-Pogossian MM. (1976). *The challenge of computed tomography*. American Journal of Roentgenology; 127(1): pp. 1-2.

Tollner E.W. & Murphy C. (1991). *Factors affecting soil X-ray absorption coefficients with computed tomography*. Trans. ASAE 43, pp. 1047-1053.

Tollner E. W., Melear N. D., Rodriguez L. A.& Wright M. E. (1998). *Soil Aggregate Size Distributions Using X-Ray Images*. Transactions of the American Society of Agricultural Engineers 41, No. 4 (July-August 1998): pp. 1207-1215.

Torczynski J.R., Adkins D.R., Shollenberger K.A. & O'Hern T.J. (1995). *Application of gamma-densitometry tomography to determine phase spatial variation in two-phase and three-phase bubbly flows*. Department of Energy, DOE Report SAND-95-2635C.

Van Geet M.,Swennen R. & Wevers M. (2000). *Quantitative analysis of reservoir rocks by microfocus X-ray computerised tomography*. Sedimentary Geology 132 (2000) pp. 25-36.

Van Geet M. (2001). *Optimization of microfocus X-ray computer tomography for geological research with special emphasis on coal components (macerals) and fractures (cleats) characterization*. PhD thesis, K. U. Leuven, Belgium.

Verhelst F., David P., Fermont W., Jegers L. & Vervoort A. (1996). *Correlation of 3-D computerized topographies scans and 2-D color image analysis of Westphalian coal by menace of multivariance statistics*. Int. J. Coal Geol. 29, pp. 1-21.

Verhelst F., Vervoort A., De Bosscher Ph. & Marchal G. (1995). *X-ray computerized tomography determination of hetero- geneities in rock samples*. In: Fujii, T. (Ed.), Proc. 8th International Congress on Rock Mechanics. ISRM, Balkema, Roterdam, pp. 105-108.

Viggiani G., Lenoir N., Bésuelle P., Marco Di Michiel, Marello S., Desrues J. & Kretzschmer M. (2004). *X-ray microtomography for studying localized deformation in fine-grained geomaterials under triaxial compression*. C. R. Mécanique 332, No. 10, pp. 819-826.

Vinegar H. (1986). *X-ray CT and NMR imaging of rocks*. J. Petrol. Technol. 38, pp. 257-259.

Vinegar H.J. & Wellington S.L. (1986). *Tomographic imaging of three-phase flow experiments*. Review of Scientific Instruments, 58, pp. 96-107.

Vinegar H., De Wall J. & Wellington S.L. (1991). *CT studies of brittle failure in Castlegate sandstone*. Int. J. Rock Mechan. Min. Scie. Geomechan. Abs. 28, pp. 441-448.

Wellington, S.L. & Vinegar, H.J. (1987). *X-ray computerized tomography*. Journal of Petroleum Technology 39 (8), pp. 885–898.

Wevers, M., De Meester, P. & Swennen, R., (2000). *Microfocus X-ray Computer Tomography in Materials Research*. Proceeding of the 15th World Conference on Nondesructive Testing, Roma, Italy, 15-21 October 2000.

Withjack, E.M. (1988). *Computed tomography for rockproperty determination and fluid-flow visualization*. SPE Formation Evaluation 3 (4), pp. 696–704.

Withjak E.M., Graham S.K. & Yang C.-T. (1990). *Determination of heterogeneities and miscible displacement characteristics in coreflood by CT scanning*. 65th Annual Technical Conference and Exhibition of the Society of Petroleum Engineers, SPE 20490, pp. 213-224.

Wissa A. et al. (1971). *Consolidation at a constant rate of strain*. J.Soil Mech. Eng. Div., Am. Soc. Civ. Eng., 97, SM10

Yanbin Yao, Dameng Liu, Yao Che, Dazhen Tang, Shuheng Tang & Wenhui Huang (2009). *Non-destructive characterization of coal samples from China using microfocus X-ray computed tomography*. International Journal of Coal Geology 80 (2009) pp. 113-123.

Yoshikawa H. (2004). X-ray Computed Tomography. Website of Inouye Labs, Japan. http://ctlab.bk.tsukuba.ac.jp/~hiroki/blind/x-rayCT.html

Zeng Y., Gantzer C.J., Peyton R.L. & Anderson S.H. (1996). *Fractal dimension and lacunarity of bulk density determined with X-ray computed tomography*. Soil Sci. Soc. Am. J. 60, pp. 1718-1724.

Zinsmeister, W.J. & De Nooyer, C. (1996). *Computed tomography; non-destructive techniques for visualizing internal morphology of invertebrates*. Geological Society of America, Abstracts with Programs 28 (7), p. 294.

APPENDIX I. RESULTS FROM NOISE ARTIFACT TREATMENT

The parameters of the filter used are summarized in Table 24.

Table 24. Filtering process of OED2-SHK6-L specimen.

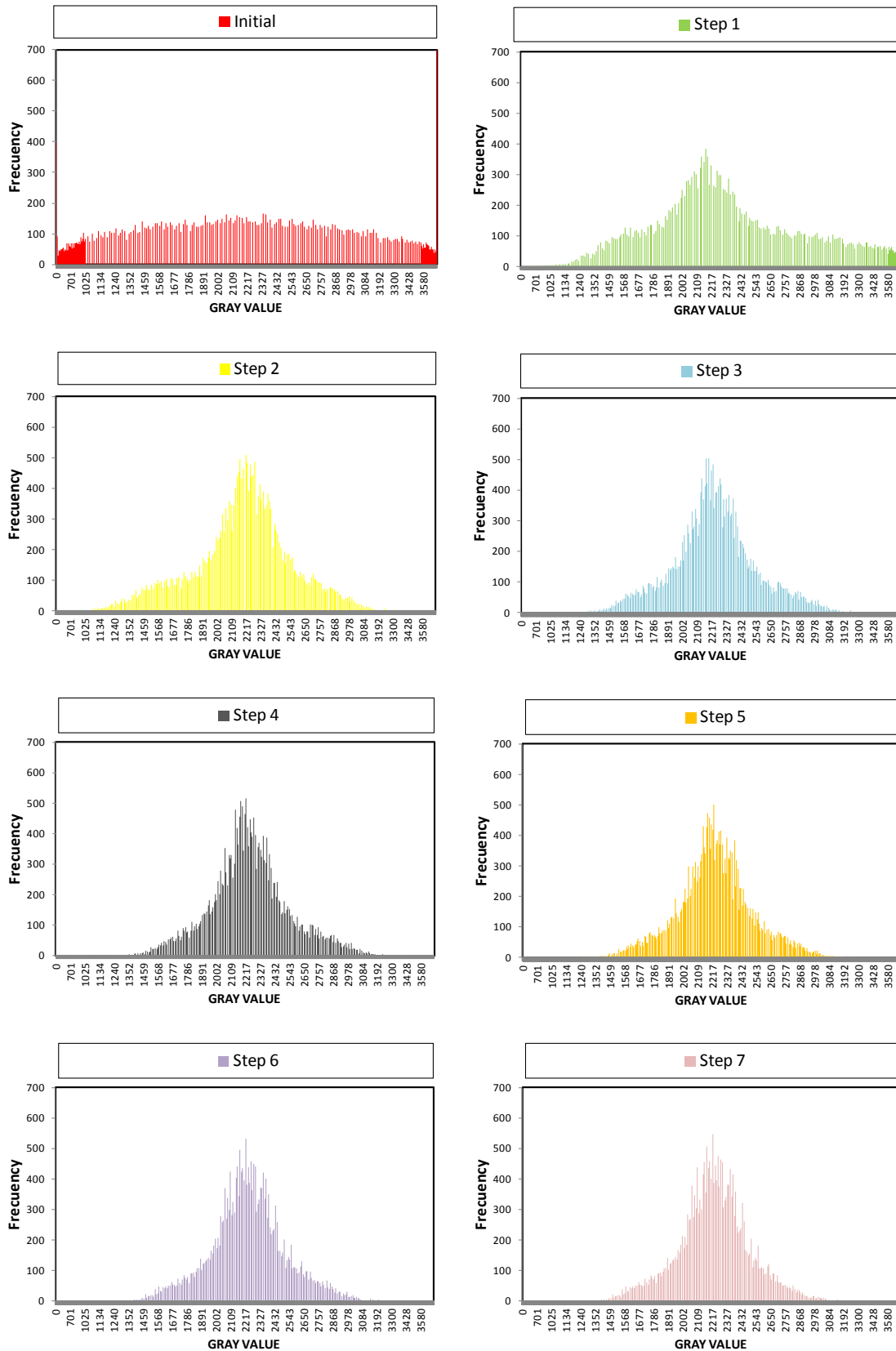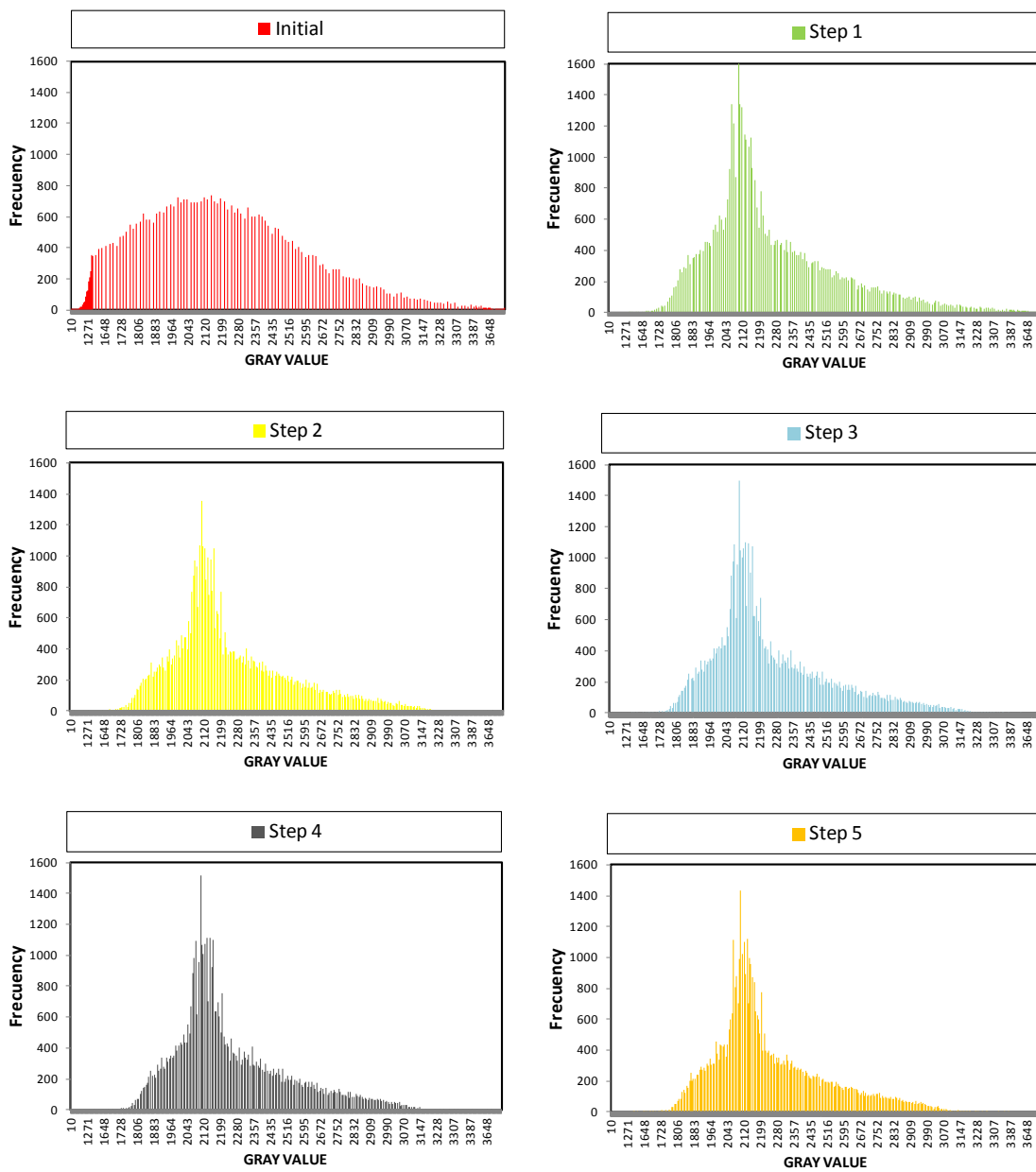| ID step	Radius	Thershold	Which Outliers
Step 1	5	600	Dark
Step 2	15	1000	Bright
Step 3	5	1000	Bright
Step 4	20	550	Dark
Step 5	10	950	Bright
Step 6	10	550	Dark
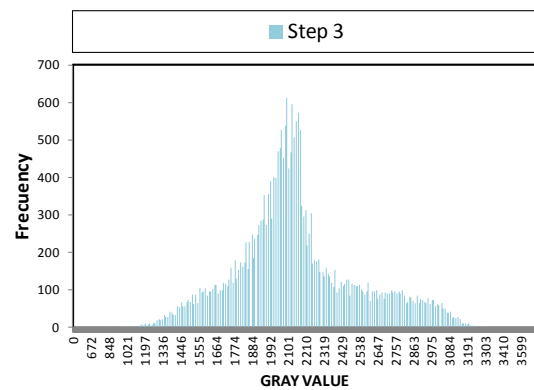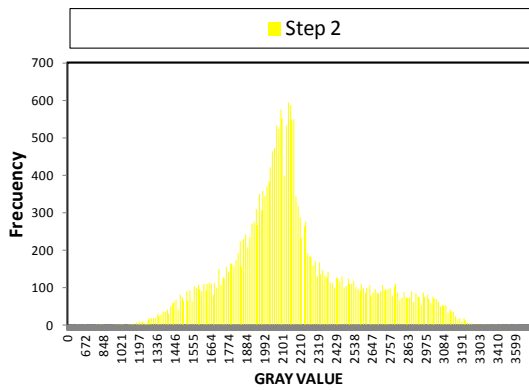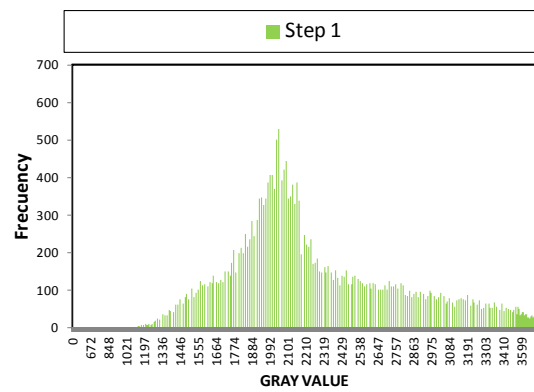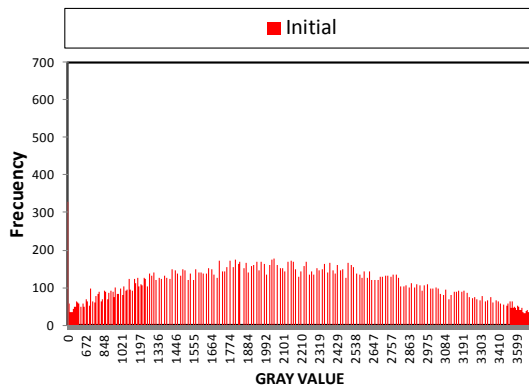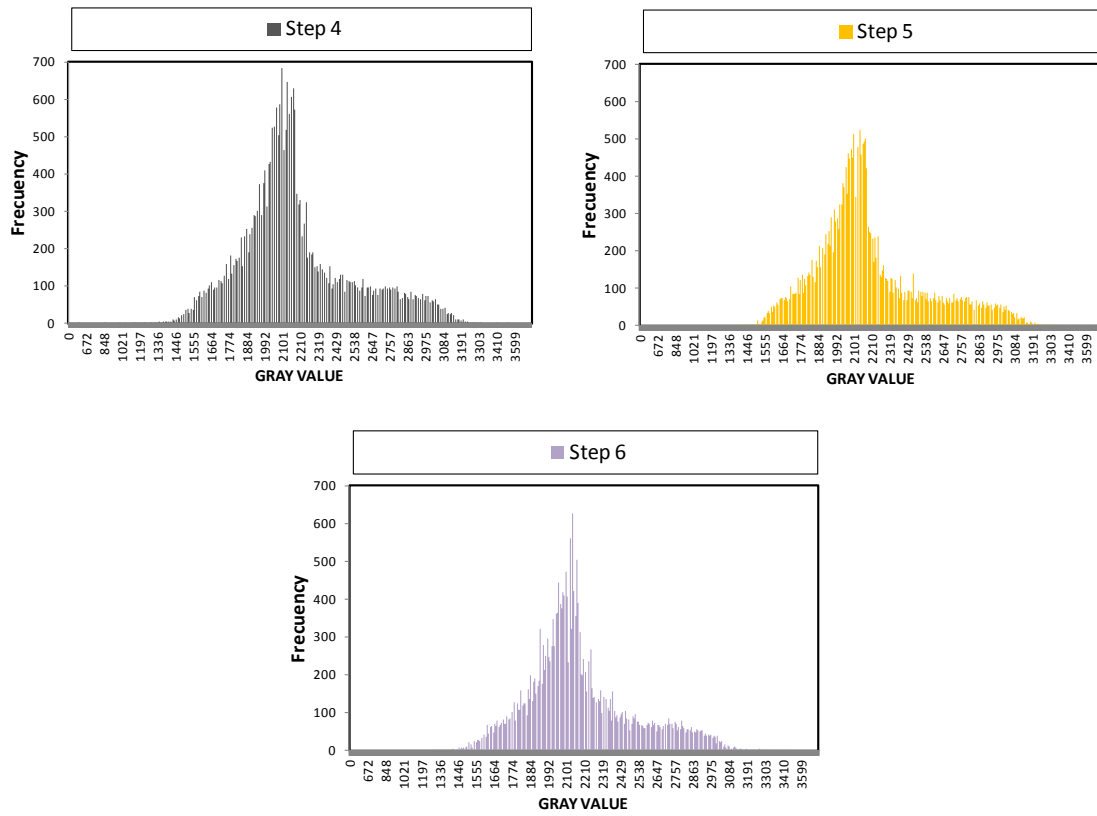
Figure 106. Filtering results of OED2-SHK6-L specimen.

OED3-SHK6-L

The parameters of the filter used are summarized in Table 25.

Table 25. Filtering process of OED3-SHK6-L specimen.

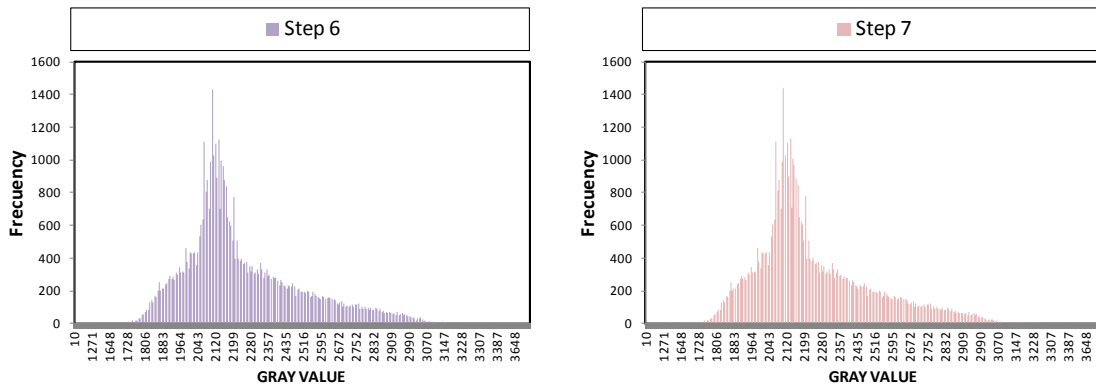| ID step	Radius	Thershold	Which Outliers
Step 1	5	800	Dark
Step 2	5	650	Bright
Step 3	5	650	Dark
Step 4	5	600	Dark
Step 5	5	625	Bright
Step 6	2	625	Bright
Step 7	3	600	Bright

Figure 107. Filtering results of OED3-SHK6-L specimen.

TX1-MA-SHK6-L

The parameters of the filter used are summarized in Table 26.

Table 26. Filtering process of TX1-MA-SHK6-L specimen.

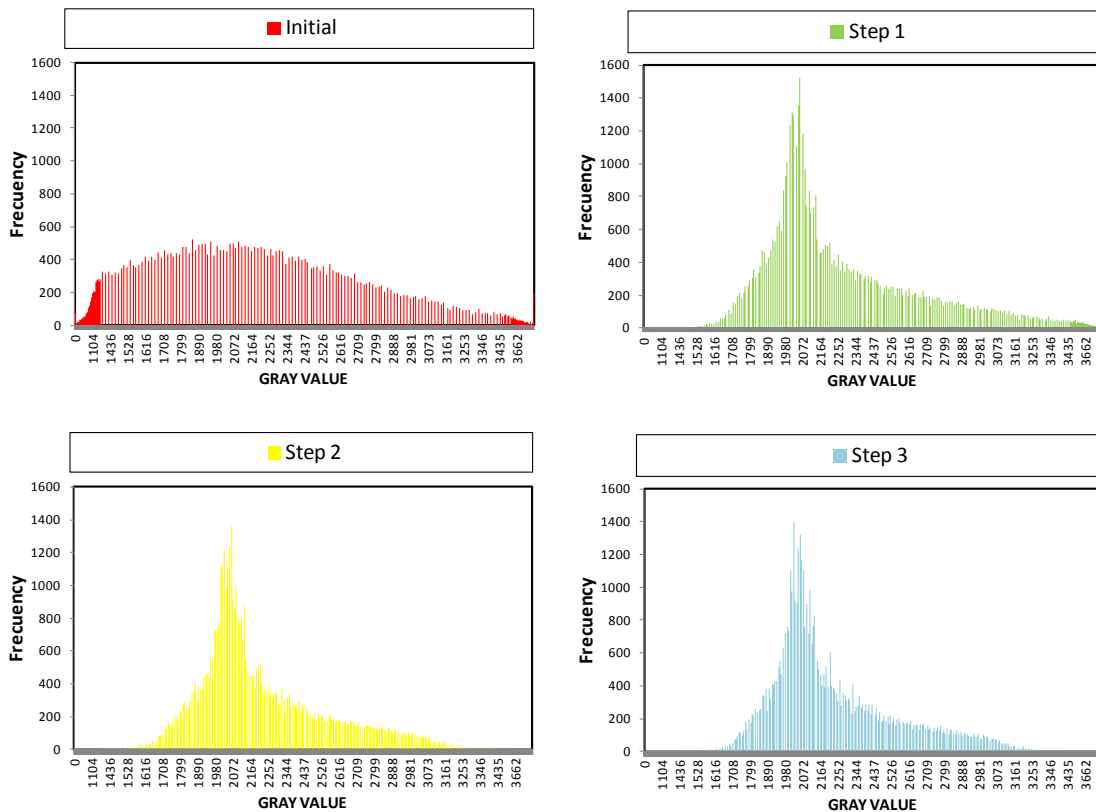| ID step	Radius	Thershold	Which Outliers
Step 1	40	300	Dark
Step 2	40	1000	Bright
Step 3	10	300	Dark
Step 4	10	950	Bright
Step 5	10	900	Bright
Step 6	5	900	Bright
Step 7	5	870	Bright

Figure 108. Filtering results of TX1-MA-SHK6-L specimen.

TX2-MB-SHK6-L

The parameters of the filter used are summarized in Table 27.

Table 27. Filtering process of TX2-MB-SHK6-L specimen.

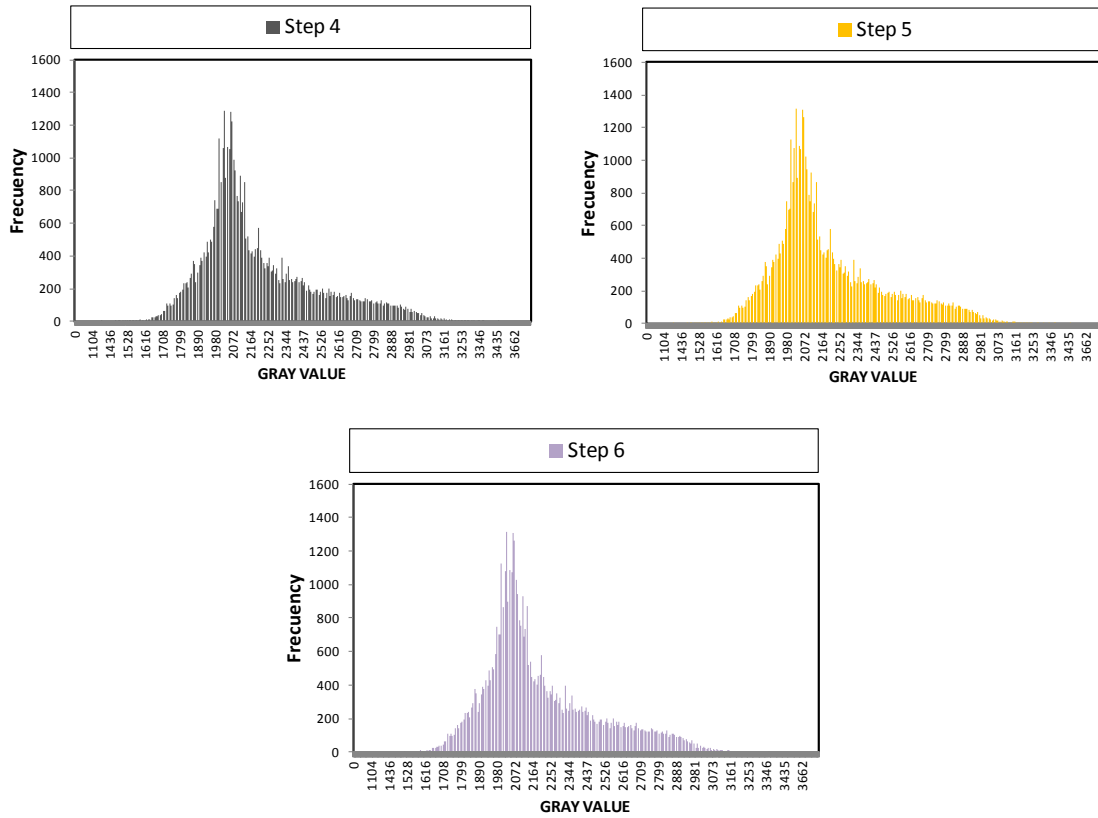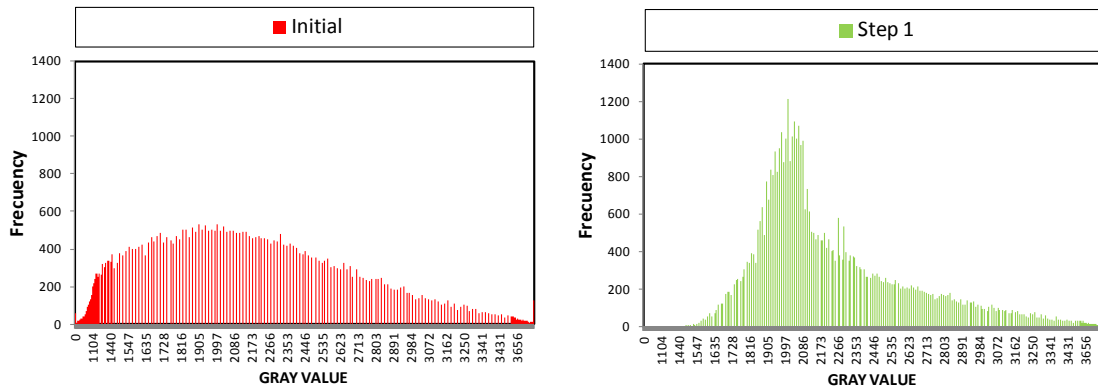| ID step	Radius	Thershold	Which Outliers
Step 1	40	300	Dark
Step 2	40	1000	Bright
Step 3	10	300	Dark
Step 4	10	950	Bright
Step 5	10	900	Bright
Step 6	3	800	Bright

Figure 109. Filtering results of TX2-MB-SHK6-L specimen.

TX3-MC-SHK6-L

The parameters of the filter used are summarized in Table 28.

Table 28. Filtering process of TX3-MA-SHK6-L specimen.

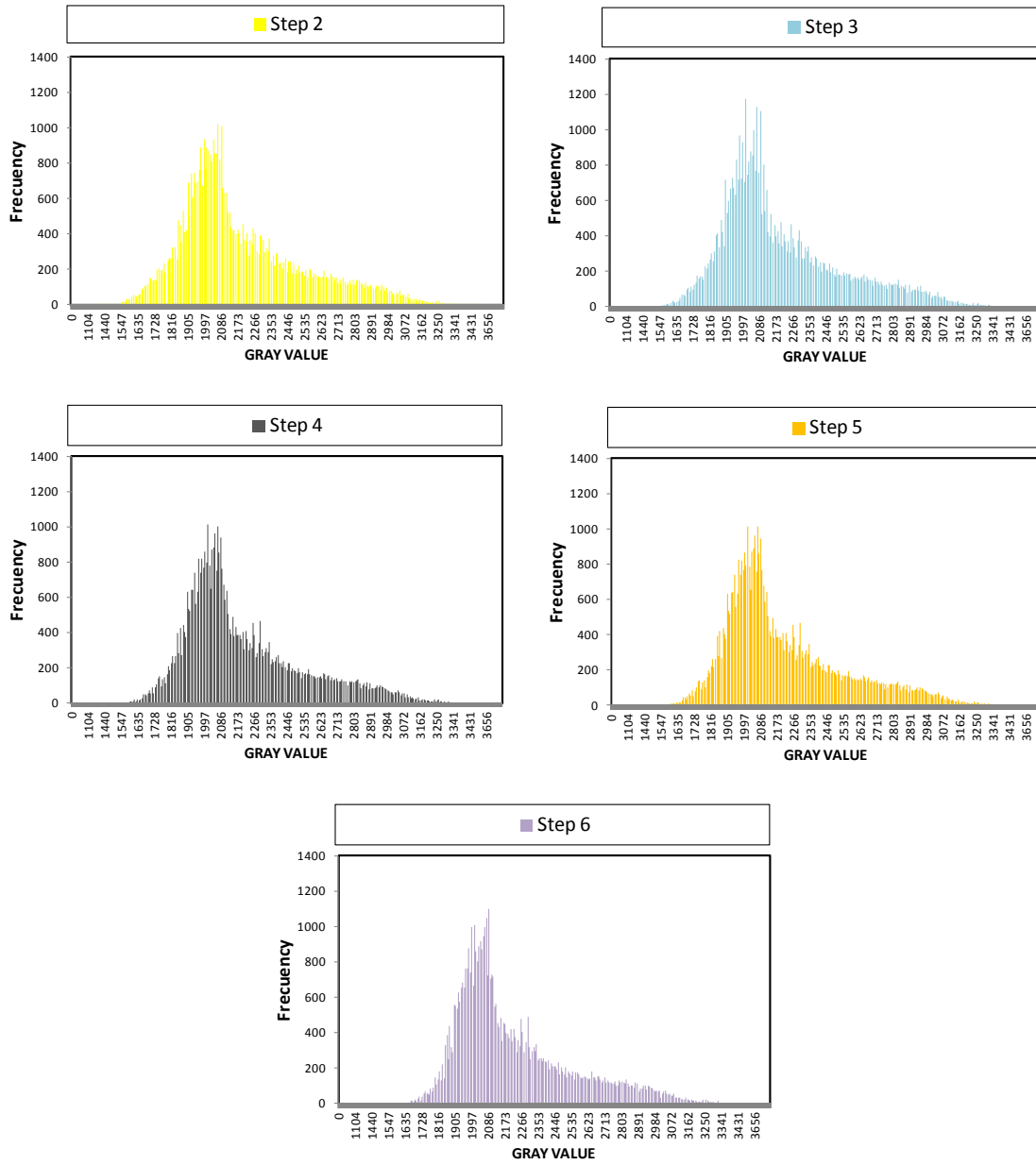| ID step	Radius	Thershold	Which Outliers
Step 1	40	300	Dark
Step 2	40	1000	Bright
Step 3	10	300	Dark
Step 4	8	275	Dark
Step 5	5	275	Dark
Step 6	5	200	Dark

Figure 110. Filtering results of TX3-MC-SHK6-L specimen.